Department of Electrical and Computer Engineering
Faculty of Engineering and Science

PAPR Reduction in Multicarrier Communication Systems Using Efficient Pulse Shaping Technique

Zee Ang Sim
0000-0003-2031-1060

This thesis is presented for the Degree of
Doctor of Philosophy
of
Curtin University

March 2020

Declaration

To the best of my knowledge and belief this thesis contains no material previously published by any other person except where due acknowledgement has been made.

This thesis contains no material which has been accepted for the award of any other degree or diploma in any university.

Signature:

Date: 31 March, 2020

Acknowledgements

First and foremost, I would like to express my deepest gratitude to my lead supervisor, Dr Regina Reine, for her guidance and support throughout this research. Her passion and determination has motivated me to pursue this PhD degree. I truly appreciate her patience in shaping my perspective towards the world of research. Next, I would like to thank A/Prof. Zhuquan Zang, A/Prof. Lenin Gopal, and Dr Filbert H. Juwono. Their valuable feedback and suggestions have improved the quality of this research, and provided me a broad view of life as a researcher. I would also like to thank A/Prof. Chua Han Bing, who is the Chairperson of my thesis committee, for his necessary administrative guidance.

To my family and relatives, I am very thankful of your teachings, support, encouragements, and tolerance, throughout my entire research period. I would also like to extend my gratitude towards my sister, who has been accompanying my parents while I am away from home. To all my friends and people whom I have met during my PhD journey, I am thankful to all of you in making this journey a memorable one.

This research is supported by the Malaysia Ministry of Higher Education (MOHE) under the Fundamental Research Grant Scheme (FRGS) with project ID: FRGS/1/2017/TK04/CURTIN/03/1. I would also like to thank Curtin University Malaysia, in particular the Faculty of Engineering and Science (FoES) and Curtin Malaysia Graduate School, for their financial and administrative support throughout my study.

Abstract

Multicarrier modulation such as Orthogonal Frequency Division Multiplexing (OFDM) has been adopted in the latest wireless communication systems due to its high spectral efficiency, high robustness against fading channel and simple implementation using the fast Fourier transform (FFT) and inverse fast Fourier transform (IFFT) pair. However, OFDM is not sufficient to support the more complex demand of emerging communication system such as the fifth generation (5G) communication system. Multiuser OFDM (MU-OFDM) can be used to improve the current OFDM system, and Generalized Frequency Division Multiplexing (GFDM) has been considered as a potential candidate to replace the OFDM system for 5G communication system. Despite carrying out the same advantages as OFDM, GFDM also inherits the high peak-to-average power ratio (PAPR) in the transmitted signal. High PAPR in the transmitter of multicarrier systems will result in nonlinearity of the transmit signal when passed through a high power amplifier (HPA). One way to prevent the nonlinearity is to increase the input back off (IBO) of the HPA. However, this way is costly and inefficient. Hence, reducing the PAPR of the transmitted signal is essential.

Pulse shaping can be used to reduce the PAPR of the OFDM transmitted signal by shaping the OFDM subcarriers using properly selected pulse shaping filters. This technique can be implemented for MU-OFDM. Ideal Nyquist filters, such as the raised cosine (RC) and the root raised cosine (RRC), are commonly used for pulse shaping. However, ideal filters are not causal. The filters need to be truncated and shifted before being implemented practically. Furthermore, to

ensure user independence in the MU-OFDM system, different orthogonal filters are often used for different user. The contribution from this work is to design a set of pulse shaping filters using computationally efficient optimisation approach subjected to auto-correlation and cross-correlation constraints. Numerical examples show that the set of designed filters is able to reduce the PAPR of the MU-OFDM signal while improving the bit error rate (BER) performance.

As mobile communication systems move towards the 5G networks, the tactile internet will become a necessity due to Internet of Things (IoT) devices such as sensors requiring extremely low latency for data transmission. Using the guard bands to suppress the out-of-band (OOB) radiation as well as transmitting short bursts of data over a long period in current OFDM systems is not desired for the tactile internet and is a waste of resources. The GFDM system is able to flexibly adjust the system parameters to solve the shortcomings of the OFDM system. Data symbols in the GFDM system are shaped by a principle filter that is shifted in both time and frequency domains. To avoid using excessive guard bands, it is meaningful to design the optimal filter for the GFDM system. The contribution from this work is to formulate the filter design problem using the quadratic programming approach with the aim to reduce the OOB radiation and the PAPR of the GFDM transmitted signal. Numerical examples show that the designed filter has reduced the PAPR and the OOB radiation of the GFDM signal. Furthermore, the BER performance at the receiver has also been improved.

In a practical system, the nonlinearity due to HPA will affect the overall system performance. Nonlinearity will result in spectral regrowth and distortion of the transmit signal, which reduces the spectral efficiency. On the other hand, increasing the IBO to prevent nonlinearity reduces the HPA efficiency. Both spectral efficiency and energy efficiency are important aspects to consider for the massive battery-powered devices in the 5G network. Hence, it is necessary to analyse the GFDM performance with HPA and manage the trade-off between spectral and energy efficiency. The contribution from this research work is to

review a holistic performance to analyse spectral and energy efficiency of the GFDM system, where an optimal IBO is obtained. Numerical results indicate that the GFDM system with the designed filter has a better performance in all metrics than the one with RC filter.

Publications

Parts of the contents in this thesis have been previously published in the following journal or conference papers.

- Z. A. Sim, F. H. Juwono, R. Reine, Z. Zang and L. Gopal, "Performance of GFDM Systems Using Quadratic Programming Pulse Shaping Filter Design," in IEEE Access, vol. 8, pp. 37134-37146, 2020.

- Z. A. Sim, F. H. Juwono, R. Reine, Z. Zang and L. Gopal, "Reducing Out-of-Band Radiation in GFDM Systems Using Pulse Shaping Filter Design," 2019 25th Asia-Pacific Conference on Communications (APCC), Ho Chi Minh City, Vietnam, 2019, pp. 41-45.

- Z. A. Sim, R. Reine, Z. Zang, F. H. Juwono and L. Gopal, "Reducing the PAPR of GFDM Systems with Quadratic Programming Filter Design," 2019 IEEE 89th Vehicular Technology Conference (VTC2019-Spring), Kuala Lumpur, Malaysia, 2019, pp. 1-5.

- Z. A. Sim, R. Reine, Z. Zang and L. Gopal, "PAPR and BER reduction in MU-MIMO-OFDM systems via a set of waveforms," 2017 IEEE International Conference on Signal and Image Processing Applications (ICSIPA), Kuching, Malaysia, 2017, pp. 55-60.

Contents

List of Figures

List of Tables

Acronyms

4G	fourth generation
5G	fifth generation
ACLR	adjacent channel leakage ratio
AMI	average mutual information
AR	augmented reality
AWGN	additive white Gaussian noise
BER	bit error rate
BM	baseband modulator
BPSK	Binary Phase Shift Keying
CCDF	complementary cumulative distribution function
CCI	co-channel interference
CP	cyclic prefix
CSI	channel state information
DAB	digital audio broadcasting
DAC	digital-to-analog converter
DFT	discrete Fourier transform
DVB	digital video broadcasting
eMBB	enhanced mobile broadband
FBMC	Filter Bank Multicarrier
FET	field-effect transistor
FFT	fast Fourier transform

FIR	finite impulse response
GFDM	Generalized Frequency Division Multiplexing
HPA	high power amplifier
i.i.d.	independent and identically-distributed
IBO	input backoff
ICI	intercarrier interference
IDFT	inverse discrete Fourier transform
IFFT	inverse fast Fourier transform
IoT	Internet of Things
ISI	inter-symbol interference
LTE	Long Term Evolution
M2M	machine-to-machine
MIMO	multiple input multiple output
MMSE	minimum mean-squared error
mmWave	millimeter wave
MTC	machine-type communications
MUI	multiuser interference
MU-MIMO-OFDM	multiuser MIMO-OFDM
MU-OFDM	multiuser OFDM
NR	New Radio
OBO	output backoff
OFDM	Orthogonal Frequency Division Multiplexing
OOB	out-of-band
PAPR	peak-to-average power ratio
PSD	power spectral density
PTS	partial transmit sequence
QAM	Quadrature Amplitude Modulation
QP	quadratic programming
QPSK	Quadrature Phase Shift Keying

RC	raised cosine
SC-FDE	single carrier frequency domain equalization
SLM	selected mapping
SNR	signal-to-noise power ratio
SRRC	square root raised cosine
SSPA	solid-state power amplifier
TWTA	traveling wave tube amplifier
UFMC	Universal Filtered Multicarrier
VR	virtual reality
WiMAX	Worldwide Interoperability for Microwave Access
WLAN	wireless local area network

Chapter 1

Introduction

Today, mobile phones are capable of performing a large spectrum of applications, from simple applications such as sending instant messages, to complex applications such as mobile gaming with real-time interactions. It has become a necessity in most parts of the world, where each person will own an average of 3 devices [1]. On the other hand, machine-to-machine (M2M) communication devices has emerged as the fastest-growing device globally due to the rise in popularity of smart grids, smart cities, smart homes [2], [3]. According to the Cisco Annual Internet Report [1], there will be close to 30 billion connected devices globally by 2023, with M2M devices amounting to 50% of those devices followed by smartphones (including tablets) with a little less than 30%. The remainder goes to connected TVs, PCs and others.

To support the growing trends of these networked devices, research on enabling technologies for the upcoming fifth generation (5G) has been very active [4]–[12]. The development of previous generations of mobile communication networks has been focusing on increasing the data rate [8], [13]–[15]. In the 5G network, devices that are connected to the network are very diverse, thus they have different requirements and demands. Therefore, the upcoming 5G network must go beyond increasing data rates, and is required to satisfy some other requirements, though

not necessarily simultaneously. Some of the requirements of the 5G network are as follows:

- **Higher Data Rate** - The demand for high speed data remains a challenge with scarcity in spectrum. Driven by high definition (HD) video streaming services, augmented reality (AR), virtual reality (VR), and embedded videos in social platforms and advertisements, video traffic is projected to account for 76% of 160 EB mobile traffic per month in 2025 [16], with demands of greater than 100 Mbps data rate [1].
- **Low latency** - Synchronisation is required in wireless communication systems in order to reduce the intercarrier interference (ICI), but has a bulky synchronisation process. An asynchronous transmission is much more preferred for sporadic traffic or burst type transmissions in M2M communications to achieve the 1ms latency requirement [9], [11].
- **Scalibility** - With the massive amount of M2M communication devices, networks are expected to be extremely dense that need to support up to 10000 connections per macrocell [2], [10], [17].
- **High Power Efficiency** - Considering the carbon emission from power consumption of the massive number of devices, green technologies are required to reduce energy usage by 90% [12], [18], [19]. A power efficient system also ensures mobile devices and sensors have a longer battery life.

As the heterogeneity of traffic and applications make the already complicated network support even more challenging, new and innovative solutions are required for the 5G network. Several disruptive technologies are currently receiving interest in the design of the 5G network, such as the millimeter wave (mmWave), massive multiple input multiple output (MIMO), and advanced modulation techniques [7], [11], [12]. Among these technologies, the modulation techniques in communication systems constitute a major role in the system performance [9], [15], [20].

1.1 The Multicarrier Modulation System

The principle of multicarrier modulation systems is to divide a high-rate stream into a number of parallel low-rate substreams and transmit the streams them over a number of subchannels. By allowing the data streams to be transmitted at a low rate, the multicarrier signal is less sensitive to interference caused by multipath fading channels [21]. To recover the transmitted signal at the receiver, the multicarrier system only requires simple equalisation to mitigate channel fading [22]. Various multicarrier modulation systems exist in the literature for implementation in wireless communication systems [9], [11], [20], [23]–[29]. In this thesis, the research is focused on analysing the Orthogonal Frequency Division Multiplexing (OFDM) system and the Generalized Frequency Division Multiplexing (GFDM) system.

1.1.1 OFDM Overview

The OFDM system is one of the most well-known multicarrier modulation. In OFDM, the parallel substreams of a multicarrier system are mapped to a number of orthogonal subcarriers. The orthogonality of the subcarriers, as illustrated in Fig. 1.1, eliminates the need for the usage of guard bands between subcarriers, without introducing ICI. This shows that the OFDM system has a high spectral efficiency as most of the bandwidth can be used for data transmission. In terms of hardware implementation, the OFDM system can be easily implemented using the inverse fast Fourier transform (IFFT) and fast Fourier transform (FFT) [30], [31].

Due to its high spectral efficiency, robustness against multipath channel fading, and low implementation complexity, the OFDM system has gained popularity in wireless communication applications. With the successful implementation in digital audio broadcasting (DAB) and digital video broadcasting (DVB), the OFDM system has then been applied in high data rate applications such as World-

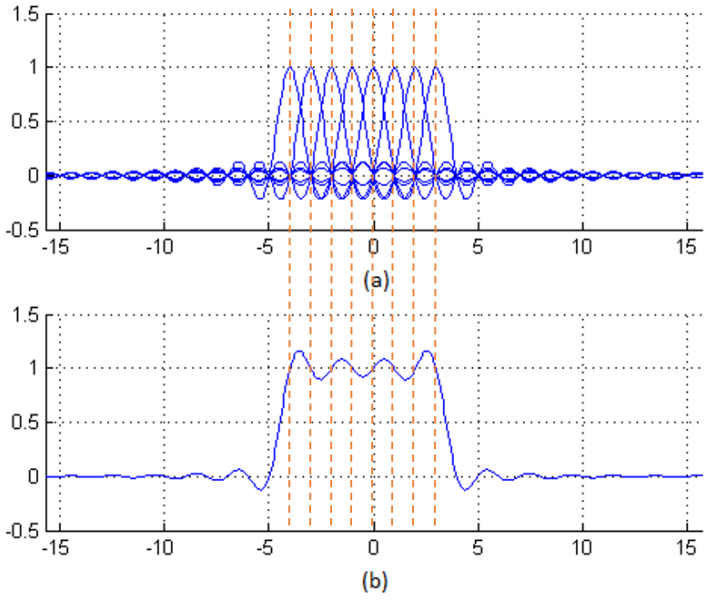

Figure 1.1: The peak of each subcarrier occurs at the zero-crossings of adjacent subcarriers due to orthogonality of the subcarriers.

wide Interoperability for Microwave Access (WiMAX) [32], [33], wireless local area network (WLAN) 802.11 WiFi [34], and Long Term Evolution (LTE) [13], [35].

Although the current OFDM system has various advantages, it struggles to satisfy the increasing demands and requirements of the 5G network. The 5G network is envisioned to be an evolution of the current communication standards which will be applied in wide range of emerging applications with diverse requirements and specifications [5]. Some of the key applications that are expected to be in the 5G network are the massive machine-type communications (MTC), enhanced mobile broadband (eMBB), and the tactile internet [9], [36]. Several requirements for the 5G network have been identified, which includes Gigabit connectivity, extremely low latency, low power consumption, and ability to handle massive connections [4], [37].

In the OFDM system, strict time and frequency synchronization is required to properly detect the transmitted signal. However, the bulky synchronization process is not suitable for sporadic traffic from Internet of Things (IoT) devices,

and for the low latency requirement in real-time applications [9], [36]. Additionally, the usage of rectangular filter in the OFDM system causes its amplitude to have abrupt discontinuity which induces spectral growth and lead to the high out-of-band (OOB) radiation. High OOB radiation will interfere with the adjacent channels. Guard bands can be placed between channels to minimize interference but this will reduce the bandwidth efficiency.

1.1.2 GFDM Overview

Due to the above-mentioned limitations with the OFDM system, several multicarrier modulation techniques have been considered as potential candidates for 5G, such as Filter Bank Multicarrier (FBMC), Universal Filtered Multicarrier (UFMC), and GFDM [9], [20], [27]–[29], [38]. The FBMC system shapes each subcarrier with a narrowband filter. However, it has a long impulse response which is not suitable for sporadic traffic from the IoT devices. UFMC does not require cyclic prefix (CP) which is good for spectral efficiency, and it uses filtering over a group of subcarriers. However, UFMC requires strict time-synchronization to reduce inter-symbol interference (ISI). GFDM is a flexible modulation technique that is able to adapt to different types of scenarios, such as high speed connectivity and very low latency. This is achieved by adjusting its system parameters. Data symbols in the GFDM system are divided into multiple subcarriers, with each subcarrier carrying multiple subsymbols.

The GFDM system was proposed by the Vodafone Chair Mobile Communications as an alternative multicarrier technique for future generation mobile networks [29]. In the GFDM system, the data symbols are arranged in a time and frequency block, where the data are transmitted over K number of subcarriers, with each subcarrier carrying M number of subsymbols. The total number of data symbols per GFDM block is $N = KM$. Let $x_{k,m}$ denote the data symbol that is transmitted on the kth subcarrier and mth subsymbol, the arrangement of subcarriers and subsymbols in GFDM compared with OFDM is as illustrated

in Fig. 1.2.

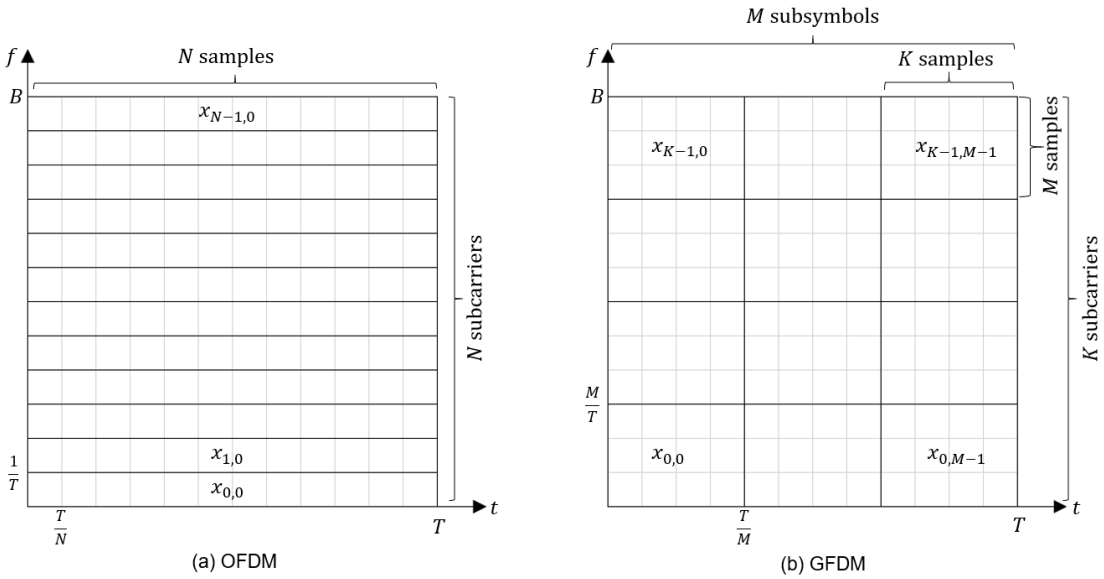

Figure 1.2: Arrangement of data symbols in time and frequency domain with (a) OFDM - $K = N = 12$ subcarriers, $M = 1$ subsymbol, (b) GFDM - $K = 4$ subcarriers, $M = 3$ subsymbols, $N = 12$.

The GFDM system adopts the advantageous properties of OFDM, with several added enhancements. The GFDM system has an added advantage in terms of the CP insertion. As illustrated in Fig. 1.3, with the same total number of data symbols, the GFDM system only requires the CP to be inserted once per block, while the OFDM system needs insert a CP after each time slot. This advantage in GFDM is essential as less time resource is consumed, and is particularly crucial in tactile internet where the data transmissions are burst-type [36].

1.2 The High PAPR in Multicarrier Signals

Despite the advantageous properties of multicarrier systems, they have two major drawbacks, which are sensitivity to frequency offset and having a high peak-to-average power ratio (PAPR). Frequency offset occurs due to Doppler shift and will cause synchronisation errors. The issue of frequency offset has been heavily researched and discussed, and many solutions have been proposed in the literature

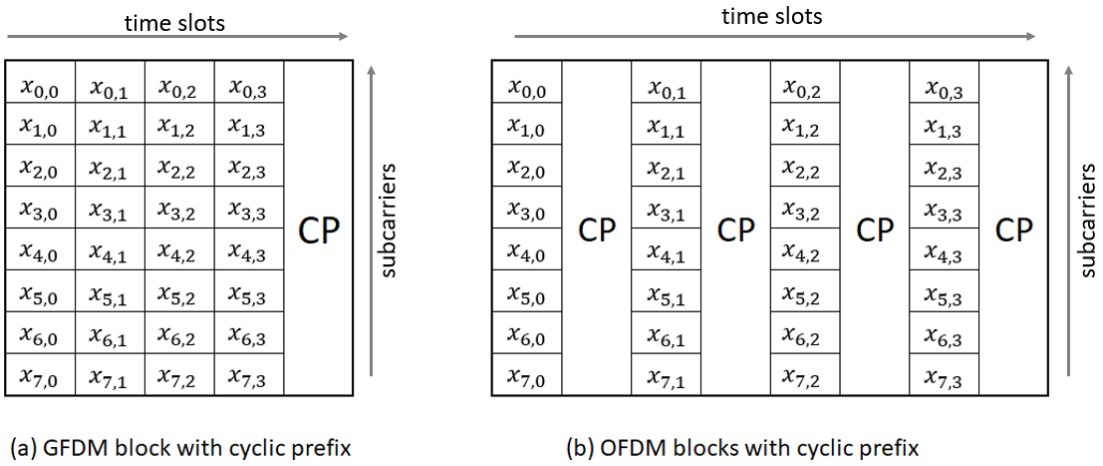

Figure 1.3: Cyclic prefix insertion in GFDM and OFDM systems.

to easily overcome the frequency offset in multicarrier systems, e.g., [39]–[42]. On the other hand, the PAPR remains a major issue in multicarrier systems as most of the existing solutions have their respective drawbacks, which is further discussed in Chapter 2. Since both the OFDM and GFDM systems are multicarrier systems, they also suffer from frequency offset and a high PAPR.

When the subcarriers of multicarrier systems are added up coherently in the time domain, a signal with large variations such as that shown in Fig. 1.4 will be produced. In a typical communication system, the transmit signal is amplified by a nonlinear high power amplifier (HPA) before it is transmitted over the channel. When a signal with a high PAPR is passed through the HPA, signal power exceeding the linear region of the HPA may cause distortion to the transmitted signal. This is because when a certain portion of the time domain signal is modified or clipped, it will affect the entire frequency band.

A higher input backoff (IBO) can be applied to allow a signal with higher power to go through the HPA's linear region. However, large IBO in multicarrier signals often results in very low HPA efficiency, with an efficiency of lower than 10% when a Class-A HPA is used [43]. The low efficiency of the HPA indicates that most of the power supplied to the HPA is wasted as heat, which is not energy efficient especially at the base station where more than half of the power

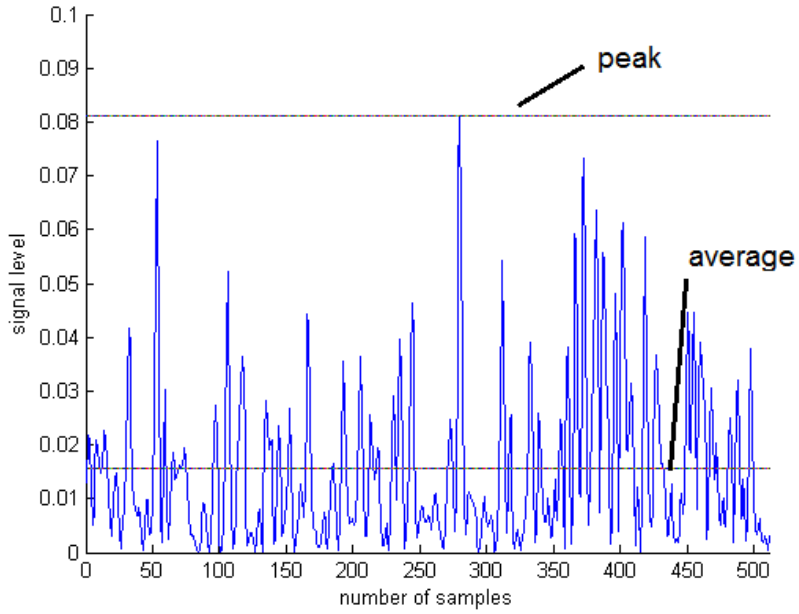

Figure 1.4: Peak power and average power levels in a multicarrier signal.

consumption is by the HPA [44]. Smart or complex HPA can be used where the input power is adjusted according to the signal but these type of amplifiers are costly. Energy efficiency plays a major factor for mobile devices and low power sensors as they have limited battery life. Hence, a better solution for high PAPR in OFDM systems is to reduce the PAPR before the signal passes through the HPA.

1.3 Thesis Objectives

The main objectives of this thesis are

- to design causal pulse shaping filter to reduce the PAPR of the MU-OFDM and the GFDM transmitted signals using computationally efficient optimisation approach
- to investigate the performance of the designed filter in the MU-OFDM and the GFDM systems
- to investigate the performance of the designed filters in GFDM systems in

order to find the optimal trade-off for energy and spectrum efficiency when HPA is applied

1.4 Thesis Overview and Contributions

The pulse shaping technique is effective in reducing the PAPR of multicarrier systems by shaping the data symbols using a set of properly selected filters. This thesis proposes to design optimal causal pulse shaping filters for multicarrier systems to reduce the PAPR of the transmitted signal.

Chapter 2 discusses some of the common techniques for reducing the high PAPR of the multicarrier transmitted signal and analyses the effectiveness of the pulse shaping technique in reducing the PAPR in OFDM and GFDM transmitted signals. Chapter 3 illustrates the PAPR reduction of multiuser OFDM (MU-OFDM) signals and multiuser MIMO-OFDM (MU-MIMO-OFDM) using a set of causal pulse shaping waveform. In Chapter 4, the GFDM system is investigated and a causal pulse shaping filter is designed to reduce the PAPR of the GFDM signal as well as the OOB radiation. Chapter 5 analyses the impact of nonorthogonality from pulse shaping technique in GFDM. Chapter 6 presents a holistic investigation of the impact of the PAPR on the GFDM system performance in presence of HPA nonlinearity. Chapter 7 summarises this thesis and highlights some potential future research.

Chapter 2: Pulse Shaping for PAPR Reduction

In this chapter, an overview of existing PAPR reduction techniques is presented. This is followed by an investigation on the pulse shaping technique in OFDM systems. By using a set of properly selected pulse shaping filters, the PAPR of the OFDM transmitted signal can be reduced significantly. The effectiveness of the pulse shaping technique in GFDM systems is then analysed.

Chapter 3: Filter Design for Multiuser OFDM

In this chapter, the pulse shaping technique is applied onto the MU-OFDM system to reduce the PAPR of its signal. As existing ideal Nyquist filters shapes are non-causal, a set of causal pulse shaping filters are designed using min-max optimisation approach. The designed pulse shaping filters are also extended to MU-MIMO-OFDM systems to analyse the PAPR when MIMO is added into the system. Simulation results indicate that the designed pulse shaping filters are able to reduce the PAPR while improving the bit error rate (BER) performance when the OFDM signal is transmitted over a multipath fading channel.

Chapter 4: Filter Design for GFDM Systems

Besides the need to have a low PAPR, it is also essential to ensure that the multicarrier system has a low OOB radiation for better spectral efficiency. The GFDM system is a potential 5G candidate which uses non-causal pulse shape filtering to enhance the overall system performance. In this chapter, the quadratic programming filter design is applied to design a causal pulse shaping filter for GFDM in order to reduce the PAPR and OOB radiation of the GFDM system. Simulation results show that the designed pulse shaping filter reduces the PAPR of the GFDM signal as compared with using the raised cosine (RC) filter.

Chapter 5: GFDM Receiver Performance with Designed Filter

Designing an optimum pulse shaping filter for the GFDM system gives desirable PAPR and OOB radiation performance. Therefore, it is meaningful to analyse the BER performance at the receiver. The implementation of filtering using the ideal RC filter and the designed filter in the GFDM system can result in self interference. An iterative algorithm can be applied to mitigate the self interference.

Chapter 6: Impact of the PAPR Towards HPA Nonlinearity

In a practical wireless communication system, the HPA is used to amplify the transmit signal prior to the actual transmission. The nonlinear characteristics of the HPA will affect the overall quality of the signal. Generally, a lower PAPR is desired to minimize the effects of nonlinearity, such as spectral regrowth and increase in BER. The GFDM system has a PAPR that is higher than the OFDM system, but has a much lower OOB radiation. Hence, in this chapter, a holistic approach is applied to investigate the performance of GFDM system by considering the HPA nonlinearity. The performance of the GFDM system using the designed filter is compared with the GFDM system using the ideal RC filter. Numerical examples show that the designed filter has a better overall performance than the ideal RC filter in a GFDM system in the presence of HPA nonlinearity.

Chapter 2

Pulse Shaping for PAPR Reduction

This chapter presents various PAPR reduction techniques and analyses the effectiveness of the pulse shaping technique in reducing the PAPR of the OFDM and GFDM transmitted signal. The rest of this chapter is organised as follows: Section 2.1 presents an overview of PAPR reduction and reviews several common PAPR reduction techniques. Section 2.2 analyses the pulse shaping technique to reduce the PAPR of the OFDM transmitted signal. Section 2.3 investigates the effectiveness of the pulse shaping technique in reducing the PAPR of GFDM signals. Finally, concluding remarks are drawn in Section 2.4.

2.1 Overview of PAPR Reduction

Various approaches have been proposed in the literature to reduce the high PAPR in multicarrier systems [31], [45]–[47]. Generally, PAPR reduction techniques can be divided into three categories [46], [48]: 1) Signal distortion techniques such as clipping and filtering, peak windowing, and companding transform; 2) Distortionless or probabilistic techniques such as selected mapping (SLM), partial transmit

sequence (PTS), and tone reservation; 3) Coding or signal scrambling techniques such as turbo coding, Golay complementary sequences, and Barker Codes. Clipping and filtering are able to significantly reduce the PAPR by limiting the peak levels of the transmit signal [49]–[53], but results in intermodulation between subcarriers and will cause spectral regrowth in the stopband. Filtering is used to reduce the negative effects of clipping but this introduces additional complexity at the receiver [49], [50], [52]. In SLM [54], [55] and PTS [56], [57], copies of the data block are generated and mapped onto different type of transform vectors. The combination which has the lowest PAPR performance is selected for transmission. However, side information is needed to be transmitted which takes up bandwidth, and the redundant copies increases the computational complexity.

Shaping the subcarriers using a set of properly selected pulse shaping filters have been shown to be effective in reducing the PAPR of the OFDM and GFDM transmit signals [58]–[62]. The pulse shaping technique can be considered as a precoding approach [63], and can be implemented with minimal increase in computational complexity. This thesis focuses on using the pulse shaping technique to reduce the PAPR of the multicarrier transmitted signals.

2.2 Pulse Shaping in OFDM System

2.2.1 OFDM System Model

A single user OFDM transmitter with K subcarriers of duration T is as shown in Fig 2.1. The input data is first modulated by a baseband modulator (BM) according to its modulation scheme, Binary Phase Shift Keying (BPSK), Quadrature Phase Shift Keying (QPSK), or Quadrature Amplitude Modulation (QAM). The modulated data is divided into K number of symbols, $\vec{x} = \{x_0, x_1, \ldots, x_{K-1}\}^T$, which will be carried by K subcarriers. The subcarriers are shifted to their respective carrier frequencies using the IFFT, which is represented by the exponential term, $e^{j2\pi kt/T}$. The subcarriers are then summed and transmitted in parallel as

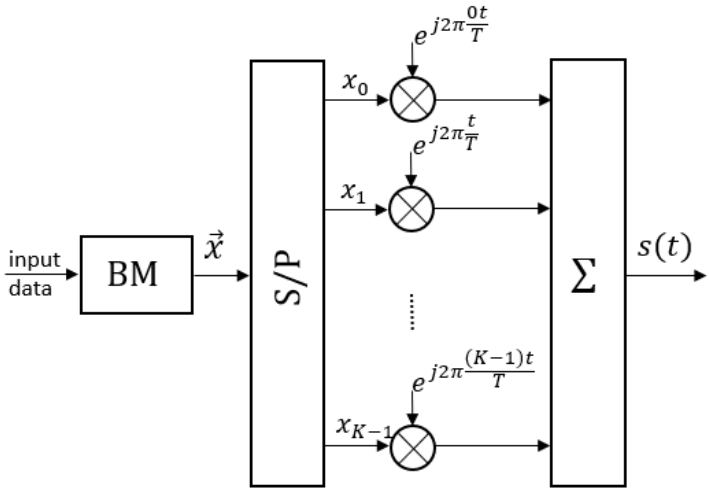

Figure 2.1: Conventional OFDM transmitter system model.

$s(t)$. The baseband equivalent of a single user continuous OFDM transmitted signal can be expressed as

$$s(t) = \sum_{k=0}^{K-1} x_k e^{\frac{j2\pi kt}{T}}, \qquad 0 \leq t \leq T \tag{2.1}$$

where $k = 0, 1, 2, \ldots, K-1$ represents the subcarriers. The discrete OFDM transmitted signal of (2.1) can be expressed as

$$s[n] = \sum_{k=0}^{\mathcal{L}K-1} x_k e^{\frac{j2\pi kn}{\mathcal{L}K}} \qquad 0 \leq n \leq \mathcal{L}K-1 \tag{2.2}$$

where $s[n] = s(nT/\mathcal{L}K)$, n is the sampling index, and $\mathcal{L}$ denotes the oversampling factor. The number of samples within an OFDM block is $N = \mathcal{L}K$.

2.2.2 OFDM with Pulse Shaping System Model

The block diagram of the OFDM transmitter with pulse shaping is illustrated in Fig. 2.2. The baseband equivalent of the continuous OFDM transmitted signal with pulse shaping can be expressed as

$$s(t) = \sum_{k=0}^{K-1} x_k p_k(t) e^{\frac{j2\pi kt}{T}}, \quad 0 \leq t \leq T, \tag{2.3}$$

where $p_k(t)$ is the pulse shaping filter used to shape subcarrier k.

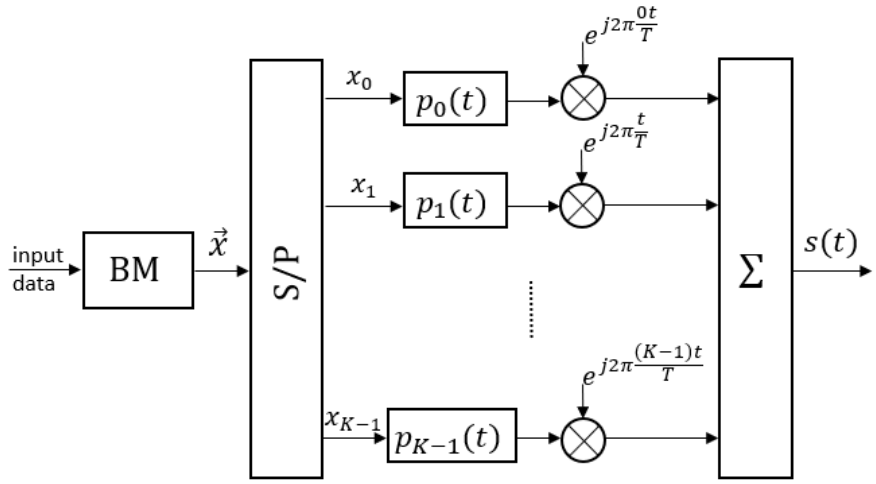

Figure 2.2: System model of single user OFDM with pulse shaping.

The general idea of pulse shaping is to shape each subcarriers in such a way that the peaks of each subcarriers do not coincide when summed up coherently [59]. In order to reduce the PAPR in OFDM systems, a proper selection of pulses is required. The pulse shape, $p(t)$, has to be a time limited waveform of duration T, with

$$p(t) = 0, \qquad t < 0, t > T \tag{2.4}$$

and

$$\int_0^T |p(t)|^2 dt = T. \tag{2.5}$$

Using extension by periodicity, a periodic function with period T is defined as

$$\omega(t) = \sum_{i=-\infty}^{+\infty} p(t - iT) \tag{2.6}$$

which leads to the pulse shape of subcarrier k as

$$p_k(t) = \omega(t - kT_s) \sqcap_T (t - \frac{T}{2}), \quad k = 0, 1, \ldots, K-1 \tag{2.7}$$

where $T_s = \frac{T}{K}$ is the symbol duration of the baseband signal, and

$$\sqcap_T (t) = \begin{cases} 1, -\frac{T}{2} \leq t \leq \frac{T}{2} \\ 0, \text{elsewhere.} \end{cases} \tag{2.8}$$

To generate a different pulse shaping waveform for each subcarrier, the prototype pulse is cyclic shifted for every subcarrier. When a set of pulse shapes (that are cyclic shifts of each other) with

$$p_k(t) = \begin{cases} \omega(t - kT_s) & 0 \leq t \leq T = KT_s \\ 0 & \text{elsewhere} \end{cases} \tag{2.9}$$

is applied to an OFDM system with K subcarriers, where $\omega(t)$ is a periodic function with period T, the maximum PAPR of the transmitted OFDM signal is upper bounded by [58]

$$PAPR_{max} \leq K \tag{2.10}$$

with equality when a rectangular pulse shape is used. This shows that different type of pulse shapes can be used for PAPR reduction in OFDM systems. Therefore, many other researchers in references [64]–[66] had conducted extensive research into this technique.

In order to prevent ISI, filters used in the pulse shaping technique will need to satisfy the Nyquist Criterion. Filters that satisfy the Nyquist Criterion are called Nyquist filters. The Nyquist Criterion, or the Nyquist condition for zero ISI is given as [67]

$$p(nT) = \begin{cases} 1 & n = 0 \\ 0 & n \neq 0. \end{cases} \tag{2.11}$$

2.2.3 PAPR of OFDM Transmitted Signal

The PAPR of a discrete OFDM transmitted signal, $s[n]$, is described as the ratio between the peak power, $\max|s[n]|^2$, and the average power, $E\{|s[n]|^2\}$, which can be written as [31]

$$PAPR = \frac{\max|s[n]|^2}{E\{|s[n]|^2\}}, \tag{2.12}$$

where $E\{|s[n]|^2\}$ denotes the expectation or mean of the OFDM transmitted signal. In order for the discrete signal, $s[n]$, to have close approximation to the continuous signal, $s(t)$, oversampling $\mathcal{L} = 4$ is required. Without oversampling, it will result in a lower PAPR which does not represent the PAPR of a continuous signal [45], [53], [68]. In this thesis, oversampling $\mathcal{L}$ is used for simulations; but the notations of oversampling is not going to be mentioned for simplicity.

Due to the superposition of subcarriers in the OFDM system, the OFDM transmitted signal will have a higher PAPR when there is a larger number of subcarriers. However, the PAPR of the OFDM signal is determined by the single largest-amplitude sample in a block of $\mathcal{L}N$ samples. As the number of subcarriers in an OFDM system gets increasingly large, the probability of the highest peak value occurring in the multicarrier system becomes negligible.

A more meaningful approach is by taking the complementary cumulative distribution function (CCDF) of the OFDM transmitted signal amplitude that is measured over many samples, given as

$$\begin{aligned} CCDF_{PAPR}(PAPR_0) &= Pr(PAPR \geq PAPR_0) \\ &= Pr\left(\frac{\max|s[n]|^2}{\mathrm{E}\{|s[n]|^2\}} \geq PAPR_0\right), \end{aligned} \tag{2.13}$$

where the probability of the PAPR of the multicarrier signal, $s[n]$, exceeding a given PAPR threshold, $PAPR_0$, is analysed.

To minimise the PAPR of the OFDM transmitted signal using pulse shaping,

the pulse shaping filter needs to be properly selected. The sinc filter is a filter ideally suited for communications due to the sharp edges of its corresponding frequency response (brick-wall filter), which are very bandwidth efficient as a bandpass filter [69]. On the other hand, the sinc filter has an infinitely long impulse response and can only be implemented by approximation.

The RC filter [69] is commonly used in communication systems instead of sinc filters. The RC filter adjusts the edges of the filter frequency response using roll-off factor parameter, $0 \leq \beta \leq 1$, by allowing the frequency response to occupy additional bandwidth. A roll-off factor of $\beta = 0$ will correspond to a brick-wall filter, while $\beta = 1$ is referred to as a pure raised cosine with smooth edges that spans to double of the original bandwidth. In practical implementations, the square root raised cosine (SRRC) [70] is used at both the transmitter and receiver, in order to get the RC filter as the desired resultant filter after matched filtering.

Various filters have been proposed in the literature to improve the system performance, such as the "better than" raised cosine filter [71], Xia filter [72], and flipped-hyperbolic secant (fsech) filter [73]. As illustrated in Fig. 2.3, the PAPR reduction performance of the RC and SRRC are better than the "improved" filters such as the Xia filter. This shows that some pulse shaping filters, such as the Xia filter, have better performance in other metrics, but is not desirable for reducing the high PAPR of the OFDM signal.

In the RC and SRRC filter, one of the parameters that can affect the PAPR of the OFDM transmitted signal when pulse shaping is applied is the roll-off factor of the pulse shaping filter, β. The PAPR of the OFDM transmitted signal with the SRRC filter using different roll-off factors, $\beta = \{0.1, 0.3, 0.5\}$, is as illustrated in Fig. 2.4. A larger roll-off factor may occupy more bandwidth, but has a better impulse response.

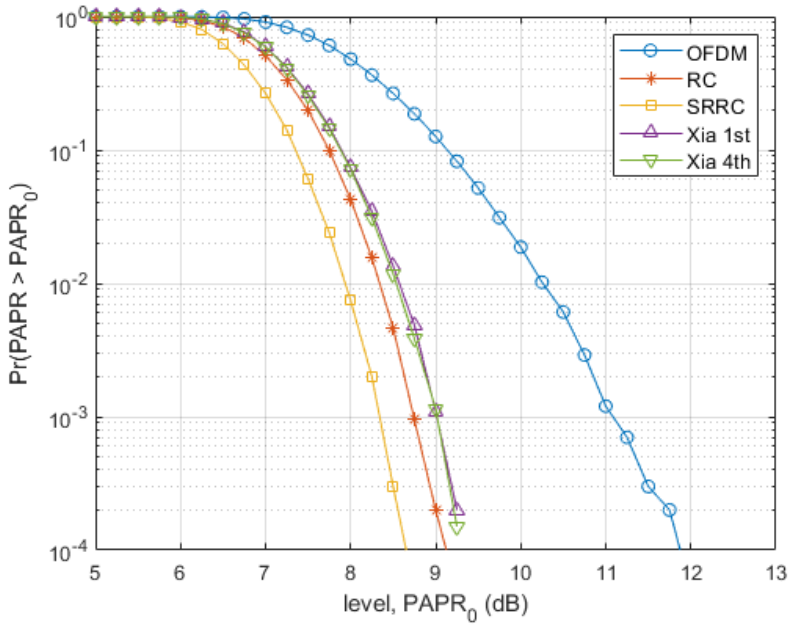

Figure 2.3: PAPR of OFDM transmitted signals using different pulse shaping filters.

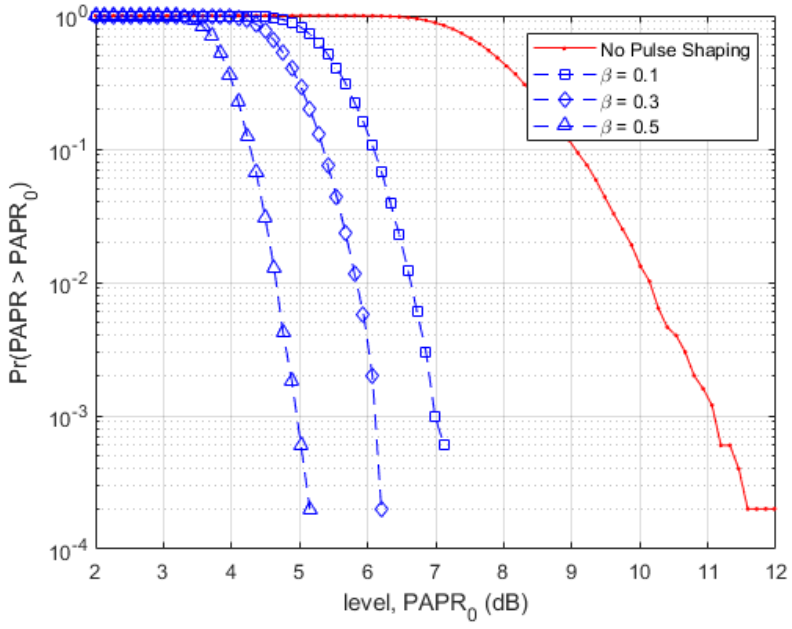

Figure 2.4: PAPR of OFDM transmitted signals with pulse shaping with N = 128 subcarriers.

2.3 Pulse Shaping in GFDM Systems

2.3.1 GFDM System Model

Consider a GFDM system, as illustrated in Fig. 2.5, where M denotes the number of subsymbols and K denotes the number subcarriers with $N = MK$. The input data stream consists of N elements and modulated using QPSK modulation. The input data vector can be represented as $\vec{x} = (x_0, x_1, \ldots, x_{N-1})^T$. The data stream is then mapped to a $K \times M$ matrix $\mathbf{x}$ using a serial-to-parallel converter, denoted as S/P, where $x_{k,m}$ denotes the data symbol transmitted at the k^{th} subcarrier at the m^{th} subsymbol. Each data symbol is then shaped by a pulse shaping filter, given as

$$p_{k,m}[n] = p[(n - mK) \mathrm{mod} N] e^{-j2\pi n \frac{k}{K}} \tag{2.14}$$

where each pulse $p_{k,m}[n]$ is shifted in time and frequency based on the prototype pulse shaping filter, $p[n]$, with n denoting the sampling index. The modulo operator performs the circular time shifting in time domain for different m subsymbol, while the exponential term performs the frequency shifting in time domain for each k subcarrier. The GFDM transmitted signal is obtained by summing all subcarriers and subsymbols. The baseband equivalent of the discrete GFDM transmitted signal is given as [74]

$$s[n] = \sum_{k=0}^{K-1} \sum_{m=0}^{M-1} p_{k,m}[n] x_{k,m}, \quad n = 0, 1, \ldots, N-1. \tag{2.15}$$

From (2.15), it can be observed that the equation is similar to OFDM, with an additional parameter, the subsymbol M. In the GFDM system, the duration of the GFDM block is divided into M number of time slots. In the case of $M = 1$, $K = N$, and a rectangular pulse is used as the pulse shaping filter, $p[n]$, (2.15) will be reduced to a conventional OFDM system as in (2.2).

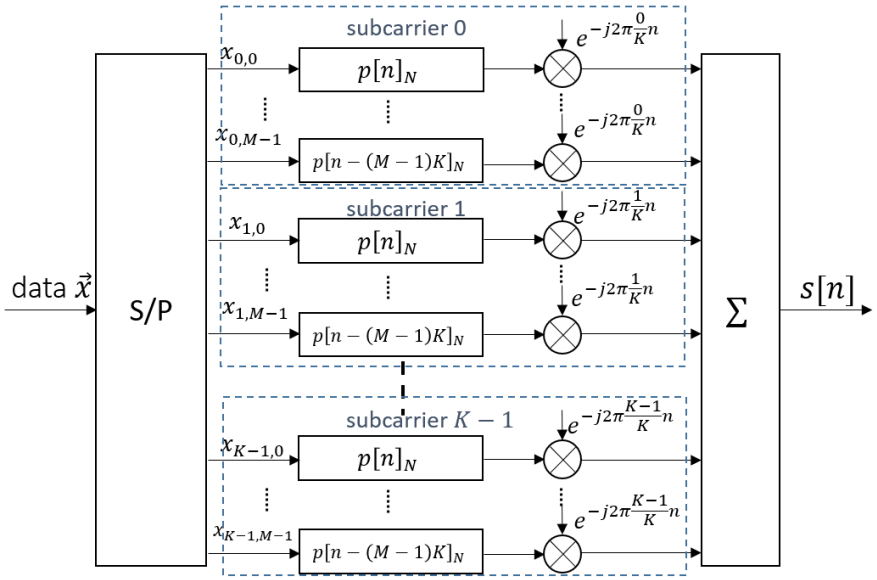

Figure 2.5: GFDM System Model.

2.3.2 PAPR of GFDM Transmitted Signal

The PAPR of a GFDM transmitted signal is analysed the same way as that of the PAPR of an OFDM transmitted signal as given in (2.12), except that the transmitted signal, $s[n]$, is following the GFDM equation in (2.15). In a conventional GFDM system, pulse shaping is integrated within the system model, as shown in Fig. 2.5. Different pulse shaping filters can be used as the prototype filter, $p[n]$, but analysis is performed on the RC filter due to its widespread usage [61], [62].

In the GFDM system, the roll-off factor also affects the PAPR. In Fig. 2.6, a larger roll-off will also produce a reduced PAPR, similar to the pulse shaping in OFDM. However, when using greater number of data symbols, the PAPR is increased when the roll-off factor increases. This is shown in Fig. 2.7. It can also be observed that the PAPR of the GFDM transmitted signal is higher than the PAPR of the OFDM transmitted signal when data symbols is greater, which is due to the structure of the GFDM filtering [75], [76]. In most high speed applications, the number of data symbols within a data block is high. Therefore, it is essential to reduce the PAPR of the GFDM signal.

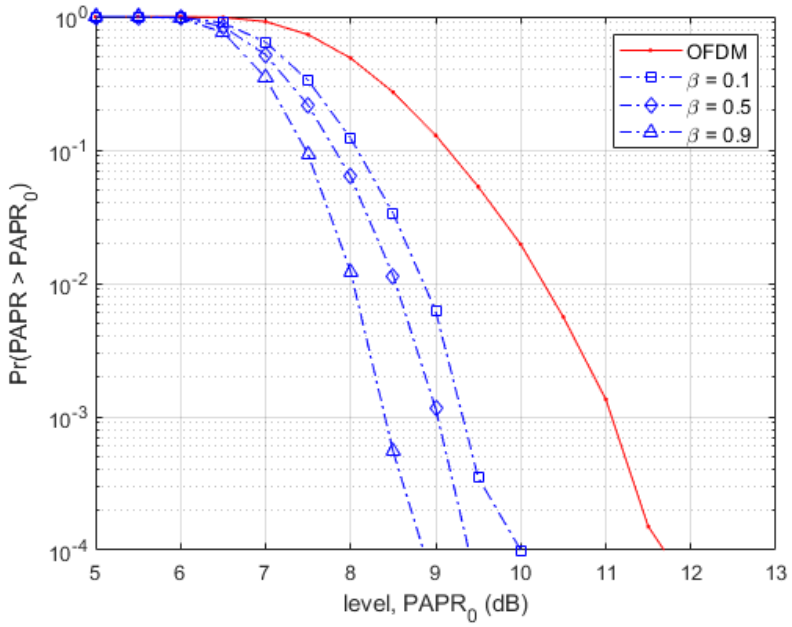

Figure 2.6: PAPR of GFDM transmitted signal with different roll-off factors, number of subcarriers K = 4, number of subsymbols M = 64.

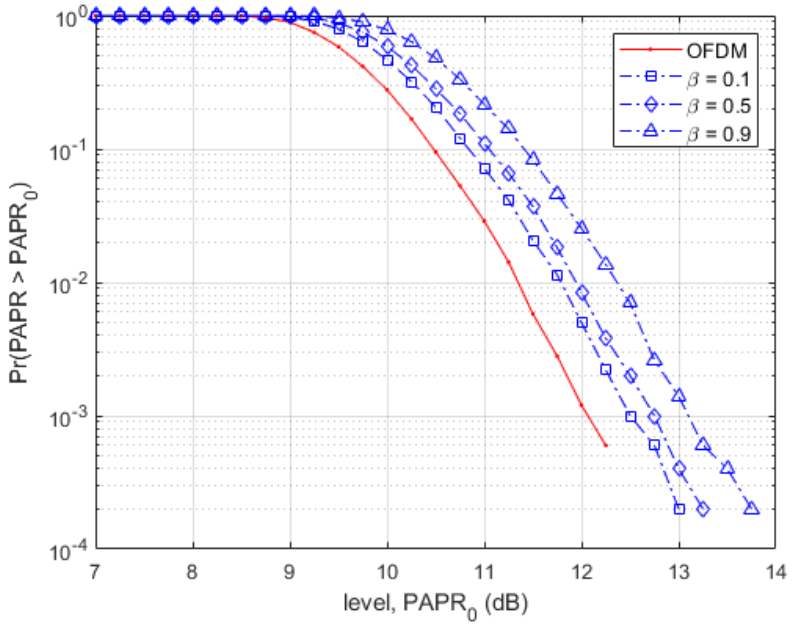

Figure 2.7: PAPR of GFDM transmitted signal with different roll-off factors, number of subcarriers K = 128, number of subsymbols M = 15.

2.4 Concluding Remarks

In this chapter, the effectiveness of the pulse shaping technique in reducing the PAPR of the OFDM and GFDM transmitted signal is investigated. The impact of using different pulse shaping filters in reducing the PAPR is also analysed. It has been shown that the RC filter with roll-off $\beta = 0.1$ can reduce the PAPR of the OFDM transmitted signals by 4 dB. Whereas in the GFDM system, the same filter reduces the PAPR of the transmitted signal by about 1.6 dB for $N = 256$ data symbols, while it increases the PAPR by about 0.5 dB for $N = 1920$ data symbols, when compared with the OFDM system.

Chapter 3

Filter Design for Multiuser OFDM

Ideal pulse shaping filters are not causal and are often approximated for practical implementations by truncating and shifting the ideal filters. However, truncation and shifting will introduce spectral regrowth and delay in the system. Instead of using non causal ideal filters, causal filters were designed to reduce the PAPR of the OFDM transmitted signal [66], [77]. However, these works focused on the single user OFDM system model. As the number of mobile users are constantly increasing, the conventional OFDM system needs to incorporate multiuser systems to accommodate more users. In the MU-OFDM system, the bandwidth is shared among multiple users, thereby increasing the user capacity of a given channel.

In this chapter, a set of pulse shaping filters is designed for MU-OFDM systems to reduce the PAPR of the transmitted signal. In the MU-OFDM system, it is important for the data of each user to be distinguished from the data of other users to prevent distortion [78]. The filter designs in [66], [77] cannot be applied directly for the MU-OFDM systems as they were designed for single user and did not consider user indpenedence.

The rest of the chapter is organised as follows: Section 3.1 presents the MU-OFDM system model. Section 3.2 illustrates the pulse shaping technique in the MU-OFDM system. Section 3.3 presents the design of the pulse shaping filter set using a computationally efficient optimisation approach and the effectiveness of the designed filters in reducing the PAPR of the MU-OFDM signal. In Section 3.4, the pulse shaping technique with the designed pulse shaping filter set is extended to the MU-OFDM systems with MIMO. Finally, concluding remarks are drawn in Section 3.5.

3.1 MU-OFDM System Model

Consider the system model for the transmitter of a downlink MU-OFDM system with U users utilizing the system, as illustrated in Fig 3.1. The transmitter accommodates data from multiple users by summing all users' data and transmits them as an entity. Assuming the subcarrier allocation for each user is fixed, each user is allocated K_u subcarriers, where $K_u = \frac{K}{U}$. The continuous-time representation of the MU-OFDM downlink transmitted data can be written as

$$s(t) = \sum_{u=1}^{U} s^u(t), \tag{3.1}$$

where $s^u(t)$ is the OFDM signal of the uth user expressed as

$$s^u(t) = \sum_{k=0}^{K_u-1} X_k^u e^{\frac{j2\pi\kappa t}{T}}, \tag{3.2}$$

where $\kappa = (u-1)K_u + k$. The discrete MU-OFDM transmit signal is expressed as

$$s[n] = \sum_{u=1}^{U} s^u[n], \tag{3.3}$$

with

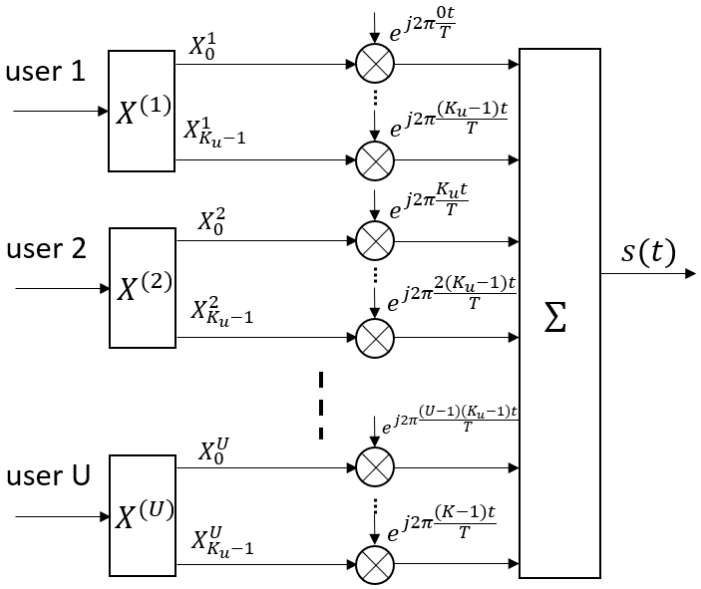

Figure 3.1: Conventional downlink MU-OFDM transmitter.

$$s^u[n] = \sum_{k=0}^{K_u-1} X_k^u e^{\frac{j2\pi\kappa n}{K}}. \tag{3.4}$$

The transmitter will process each users' data individually before summing them up for transmission.

3.2 Pulse Shaping in MU-OFDM systems

The pulse shaping technique is performed by convolution of the pulse shaping filter with the data symbols in the time domain. Convolution is a computationally exhaustive process. To simplify the pulse shaping technique, the convolution can be converted into multiplication by implementing the pulse shaping technique in the frequency domain and defining it as a matrix [63]. The pulse shaping matrix of each user, $\mathbf{P^u}$, can be extracted from a principle pulse shaping filter using [63]

$$P_{i,m}^u = P_{i,0}^u e^{-j2\pi\frac{im}{K}}, \tag{3.5}$$

where $P_{i,0}^u$ is the principle filter for the uth user, $i = \{0, 1, \ldots, L_u - 1\}$, $m =$

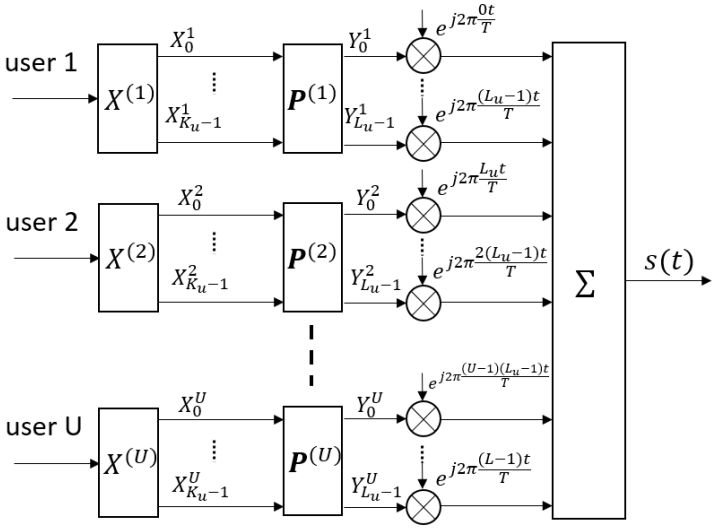

Figure 3.2: System model of MU-OFDM with pulse shaping.

$\{0, 1, \ldots, K_u - 1\}$, with $L_u = \beta K_u$. The exponential operator performs the cyclic shifting in time domain, such that the peaks of the filter impulse response do not coincide when summed up coherently. Hence, the PAPR of the MU-OFDM signal can be reduced.

The pulse shaping matrix (3.5) can be regarded as precoding [63]. Precoding spreads the data symbol over multiple subcarriers, resulting in crosstalk between the data symbols. To mitigate this, the pulse shaping matrix has to be an orthogonal matrix, which satisfies

$$(\mathbf{P}^u)^* \mathbf{P}^u = \mathbf{I}, \tag{3.6}$$

where $\mathbf{I}$ is an $K_u \times K_u$ identity matrix, and $(\mathbf{P}^u)^*$ represents the Hermitian transpose of $\mathbf{P}^u$.

The system model of the MU-OFDM signal with pulse shaping is illustrated in Fig. 3.2 and the transmit signal can be expressed as

$$s(t) = \sum_{u=1}^{U} s^u(t), 0 \leq t \leq T, \tag{3.7}$$

where $s^u(t)$ is the transmitted signal for each user, given as

$$s^u(t) = \sum_{i=0}^{L_u-1} Y_i^u e^{j2\pi\iota\frac{t}{T}}, \tag{3.8}$$

with $\mathbf{Y}^u = \mathbf{P}^u\mathbf{X}^u = [Y_0^u, Y_1^u, \ldots, Y_{L_u-1}^u]^{\mathrm{T}}$, where $\iota = (u-1)L_u + i$. The discrete representations for (3.7) and (3.8) can be written, respectively, as

$$s[n] = \sum_{u=1}^{U} s^u[n], 0 \leq n \leq \mathcal{L}K, \tag{3.9}$$

and

$$s^u[n] = \sum_{i=0}^{L_u-1} Y_i^u e^{j2\pi\iota\frac{n}{\mathcal{L}K}}. \tag{3.10}$$

3.3 Pulse Shaping Filter Set Design for MU-OFDM

In an MU-OFDM system, data corresponding to different users must be separated so that they do not interfere with each other. This can be achieved by taking into account the orthogonality of users [78]. In the pulse shaping waveform set design, the waveforms must be self orthogonal and mutually orthogonal over a range of symbol intervals. To achieve this, correlation constraints, i.e. autocorrelation and cross-correlation from the designed waveforms, can be employed in order to reduce the interferences in an MU-OFDM system.

The autocorrelation function of each waveform should be small at all non-zero translates of multiple symbol intervals to ensure self orthogonality, which minimises ISI. The autocorrelation of each waveform is calculated by multiplying the waveform to its delayed waveform. On the other hand, the cross-correlation function between any pair of waveform should have low values for all translates of multiple symbol intervals to minimise co-channel interference (CCI). The cross-correlation is calculated by multiplying one waveform with the next designed waveform.

The significance of correlation constraints in a multiuser system is shown in [79] by considering a two-user multicarrier communications system. The demodulated data at the receiver of user 1 is denoted as $\hat{\mathbf{d}}_\mathbf{1}$ with

$$\hat{\mathbf{d}}_\mathbf{1} = \mathbf{R_{ac}}\mathbf{d_1} + \mathbf{R_{cc}}\mathbf{d_2}, \tag{3.11}$$

where $\mathbf{d_1}$ is the transmitted data from user 1 and $\mathbf{d_2}$ is the transmitted data from user 2. Both $\mathbf{d_1}$ and $\mathbf{d_2}$ are represented as a vector with $\mathbf{d_u} = d_u(0), d_u(1), \ldots, d_u(N)$, where N is the number of subcarriers. $\mathbf{R_{ac}}$ and $\mathbf{R_{cc}}$ are the autocorrelations and cross-correlations with respect to user 1, respectively, which are given as

$$\mathbf{R_{ac}} = \begin{bmatrix} R_{ac}(0) & R_{ac}(D) & \ldots & R_{ac}((N-1)D) \\ R_{ac}(-D) & R_{ac}(0) & \ldots & R_{ac}((N-2)D) \\ \vdots & \vdots & \ddots & \vdots \\ R_{ac}((N-1)D) & R_{ac}((N-2)D) & \ldots & R_{ac}(0) \end{bmatrix} \tag{3.12}$$

$$\mathbf{R_{cc}} = \begin{bmatrix} R_{cc}(0) & R_{cc}(D) & \ldots & R_{cc}((N-1)D) \\ R_{cc}(-D) & R_{cc}(0) & \ldots & R_{cc}((N-2)D) \\ \vdots & \vdots & \ddots & \vdots \\ R_{cc}((N-1)D) & R_{cc}((N-2)D) & \ldots & R_{cc}(0) \end{bmatrix} \tag{3.13}$$

In the case when the autocorrelation function and cross-correlation function are minimised, $\mathbf{R_{ac}}$ will be an $N \times N$ identity matrix, and $\mathbf{R_{cc}}$ will be a zero matrix. This indicates that the system is free of ISI and CCI. Hence, user 1 will be able recover its original data.

The design of a set of filters can be generalized as the design of a set of filters with specified constraints in time and frequency domain [80]. The objective of the design problem is to minimise the stopband energy of the designed pulse

shaping waveforms while maintaining spectral shaping efficiency. In order to reduce multiuser interference (MUI), this set of waveforms should maintain self orthogonality and mutual orthogonality over a range of symbol shifts. Correlation constraints are introduced in the problem formulation in order to minimize ISI and CCI. The pulse shaping waveforms are specified to have low autocorrelation values at nonzero translates of multiple symbol interval and low cross-correlation values at all translates of multiple symbol intervals.

3.3.1 Problem Formulation

For any u, the M-tap finite impulse response (FIR) filter $P_u(e^{j\omega})$ is defined as

$$P_u(e^{j\omega}) = \sum_{m=0}^{M-1} h_u(m)\phi_m(e^{j\omega}) = \mathbf{h}_u^{\mathrm{T}}\phi(e^{j\omega}) \tag{3.14}$$

where $h_u = [h_u(0), h_u(1), \ldots, h_u(M-1)]^{\mathrm{T}}$ and $\phi = [\phi_0, \phi_1, \ldots, \phi_{M-1}]^{\mathrm{T}}$, given that $\phi_m(e^{j\omega}) = e^{-j\omega m}, m = 0, 1, 2, \ldots$, and $\phi_m(e^{j\omega})$ is a set of orthogonal basis functions. Consider the following filter set design problem, denoted as Problem (PU).

Problem(PU). Design a set of U filters $\{P_1(e^{j\omega}), P_2(e^{j\omega}), \ldots, P_U(e^{j\omega})\}$ which solves the following constrained optimisation problem

$$\min_{h_u} \max_{1\le u\le U} \max_{\omega_p\in\Omega_p} \left\{ \left| \left|P_u(e^{j\omega_p})\right|^2 - |H_d(\omega_p)|^2 \right| + \frac{\alpha}{\pi}\int_{\Omega_s} \left|P_u(e^{j\omega})\right|^2 d\omega \right\} \tag{3.15}$$

subject to the following autocorrelation constraint

$$|R_{ac}(m)| = \left| \sum_{k=0}^{M-1} h_u(k)h_u(k-mC) \right| \le \epsilon_1 \tag{3.16}$$

where $m = 1, 2, \ldots$ and also the cross-correlation constraint

$$|R_{cc}(m)| = \left| \sum_{k=0}^{M-1} h_n(k)h_u(k-mC) \right| \le \epsilon_2 \tag{3.17}$$

for $n \neq u$, $n = 1, 2, \ldots, U$ and $m = 0, \pm 1, \pm 2, \ldots$, where $H_d(\omega)$ is the ideal frequency response function, α is the weighting parameter, Ω_p is the passband frequency, Ω_s is the stopband frequency, and C represents the number of samples per symbol interval, where C should be a positive number.

Remarks: In the first part of the objective function, all filters are shaped to a desired spectral shape, $H_d(\omega)$, by minimizing the magnitude error in the passband. $H_d(\omega)$ is the desired frequency response of an ideal non causal Nyquist pulse. The second part of the objective function is to minimize the stopband energy leakage by weighting the filters with α. Parameter α can be adjusted by the designer to achieve a trade-off between spectral shaping accuracy and minimizing the stopband energy leakage. A smaller value of α will give a better fitting pulse shape, while a larger value of α will minimize the stopband energy leakage. In constraints (3.16) and (3.17), ϵ_1 and ϵ_2 are set to positive values that are sufficiently small to minimize ISI and CCI respectively.

3.3.2 Problem Conversion

The constraints (3.16) and (3.17) in problem (PU) are non-convex and is difficult to solve using existing mathematical software such as MATLAB. After mathematical derivation as shown in Appendix 3.A, the problem (PU) is simplified and can be written as the optimisation problem (PUb).

Problem(PUb). Find h_u which solve the following optimisation problem

$$\min_{h_u} \max_{1 \leq u \leq U} \max_{\omega_p \in \Omega_p} \left\{ \left| \left| h_u^{\mathrm{T}} A(\omega) h_u \right| - |H_d(\omega_p)|^2 \right| + \frac{\alpha}{\pi} \int_{\Omega_s} A_s(\omega) d\omega \right\} \tag{3.18}$$

subject to

$$\left| h_u^{\mathrm{T}} A_m h_u \right| \leq \epsilon_1 \tag{3.19}$$

for $2 \leq u \leq U$ and $m = 1, 2, \ldots$ and

$$\left|h_n^{\mathrm{T}} G_m h_u\right| \leq \epsilon_2 \tag{3.20}$$

where $n \neq u$, $n = 1, 2, \ldots, U$, $u = 1, 2, \ldots, U$, $m = 0, \pm 1, \pm 2, \ldots, G_m = A_m$ for $m > 0$ and $G_m = A_m^{\mathrm{T}}$ for $m \leq 0$.

Remarks: Instead of solving problem (PUb) for all $P_u(e^{j\omega})$ simultaneously, the problem can be solved using the following method. First, the problem (PUb) is solved for $P_1(e^{j\omega})$ subject to autocorrelation constraint. Then, using $P_1(e^{j\omega})$, problem (PUb) for $P_2(e^{j\omega})$ is solved by subjecting it to both autocorrelation and cross-correlation constraints, in an iterative manner for $P_3(e^{j\omega})$, $P_4(e^{j\omega})$, etc.

3.3.3 Numerical Results

To design the digital waveforms, the number of digital waveforms in a set is equal to the number of users, U. In the following simulations, the number of users considered are $U = 2$ and $U = 4$. In this subsection, the designed pulses are presented according to $U = 4$. The desired pulse shape, $H_d(\omega)$, is chosen to be the spectral function of the impulse function of a SRRC pulse with $\beta = 0.2$ or a rolloff factor of 20%. The normalized magnitude spectrum response of $H_d(\omega)$ is shown in Fig. 3.3. Other design parameters are $C = 4$, $M = 48$, $\epsilon_1 = 0.001$, $\epsilon_2 = 0.001$, and $\alpha = 0.1$, where C is the number of samples per symbol interval.

The designed waveforms are summarized in Fig. 3.4, Fig. 3.5, and Fig. 3.6. Fig. 3.4 represents the normalized magnitude responses of the 4 digital waveforms, which can be observed that all 4 designed waveforms are close approximates of the desired waveform in Fig. 3.3. Shaping the filters to a desired shape is essential for better spectrum efficiency. Fig. 3.5 shows the corresponding impulse response for each waveform, where it can be observed that the waveforms have different peaks which can minimise the PAPR. It is illustrated in Fig. 3.6 that the power spectrum of the designed waveforms have low stopband leakage, which is desirable to reduce interferences from adjacent carriers or channels.

The effectiveness of the designed pulse shaping filter set in reducing the PAPR

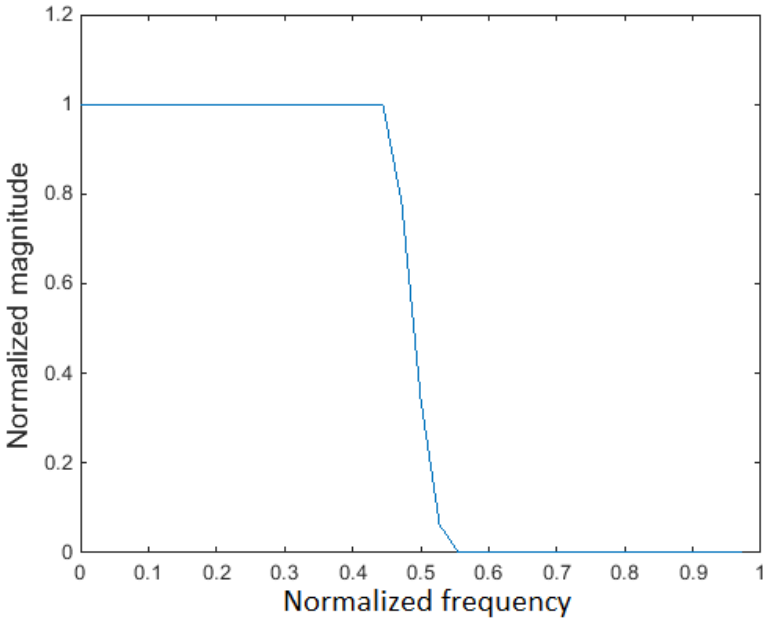

Figure 3.3: Frequency Response of Root Raised Cosine Pulse.

in MU-OFDM signals is evaluated at using $N = 128$ and $N = 256$ subcarriers, with filter roll-off factors $\beta = 10\%$ and $\beta = 20\%$, as illustrated in Fig. 3.7. The effectiveness of the designed waveforms in reducing the PAPR of the MU-OFDM signal is observed at $PAPR_0 = 10^{-4}$. For $N = 128$ subcarriers, the designed filters with roll-off $\beta = 10\%$ reduced the PAPR by about 1.3 dB, while the one with $\beta = 20\%$ reduced the PAPR by about 1.4 dB. For $N = 256$ subcarriers, the PAPR reduction obtained from using the designed filters are 1.5 dB and 1.7 dB for $\beta = 10\%$ and $\beta = 20\%$, respectively.

As the pulse shaping might result in interferences, the BER is evaluated at the receiver over a Rayleigh channel. The HIPERLAN/2 channel model is a standard which supports high speed wireless communications, and is used to simulate a practical environment [81]. The parameters and characteristics of the channel models are summarized in Table 3.1.

The BER of the MU-OFDM system with and without pulse shape filtering is shown in Fig. 3.8. At $P_b = 10^{-4}$, the conventional MU-OFDM requires an SNR of around 32 dB, while the MU-OFDM with the designed pulse shape requires only

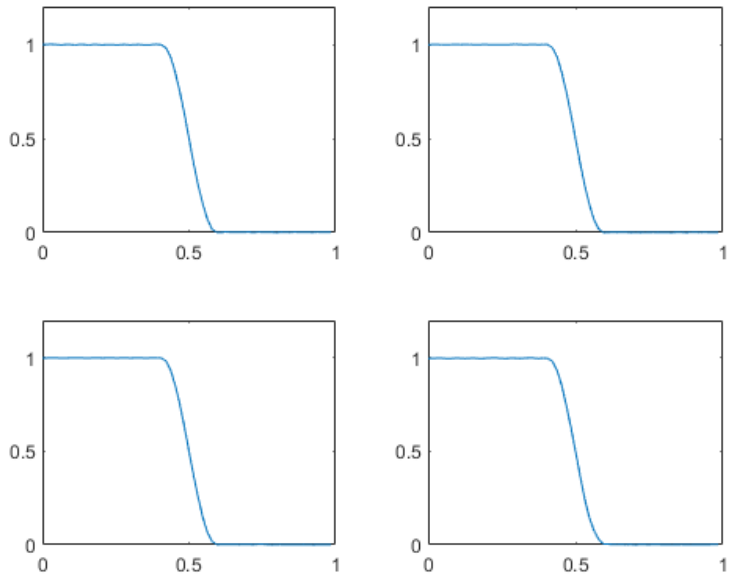

Figure 3.4: Normalized magnitude spectral responses of the designed 4 digital waveforms. The x-axis represents the normalised frequency, C, while the y-axis is the normalised magnitude.

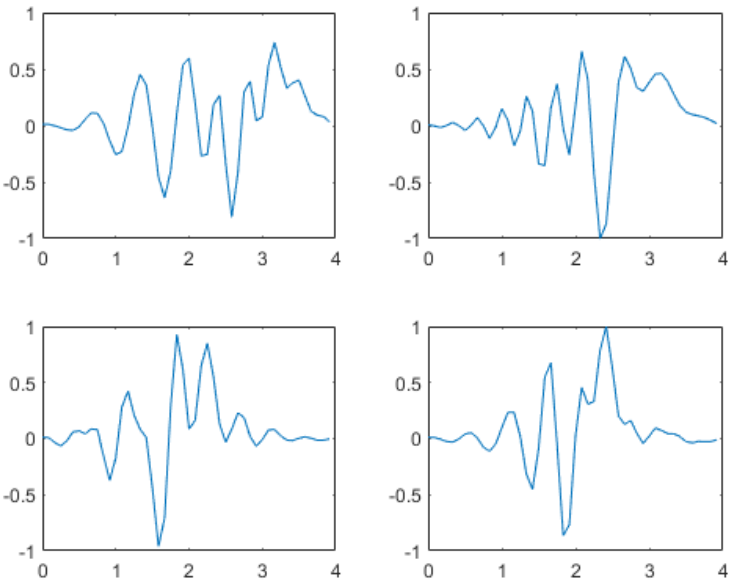

Figure 3.5: Impulse responses of the designed 4 digital waveforms. The x-axis represents the symbol duration of the filter, C, while the y-axis is the normalised amplitude.

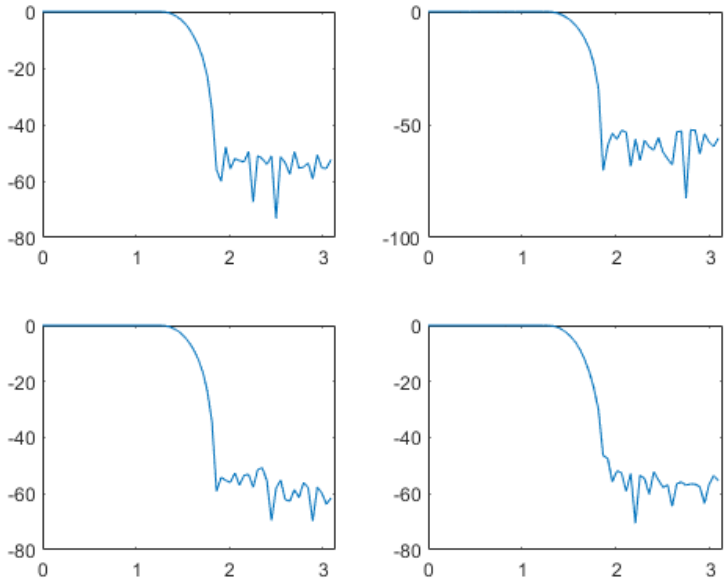

Figure 3.6: Power spectrum of the designed 4 digital waveforms. The x-axis represents the symbol duration of the filter, C, while the y-axis is the normalised power spectral density in dB.

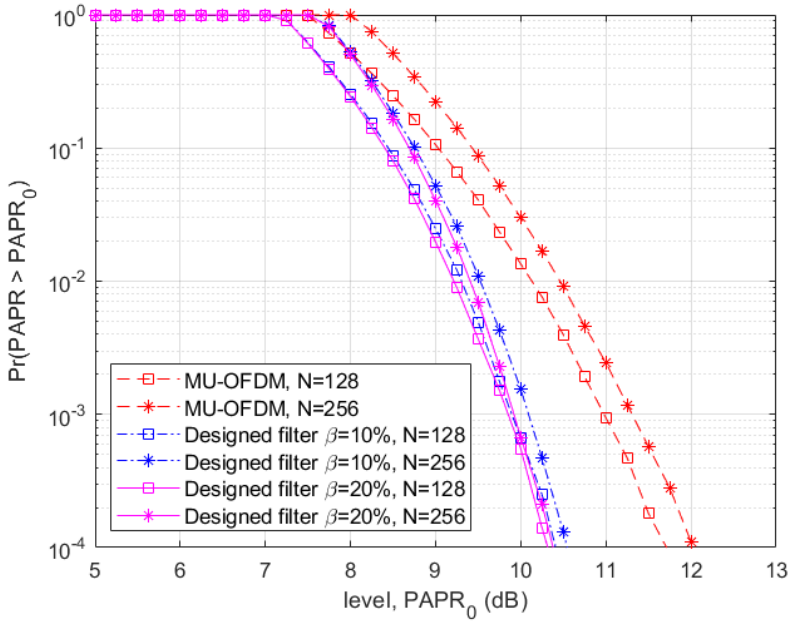

Figure 3.7: PAPR of MU-OFDM with designed pulse shaping filter set with U = 2 users.

Table 3.1: Channel models for HIPERLAN/2 in different indoor scenarios.

Name	RMS delay	Max delay	Characteristic	Environment
A	0.016T	0.122T	Rayleigh	Typical office
B	0.032T	0.228T	Rayleigh	Large open space or office
C	0.047T	0.328T	Rayleigh	Large open space
D	0.044T	0.328T	Rician	Large open space
E	0.078T	0.550T	Rayleigh	Large open space

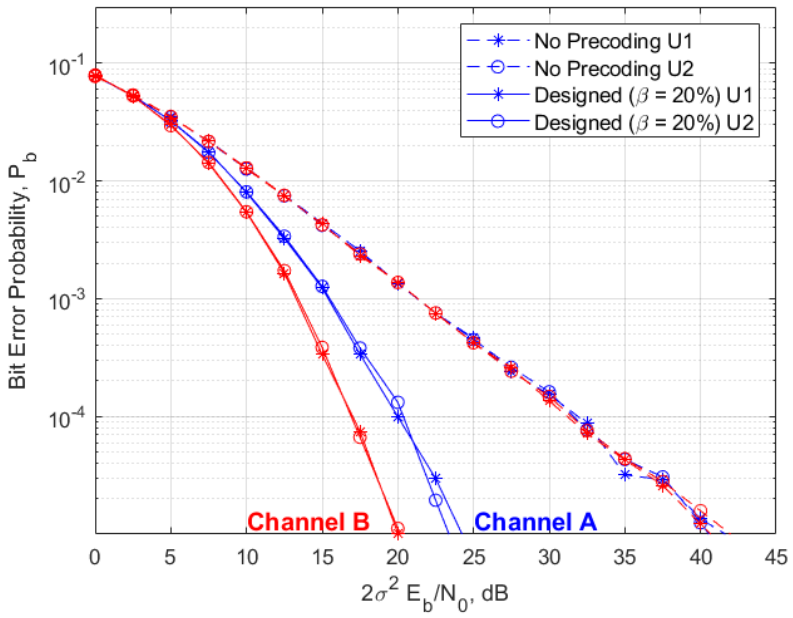

Figure 3.8: BER of MU-OFDM with designed pulse shaping filter set over HIPERLAN/2 channel.

20 dB and 17 dB SNR, respectively, when simulated over channel A and channel B. Transmitting the MU-OFDM signal with pulse shaping over channel B of the HIPERLAN/2 has a better BER than when it is transmitted over channel A, and this is due to the smaller coherence bandwidth of the channel B. It has been investigated that the roll-off factors of the pulse shaping filter, β, has minor affect towards the BER.

3.4 MU-MIMO-OFDM System

Generally, a multipath fading channel is detrimental to the overall wireless communication system performance as it causes ICI in the received signal. To combat the multipath fading channel, CP is usually added to the transmitted signal, or a more complex detector at the receiver is employed [82]. Implementing MIMO at the wireless communication system exploits the multipath fading channel by transmitting data to multiple users over different paths of the channel [83]. This is achievable via an array of antennas at the transmitter, and using beamforming, instead of viewing the effects of multipath fading channel as interferences, these signals can be added up constructively.

The MIMO can be implemented into MU-OFDM systems to increase the overall capacity of the system. In a MU-MIMO-OFDM system, multiple antennas are used to transmit data to multiple users [84]. However, a MU-MIMO-OFDM system also exhibits a high PAPR in the transmitted signal.

3.4.1 MU-MIMO-OFDM System Model

Fig. 3.9 illustrates the MU-MIMO-OFDM system model with pulse shaping technique with K subcarriers and U users utilizing the system, where the transmitter and receivers have N_T and N_R antennas, respectively. A fixed subcarrier allocation is assumed, where each user u is allotted $K_u = \frac{K}{U}$ subcarriers. Data from each user is transmitted over an antenna, Tx_u, hence each antenna will transmit a total of K_u subcarriers.

The baseband modulated input data symbol $\mathbf{X}^u = [X_0^u, X_1^u, \ldots, X_{K_u-1}^u]^{\mathrm{T}}$ is multiplied with a $L_u \times K_u$ pulse shaping matrix, $\mathbf{P}^u$, where we denote $(\cdot)^{\mathrm{T}}$ as the matrix transpose, and $L_u = \frac{L}{U}$ as the number of subcarriers per user. Parameter $L = K + K_s$, is the total number of subcarriers, K_s represents additional subcarriers as overhead with $0 \leq K_s < K$, given as $K_s = \beta K$, and β denotes the portion of excess bandwidth.

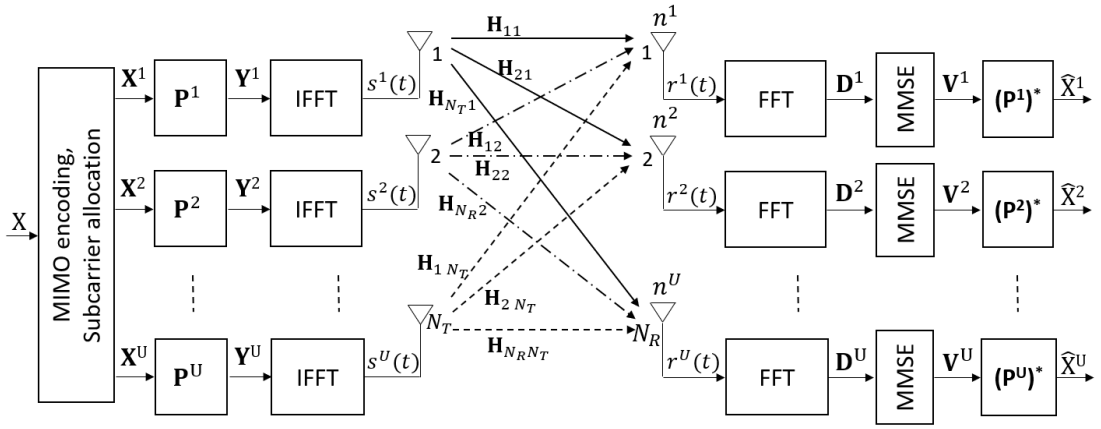

Figure 3.9: MU-MIMO-OFDM system model.

After pulse shaping is implemented, the output of the processed data can be expressed as

$$\mathbf{Y}^u = \mathbf{P}^u \mathbf{X}^u = [Y_0^u, Y_1^u, \ldots, Y_{L_u-1}^u]^{\mathrm{T}} \tag{3.21}$$

where

$$Y_i^u = \sum_{k=0}^{K_u-1} P_{i,k}^u X_k^u, \qquad i = 0, 1, \ldots, L_u - 1. \tag{3.22}$$

Eq. (3.22) is then processed by the IFFT modulation. The baseband equivalent of the discrete MU-MIMO-OFDM transmitted signal is given as

$$s[n] = \sum_{u=1}^{U} s^u[n], \tag{3.23}$$

where $0 \leq t \leq T$, and $s^u[n]$ represents the transmitted signal of uth user and given by

$$s^u[n] = \sum_{i=0}^{L_u-1} Y_i^u e^{\frac{j2\pi\iota n}{\mathcal{L}K}}, \tag{3.24}$$

where $\iota = (u-1)L_u + i$, with $i = \{0, 1, \ldots, L_u - 1\}$.

The MU-MIMO-OFDM signal is transmitted over a multipath fading channel, where the fading is set to be frequency selective fading. Consider that the

guard interval of the MU-MIMO-OFDM signal is greater than the maximum delay spread of the channel and the channel state information (CSI) is known at the receiver through pilot symbols. It is also assumed that the subcarrier intended for each user is known at the receiver from the subcarrier allocation. The demodulated received signal at the receive antenna of the u user can be written in matrix form as

$$\mathbf{D}^u = \mathbf{H}^u\mathbf{Y} + \mathbf{n}_u, \tag{3.25}$$

where $\mathbf{D}^u = [D_0^u, D_1^u, \ldots, D_{L-1}^u]^{\mathrm{T}}$ and $\mathbf{Y} = [\mathbf{Y}^1, \mathbf{Y}^2, \ldots, \mathbf{Y}^{N_T}]^{\mathrm{T}}$ are column vectors with length L given in (3.21), and $\mathbf{n}^u = [n_0^u, n_1^u, \ldots, n_{L-1}^u]^{\mathrm{T}}$ represents the additive white Gaussian noise (AWGN). $\mathbf{H}^u$ is the channel response matrix of the transmitter-receiver link, expressed as

$$\mathbf{H}^u = \mathrm{diag}\{\mathbf{H}_1^u, \mathbf{H}_2^u, \ldots, \mathbf{H}_{N_T}^u\}, \tag{3.26}$$

where $\mathbf{H}_q^u = \mathrm{diag}\{H_0, H_1, \ldots, H_{L_u-1}\}$ are $L_u \times L_u$ diagonal matrices representing each subcarrier channel coefficients of the channel path taken from qth transmit antenna to uth user's receive antenna.

As the transmitted signal may be corrupted by channel fading and noise, the received signal needs to be compensated by a weighting matrix $\mathbf{G}$ in order to recover the intended data. Consider that the minimum mean-squared error (MMSE) detector is used, Eq. (3.25) is weighted using the following parameter

$$\mathbf{G}^u = \mathbf{H}^{u*}(\mathbf{H}^u\mathbf{H}^{u*} + N_0\mathbf{I})^{-1}, \tag{3.27}$$

where $N_0 = \sigma_n^2/\sigma_s^2$, σ_n is the noise variance, and σ_s is the signal variance. Then, the transmitted data for uth user can be recovered using

$$\hat{\mathbf{X}}^u = (\mathbf{P}^u)^*\mathbf{G}^u\mathbf{D}^u. \tag{3.28}$$

3.4.2 PAPR of MU-MIMO-OFDM Signal

The PAPR of the MU-MIMO-OFDM transmit signal is defined as

$$PAPR_q = \frac{\max\limits_{0\leq t<T} |s_q[n]|^2}{E\{|s_q[n]|^2\}}, \tag{3.29}$$

where $q = 1, 2, \ldots, N_T$ represents the qth transmit antenna and $E\{\cdot\}$ denotes expectation. In the case of using multiple antennas (MIMO), the PAPR of the transmitted MU-MIMO-OFDM signal is expressed as the maximum PAPR among N_T transmit antennas, written as [85]

$$PAPR_s = \max_{q=1,2,\ldots,N_T} \{PAPR_q\}. \tag{3.30}$$

The PAPR of the MU-MIMO-OFDM signal with pulse shaping technique (3.30) will be evaluated using the CCDF [58], which can be written as

$$CCDF_{PAPR_s}(PAPR_0) \triangleq P_r\Big\{PAPR_s \geq PAPR_0\Big\}, \tag{3.31}$$

where $PAPR_0$ is a given level of signal power.

3.4.3 Numerical Results

Consider that a MU-MIMO-OFDM transmitter with $N = 256$ for $U = 2$ and $U = 4$. The rolloff factor is set to $\beta = 10\%$ and $\beta = 20\%$. In order to show the PAPR reduction capability of pulse shaping using the proposed pulse design technique, the PAPR of a precoded MU-MIMO-OFDM signal is compared to a conventional MU-MIMO-OFDM signal.

Fig. 3.10 shows that the proposed filter design has reduced the PAPR of a MU-MIMO-OFDM signal by about 1.5 db when $\beta = 10\%$ and 2 dB when $\beta = 20\%$, at Pr(PAPR) $>$ PAPR$_0$ $= 10^{-2}$ for 2 users. When $U = 4$, the PAPR level is slightly lower when compared with $U = 2$ as the number of subcarriers is less, i.e. the number of subcarriers used are $N_u = 64$ and $N_u = 128$ when $U = 4$ and

$U = 2$ respectively.

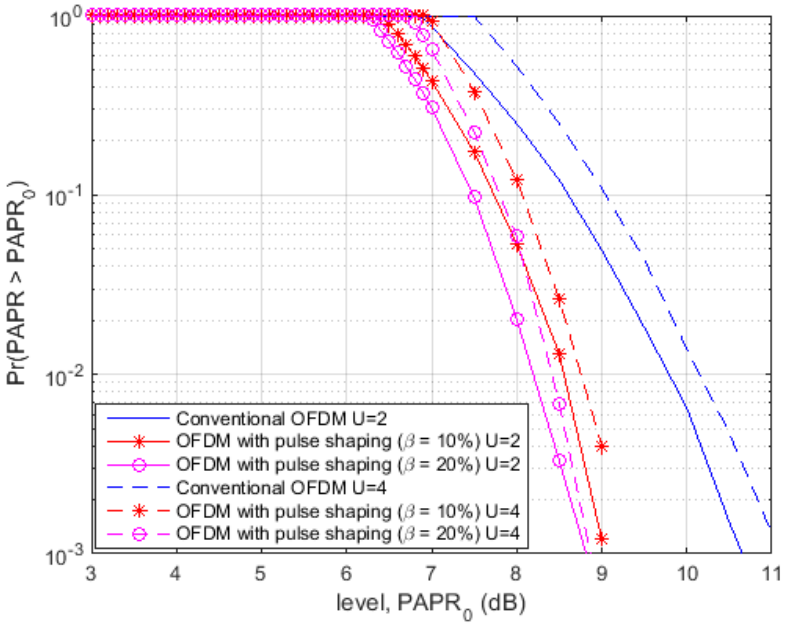

Figure 3.10: PAPR of MU-MIMO-OFDM signal with pulse shaping.

In order to see the effectiveness of the proposed filter design at the receiver over multipath fading channels, HIPERLAN/2 model is used. The following simulations are performed using Channel A and Channel B for $U = 2$ and $U = 4$. Simulation result shown in Fig. 3.11 indicate that for a BER of 10^{-4}, the proposed filter design requires about 18 dB less SNR for Channel A, and 23 dB less SNR for Channel B, when compared to a conventional OFDM without pulse shaping. From Fig. 3.11, it can be observed that the BER for $\beta = 10\%$ and $\beta = 20\%$ has marginal differences. Analysing the results from both Fig. 3.10 and Fig. 3.11, utilising more users ($U = 4$) has a poorer PAPR and BER performance when compared with less users ($U = 2$).

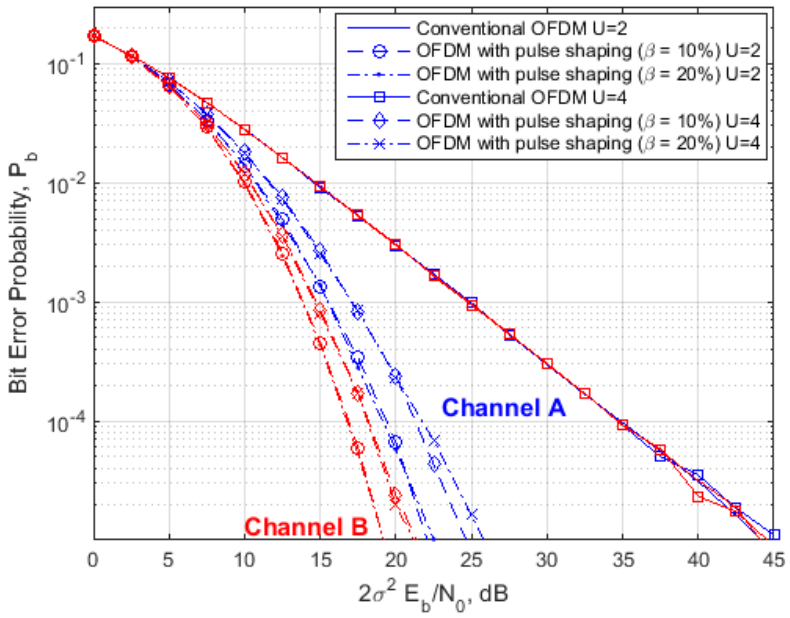

Figure 3.11: BER performance of MU-MIMO-OFDM signals with pulse shaping over multipath fading channel.

3.5 Concluding Remarks

In this chapter, a set of causal pulse shaping filters have been designed using the min-max optimisation. To minimise multiuser interference, the waveform set design problem was formulated with autocorrelation and cross-correlation constraints. The design problem was then simplified and solved iteratively. The numerical results demonstrated that the designed set of pulse shaping filters is effective in reducing the PAPR of the transmitted MU-OFDM signal by about 1.5 dB while improving the BER performance, when compared with the conventional MU-OFDM system. When the designed filters are implemented in the MU-MIMO-OFDM system, the PAPR of the transmitted signal is reduced by about 1.4 dB and has improved the BER performance as well.

3.A Appendix: Problem Simplification

Considering the simplification of the problem (PU), we first look at the objective function.

We first simplify the first part of the objective function. It is assumed that the receiver uses the matched filter and the channel is a flat fading channel. Hence, the magnitude of the overall transfer function can be expressed as

$$|P_u(e^{j\omega})|^2 = h_u^{\mathrm{T}} A(\omega) h_u, \tag{3.32}$$

where $h_u = [h_u(0), h_u(1), \ldots, h_u(M-1)]$ and $A(\omega)$ is an $M \times M$ constant matrix generated with

$$a(m,n) = \cos(\omega_p(m-n)). \tag{3.33}$$

The first part of the objective function, or the passband magnitude error, can be expressed as

$$\xi_p = \left| \left| h_u^{\mathrm{T}} A(\omega) h_u \right| - \left| H_d(\omega_p) \right|^2 \right| \ , \omega_p \in \Omega_p. \tag{3.34}$$

The stopband energy error, which is the second part of the objective function, can be expressed as

$$\xi_s = h_u^{\mathrm{T}} A_s(\omega) h_u, \tag{3.35}$$

where A_s is a matrix with $N \times N$ dimensions defined by

$$A_s = \frac{1}{\pi} \int_{\Omega_s} A(\omega) d\omega. \tag{3.36}$$

To simplify the correlation constraints in (3.16) and (3.17), the following matrix is defined:

$$A_m = \begin{bmatrix} \mathbf{0}_{m1} & \mathbf{0}_m \\ \mathbf{I}_m & \mathbf{0}_{m1}^{\mathrm{T}} \end{bmatrix} \tag{3.37}$$

where $\mathbf{I}_m$ is an $(N - mC) \times (N - mC)$ identity matrix, $\mathbf{0}_m$ is an $(mC) \times (mC)$ zero matrix, and $\mathbf{0}_{m1}$ represents an $(mC) \times (N - mC)$ zero matrix. The autocorrelation constraint (3.16) can be expressed as

$$|R_{ac}(m)| = |h_u^{\mathrm{T}} A_m h_u| \leq \epsilon_1, \tag{3.38}$$

and the cross-correlation constraint (3.17) is written as

$$|R_{cc}(m)| = |h_n^{\mathrm{T}} G_m h_u| \leq \epsilon_2, \tag{3.39}$$

where $G_m = A_m$ for $m > 0$ and $G_m = A_m^{\mathrm{T}}$ for $m \leq 0$.

Chapter 4

Filter Design for GFDM Systems

In Chapter 3, the pulse shaping technique has been applied in the MU-OFDM system and MU-MIMO-OFDM system to reduce the PAPR. The 5G network is envisaged to be applied in a wide variety of applications, and hence the more diverse requirements and specifications as compared with the fourth generation (4G) network [5], [9], [86]. Some of the requirements include low energy consumption, low latency, and low OOB radiation. Current OFDM systems will not be suitable for implementation in the 5G network due to several drawbacks, such as strict synchronisation and a high OOB radiation. The GFDM system has been considered as one of the potential candidates for the modulation system in 5G. The flexibility of the GFDM system allows the system to adjust the system parameters, such as the subcarriers, subsymbols, and pulse shaping filter, in order to meet different types of requirements. Properly selecting the pulse shaping filter in GFDM allows the GFDM system to have better system performances such as lower PAPR and lower OOB radiation.

In this chapter, causal pulse shaping filter is formulated and designed for the GFDM system. In order to minimise the OOB radiation of the GFDM signal, the designed filter needs to have a low stopband energy. The rest of this chapter is structured as follows: Section 4.1 presents a low complexity transmitter model.

The OOB radiation of the GFDM signal is discussed in Section 4.2. Section 4.3 presents the design of a causal pulse shaping filter that minimises the PAPR and OOB radiation of the GFDM signal. The effectiveness of the designed filter in reducing the PAPR and OOB radiation is analysed in Section 4.4. Finally, concluding remarks are drawn in Section 4.5.

4.1 Low Complexity GFDM Transmitter

It has been shown in [87] that the GFDM equation in (2.15) requires high complexity. Eq (2.15) can be rewritten in such a way that the GFDM processing is done in the frequency domain with lower complexity. Let $\mathbf{x} = (\mathbf{x}_0^{\mathrm{T}}, \mathbf{x}_1^{\mathrm{T}}, \ldots, \mathbf{x}_{K-1}^{\mathrm{T}})^{\mathrm{T}}$ be a concatenation of K sequences $\mathbf{x}_k = (x_0^k, x_1^k, \ldots, x_{M-1}^K)^{\mathrm{T}}$ with M elements each. Therein, d_m^k corresponds to the data symbol transmitted in the kth subcarrier and mth subsymbol. The low complexity GFDM transmitted signal is given as [88]

$$\mathbf{s} = \mathbf{W}_N^H \sum_{k=0}^{K-1} \mathbf{\Psi}_k \mathbf{P} \mathbf{\Lambda} \mathbf{W}_M \mathbf{x}_k, \tag{4.1}$$

where $\mathbf{W}_M$ is an M-point discrete Fourier transform (DFT) matrix and $\mathbf{\Lambda} = \{\mathbf{I}_M \mathbf{I}_M \ldots\}$ is a concatenation of V identity matrices. The parameter V is the upsampling factor of the pulse shaping filter and $V = 2$ is sufficient for most pulse shaping filters [61]. The filter matrix $\mathbf{P} = \mathrm{diag}\{P_0, P_1, \ldots, P_{VM-1}\}$ is a diagonal matrix with entries from the frequency response coefficients of the prototype filter. A permutation matrix $\mathbf{\Psi}_k$ is used to up-convert each subcarrier to their respective frequencies according to the following:

$$\begin{aligned}
\mathbf{\Psi}_0 &= \begin{pmatrix} \mathbf{I}_{VM/2} & \mathbf{0}_{VM/2} & \dots & \mathbf{0}_{VM/2} & \mathbf{0}_{VM/2} \\ \mathbf{0}_{VM/2} & \mathbf{0}_{VM/2} & \dots & \mathbf{0}_{VM/2} & \mathbf{I}_{VM/2} \end{pmatrix}^{\mathrm{T}} \\
\mathbf{\Psi}_1 &= \begin{pmatrix} \mathbf{0}_{VM/2} & \mathbf{I}_{VM/2} & \dots & \mathbf{0}_{VM/2} & \mathbf{0}_{VM/2} \\ \mathbf{I}_{VM/2} & \mathbf{0}_{VM/2} & \dots & \mathbf{0}_{VM/2} & \mathbf{0}_{VM/2} \end{pmatrix}^{\mathrm{T}} \\
&\vdots \\
\mathbf{\Psi}_{K-1} &= \begin{pmatrix} \mathbf{0}_{VM/2} & \mathbf{0}_{VM/2} & \dots & \mathbf{0}_{VM/2} & \mathbf{I}_{VM/2} \\ \mathbf{0}_{VM/2} & \mathbf{0}_{VM/2} & \dots & \mathbf{I}_{VM/2} & \mathbf{0}_{VM/2} \end{pmatrix}^{\mathrm{T}}.
\end{aligned} \tag{4.2}$$

The permutation matrix $\mathbf{\Psi}_k$ allows the frequency response of the pulse shaping filter to be centered at their assigned frequencies, as shown in Fig. 4.1. It can also be observed that each pulse shaping filter occupies two subcarrier spaces due to $\mathbf{\Lambda}$ when $V = 2$.

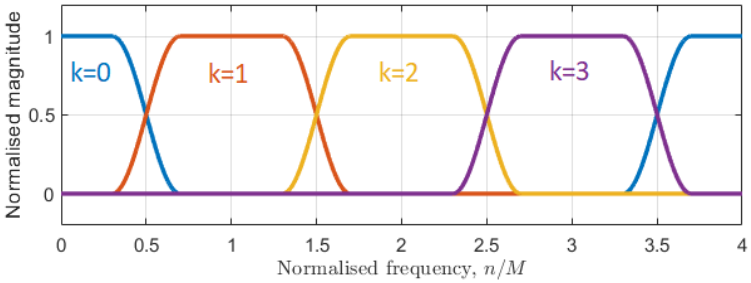

Figure 4.1: The arrangement of the frequency response of the pulse shaping filters in the GFDM system with $K = 4$ subcarriers and filter roll-off $\beta = 0.4$.

The computational cost of the low complexity GFDM transmitter (4.1) considering only complex multiplications is computed as [88]

$$C_{GFDMtx,low} = MN \log_2 N + (K + N)M \log_2 M + KVM. \tag{4.3}$$

This has greatly reduced the computational complexity of the GFDM transmitter, when compared with the conventional one that has a complexity of $C_{GFDMtx,conv} = NKM^2$. Therefore, the low complexity GFDM transmitter de-

scribed in (4.1) is used throughout this thesis.

4.2 Out-of-band Radiation of GFDM System

In the 5G system, a massive number of devices consisting mainly of MTC are expected to connect to a single cell tower [9]. Spectrum sharing mechanisms will need to be deployed to accommodate the massive traffic under limited frequency resource, with consideration that the transmitted signals do not interfere with neighbouring channels [89]. Techniques such as adding guard bands, windowing, and pulse shaping are used to reduce the interference by suppressing the OOB radiation [86], [90]. However, these techniques often come with additional bandwidth usage or extra computational complexity. Generally, the GFDM system offers a much lower OOB radiation as compared to the OFDM system through a proper selection of pulse shaping filters. To measure the OOB radiation of the GFDM system, the power spectral density (PSD) is analysed.

The PSD of a baseband signal is calculated according to [91]

$$PSD(f) = \lim_{T\to\infty} \frac{1}{T} E\left\{ \left| s(t) e^{-j2\pi ft} \right| \right\}, \tag{4.4}$$

where $s(t)$ is the transmit signal that is fed to a D/A converter and truncated to the interval $(-T/2, T/2)$.

In the GFDM case, the PSD of $s(t)$ is measured across v number of GFDM blocks, each ranges from $-\frac{T}{2MT_s}$ to $+\frac{T}{2MT_s}$. The analog baseband signal is obtained as

$$s(t) = \sum_{v,m,k} X_{v,m,k} p_{0,m}(t - vMT_s) e^{-j2\pi \frac{k}{T_s} t}, \tag{4.5}$$

with the frequency domain representation written as

$$S(f) = \sum_{v,m,k} X_{v,m,k} P_m \left(f - \frac{k}{T_s} e^{-j2\pi vMT_s f} \right), \tag{4.6}$$

where $P_m(f)$ is the Fourier transform of $p_{0,m}$. Assuming that the data symbols are zero-mean and independent and identically-distributed (i.i.d.), the PSD of a GFDM system can be obtained by inserting (4.6) into (4.4), which can be expressed as [92]

$$PSD_{GFDM}(f) = \frac{1}{MT_s}\sum_{k,m}\left|P_m\left(f-\frac{k}{T_s}\right)\right|^2. \tag{4.7}$$

The OOB leakage can be analysed by using the ratio of the average energy that is emitted into neighbouring frequency bands, $PSD_{OOB,av}$, and the average energy within the allocated bandwidth, $PSD_{B,av}$. It is defined as [92]

$$\begin{aligned}\mathcal{O} &= \frac{|\mathcal{B}|}{|\mathcal{OOB}|}\cdot\frac{\int_{f\in\mathcal{OOB}}PSD(f)df}{\int_{f\in\mathcal{B}}PSD(f)df}\\ &= \frac{PSD_{OOB,av}}{PSD_{B,av}},\end{aligned} \tag{4.8}$$

where $|\mathcal{B}|$ and $|\mathcal{OOB}|$ are the cardinality of the in-band frequencies and the out-of-band frequencies, respectively. The out-of-band average energy is obtained from $PSD_{OOB,av} = \frac{\int_{f\in\mathcal{OOB}}PSD(f)df}{|\mathcal{OOB}|}$, while the in-band average energy is obtained from $PSD_{B,av} = \frac{\int_{f\in\mathcal{B}}PSD(f)df}{|\mathcal{B}|}$.

4.3 Optimum Filter Design for GFDM

It can be seen from (4.8) that the PSD of the GFDM system is affected by the pulse shaping filter $P(f)$. Minimising the stopband leakage of the pulse shaping filter is necessary in order to suppress the OOB radiation. It is also shown in [77], [93] that filters with low stopband energy has a better PAPR performance. By considering these factors, formulating filter problem using computationally efficient optimisation approach will be able to minimise the OOB radiation and the PAPR of the GFDM transmitted signal.

4.3.1 Problem Formulation

The frequency response of an R-tap FIR pulse shaping filter can be written as

$$P(e^{j\omega}) = \sum_{r=0}^{R-1} h_r e^{-j\omega r} = \mathbf{h}^{\mathrm{T}}\mathbf{e}(\omega), \tag{4.9}$$

given that $\mathbf{h} = [h_0, h_1, ..., h_{(R-1)}]^{\mathrm{T}}$ are the impulse response coefficients of the designed filter, $\mathbf{e}(\omega) = [1, e^{-j\omega}, ..., e^{-j\omega(R-1)}]^{\mathrm{T}}$, and $\omega = 2\pi f$, where f is the linear frequency in Hz.

The objective of the pulse shaping design problem is to minimise the weighted mean squared error between the desired ideal filter $P_d(\omega)$ and the designed pulse shaping filter $P(e^{j\omega})$ over the stopband region. Mathematically, it can be formulated as

$$\min_{\mathbf{h}} \frac{1}{\pi} \int_{\Omega_s} \lambda(\omega)|P(e^{j\omega}) - P_d(\omega)|^2 d\omega, \tag{4.10}$$

subject to

$$|P(e^{j\omega}) - P_d(\omega)| \leq \sigma_p, \qquad \omega \in \Omega_p, \tag{4.11}$$

where $\lambda(\omega)$ is a positive weighting function, $P_d(\omega)$ is the frequency response of the desired filter, Ω_s and Ω_p are the set of stopband and passband frequencies, respectively, and σ_p is the error tolerance in the passband. Note that $\lambda(\omega)$ is defined by the designer. In view of (4.10) and (4.11), the optimisation problem can be reformulated and solved using the quadratic programming (QP) approach.

4.3.2 Problem Simplification

The objective function (4.10) can be simplified as

$$\min_{\mathbf{a}} \left\{ \frac{1}{2}\mathbf{a}^{\mathrm{T}}\xi\mathbf{a} - \nu^{\mathrm{T}}\mathbf{a} \right\}, \tag{4.12}$$

where

$$\xi = \frac{2}{\pi} \int_{\Omega_s} \lambda(\omega)\mathbf{e}(\omega)\mathbf{e}^{\mathrm{H}}(\omega)d\omega,$$

$$\nu = \frac{2}{\pi} \int_{\Omega_s} \lambda(\omega)\Re\{\mathbf{e}(\omega)P_d(\omega)\}d\omega.$$

The function $P(e^{j\omega})$ in constraint (4.11) is complex and thus non-linear. It can be seen that the constraint should be linearised so that efficient optimisation algorithm and computational software can be used to solve the pulse shaping filter design problem formulated in (4.10) and (4.11).

Mathematical manipulation shown in Appendix 4.A is performed to linearise the constraint. Hence, instead of the constraints in (4.11), the following constraints over the discrete sets $\{\omega_l\}_{l=1}^{L}$ and $\{\theta_i\}_{i-1}^{2q}$ should be considered

$$B_l\mathbf{h} \leq c_l \tag{4.13}$$

where, for each l, B_l is a $2q$ by R matrix with $b^{\mathrm{T}}(\omega_l, \beta_i) = \cos(\omega_l r - \theta_i)$ as its ith row, c_l a $2q$-dimensional vector with all its entries $c_l = \frac{\sigma_p}{\sec(\pi/(2q))} + P_d(\omega_l)\cos(\theta_i)$.

Fig. 4.2 illustrates an exemplary designed FIR filter using the approach outlined in (4.12) and (4.22). The desired pulse $P_d(\omega)$ is chosen to be the RC pulse [94] with a roll-off factor of $\beta = 0.2$. The filter is designed using an FIR filter order $R = 64$, stopband weightage $\lambda(\omega) = 64$, and the passband tolerance $\sigma_p = 0.0001$. It can be seen that the frequency response of the designed filter almost resembles the RC pulse. In Fig. 4.3, the frequency response of using different passband tolerance levels is illustrated. A lower tolerance will produce a pulse shaping filter with larger ripples in the passband.

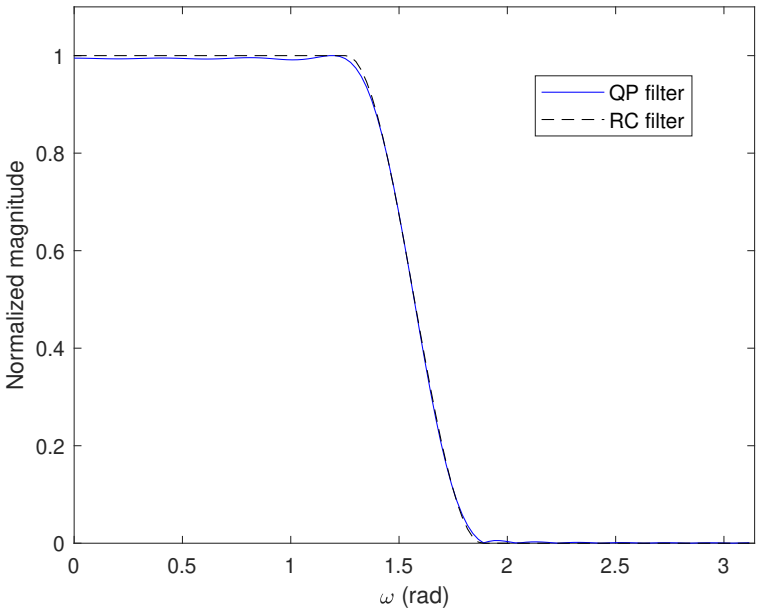

Figure 4.2: Frequency response of the designed QP filter and desired RC filter.

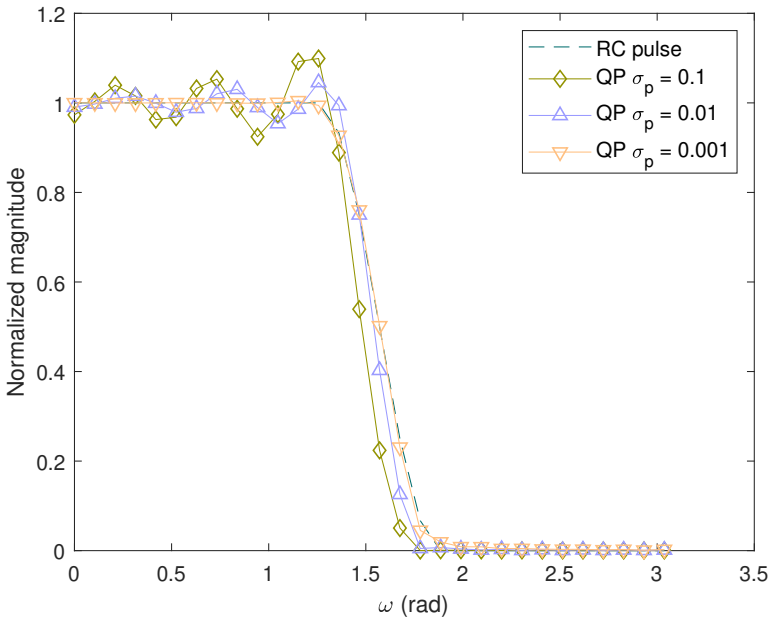

Figure 4.3: Frequency response of the designed filter at different passband tolerances, σ_p.

4.4 Numerical Results

To evaluate the effectiveness of the designed FIR filter in GFDM systems, the PAPR and OOB radiation performance is analysed at the transmitter. The performance of the designed FIR filter is analysed by comparing between a GFDM system using the designed pulse as the pulse shaping filter with roll-off $\beta = 0.2$ and a GFDM system using an RC filter with the same roll-off factor. The PAPR of an OFDM system and a single carrier frequency domain equalization (SC-FDE) system given in [61] is also included in the comparison. The number of subcarriers and subsymbols in the GFDM system is $K = 4$ and $M = 64$ respectively, hence $N = 256$. For a fair comparison, the total number of transmitted data symbols is fixed at N, ie. the number of transmitted data symbols is $K = N$ and $M = 1$ for an OFDM system, while for an SC-FDE system $K = 1$ and $M = N$.

4.4.1 PAPR of the GFDM Transmit Signal

Numerical result illustrated in Fig. 4.4 shows that the GFDM system using the designed pulse as the pulse shaping filter has a better PAPR performance, outperforming a GFDM system using an RC filter by about 0.5 dB. Further simulations were conducted to analyse the PAPR performance of GFDM systems using the designed FIR filter by varying the roll-off factor, with $\beta \in \{0.1, 0.25, 0.5\}$. Figure 4.5 shows that using the designed filter has a better PAPR performance for all simulated β. The performance of the proposed filter is also analysed for different values of subcarriers K and subsymbols M. For a same total number of data symbols N, the PAPR performance depicted in Fig. 4.6 shows that the proposed filter performs better in reducing the PAPR at higher subcarrier numbers.

The CCDF results given above shows that the GFDM system has a lower PAPR as compared with the OFDM system, consistent with what has been illustrated in [61]. However, in contrast with [61], reference [62] shows that the GFDM signals with higher number of data symbols have a higher PAPR than the

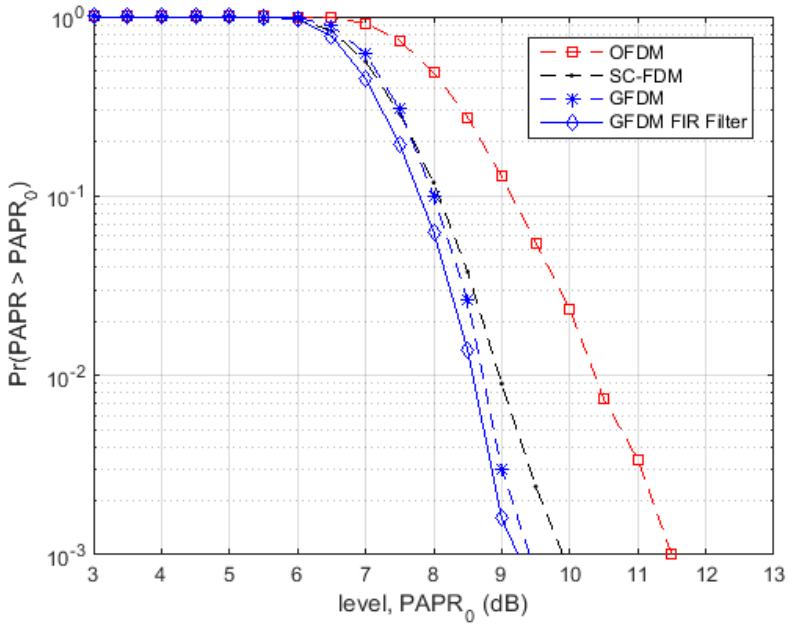

Figure 4.4: CCDF of the PAPR of GFDM signal using RC pulse and using the designed FIR filter, with $N = 256$, $\beta = 0.2$.

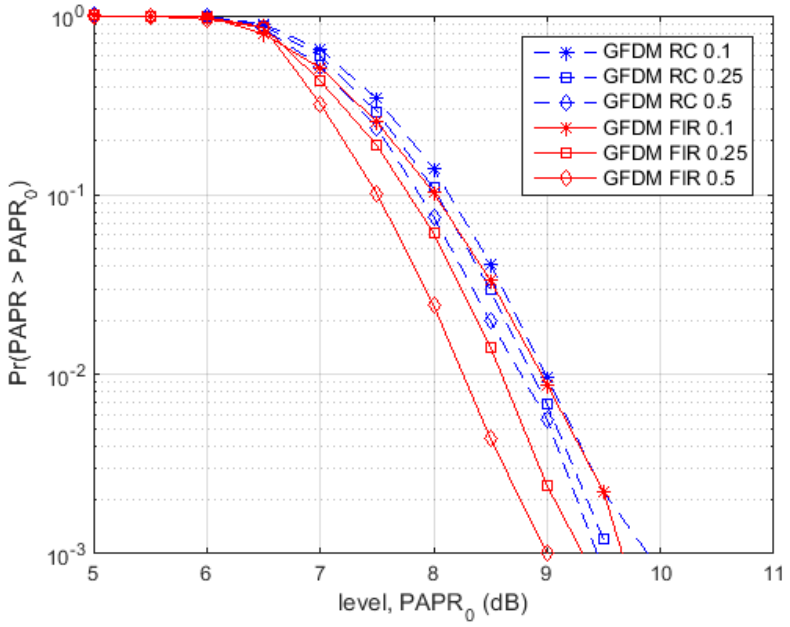

Figure 4.5: CCDF of the PAPR of the GFDM signal with different roll-off factors $\beta = \{0.1, 0.25, 0.5\}$, and $M = 64$ and $K = 4$.

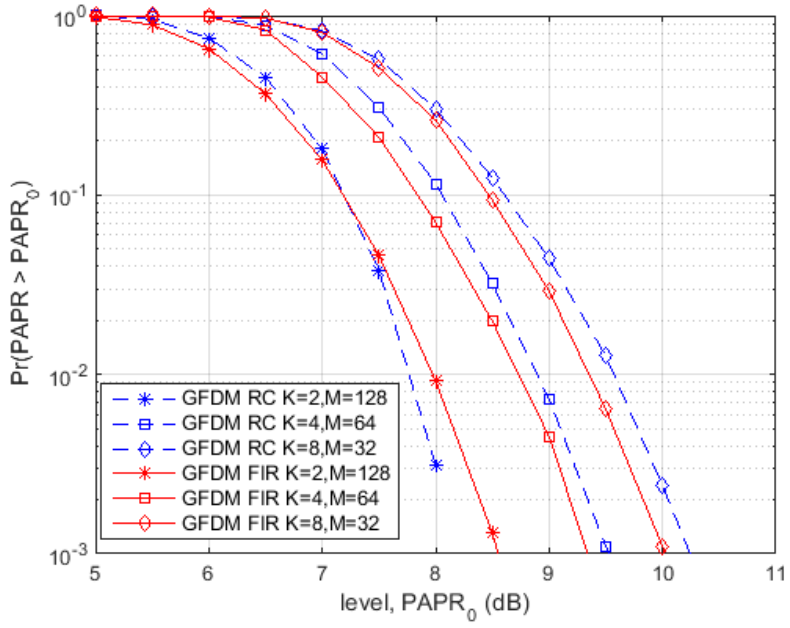

Figure 4.6: CCDF of the PAPR of GFDM signal with different subsymbols M and subcarriers K, for a total $N = 256$ and $\beta = 0.2$.

OFDM signal. The CCDF of the GFDM signal has also been derived in [75] to indicate that the GFDM signal will always have a higher PAPR than the OFDM signal when compared using the same number of data symbols.

In practical applications, the number of data symbols within a data block is usually high in order to increase the spectral efficiency. Hence, it is essential to consider the performance of the designed pulse shaping filter in a high data symbols setting. It is shown in Fig. 4.7 that the GFDM signals have a higher PAPR than the OFDM signal. It can also be seen that the GFDM signal with the designed pulse shaping filter has a lower PAPR than the one with ideal RC filter, where the PAPR is close to that of the OFDM signal.

4.4.2 PSD of the GFDM Transmit Signal

To analyse the PSD, a guard symbol is inserted for GFDM systems to allow for smooth transition between GFDM blocks, which is performed by setting the first subsymbol in each subcarrier to zero, $d_{k,0} = 0$ [92]. Fig. 4.8 illustrates the PSD

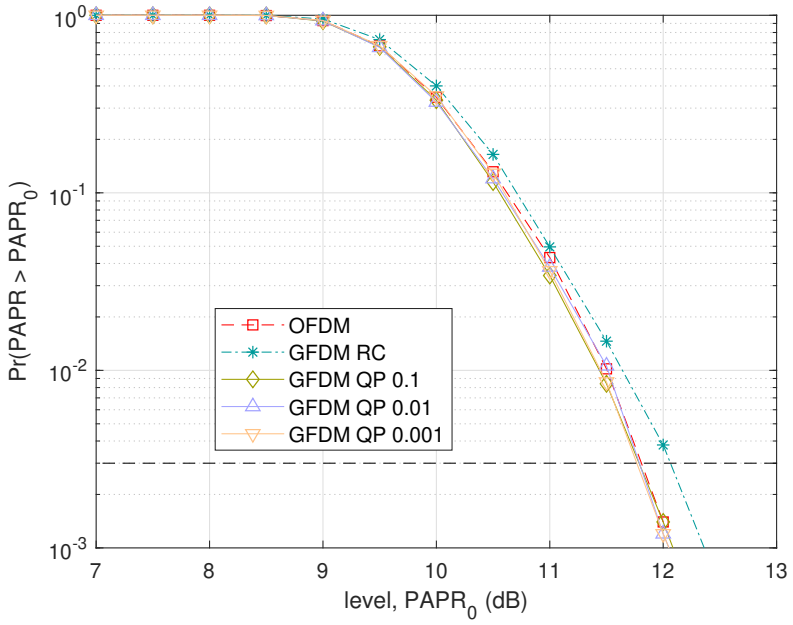

Figure 4.7: CCDF of the PAPR of GFDM signals with $K = 128$, $M = 15$, and $\beta = 0.2$.

for OFDM and GFDM using different pulse shaping filters. Using (4.8), it can be shown that by using guard symbol insertion, the GFDM system can achieve very low OOB radiation as compared to OOB radiation of the OFDM system. The designed filter shows better performance for $\sigma_p = 0.01$ and $\sigma_p = 0.001$. In fact, the designed filter is able to suppress the OOB to approximately -82.95 dB, which is significantly better than RC. The PSD performance analysis with different roll-off factor β are as illustrated in Fig. 4.9 where the higher roll-off factors producing lower OOB radiation due to the smoother transition of the filter in frequency domain.

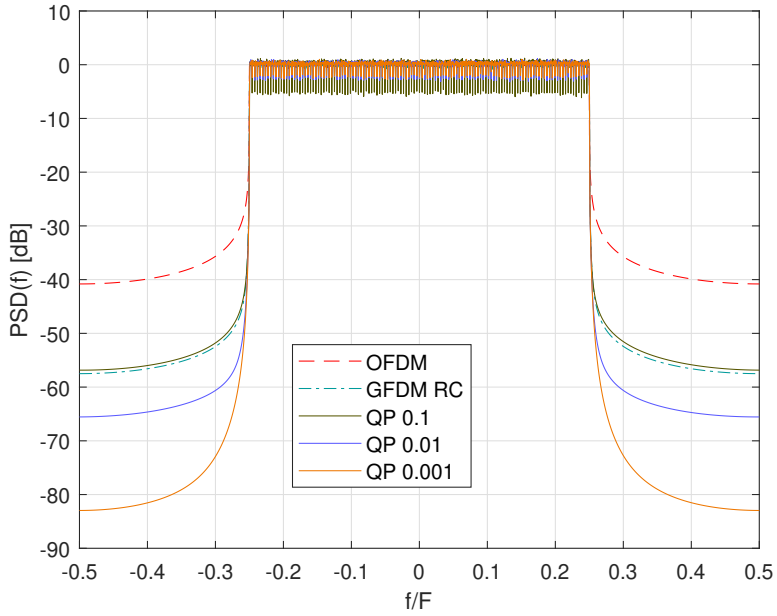

Figure 4.8: Power spectral density (PSD) for OFDM and GFDM. The PSD of the GFDM system using the designed filter of varying σ_p is compared with a GFDM system with RC pulse.

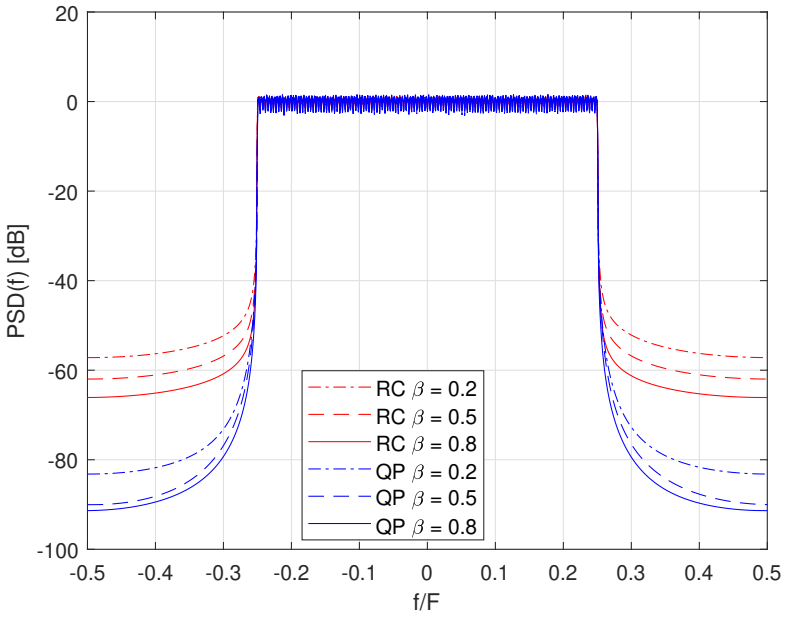

Figure 4.9: PSD of GFDM with RC and designed filter with varying roll-off factor, $\beta = \{0.2, 0.5, 0.8\}$.

4.5 Concluding Remarks

The GFDM system implements the pulse shaping technique in the system model to shift the data symbol into different time and frequency slots. A causal pulse shaping filter design was formulated to minimise the stopband energy subject to a passband constraint. The constraint was linearised and a quadratic programming approach was used to solve the pulse shaping filter design optimisation problem. The numerical results illustrate that using the designed causal filter in GFDM systems is able to reduce the PAPR of the transmitted signal by about 0.3 dB when compared to a GFDM system with the RC filter. It has also been shown that the designed filter is able to minimise the OOB radiation to about -82.95 dB, where the OOB radiation of a GFDM system with RC filter is about -57.48. As the designed causal filter shows promising results in the GFDM system, it is also beneficial to analyse the BER at the receiver.

4.A Appendix: Constraint Simplification

To linearise the inequality constraint (4.11), an additional parameter, θ, is introduced via the real rotation theorem. Eq.(4.11) can be rewritten as

$$\max_{0\leq\theta\leq 2\pi} \Re\{(P(e^{j\omega}) - P_d(\omega))e^{j\theta}\} \leq \sigma_p, \omega \in \Omega_p, \tag{4.14}$$

which is equivalent to

$$\Re\{(\mathbf{h}^{\mathrm{T}}\mathbf{e}(\omega) - P_d(\omega))e^{j\theta}\} \leq \sigma_p, \tag{4.15}$$

for $\omega \in \Omega_p$, $\theta \in [0, 2\pi]$. Rearranging (4.15), the following is obtained

$$\mathbf{h}^{\mathrm{T}}\Re\{\mathbf{e}(\omega)e^{j\theta}\} \leq \sigma_p + \Re\{P_d(\omega)e^{j\theta}\}, \tag{4.16}$$

and can be rewritten as

$$b^{\mathrm{T}}(\omega,\theta)\mathbf{h} \leq c(\omega,\theta), \tag{4.17}$$

where $b(\omega,\theta) = \Re\{\mathbf{e}(\omega)e^{j\theta}\}, c(\omega,\theta) = \sigma_p + \Re\{P_d(\omega)e^{j\theta}\}$.

From (4.17), it can be seen that the new parameter θ is continuous and has increased the number of constraints. In view of (4.12) and (4.17), the optimisation problem is now a semi-infinite QP problem. The number of variables $\mathbf{h}$ to be optimised is finite, but the number of constraints, which are dependent on ω and θ, are infinite. This can be solved via discretisation of the parameters ω and θ using the method in [80]. For simplicity, parameter θ is discretised as a discrete set $\{\theta_i\}_{i=1}^{2q}$ with

$$\theta_i = \frac{\pi(i-1)}{q}, q \geq 2.$$

Furthermore, let us define

$$Y_n^q(\omega) = \max_{1\leq i\leq 2q} \Re\{(\mathbf{h}^{\mathrm{T}}\mathbf{e}(\omega) - P_d(\omega))e^{j\theta_i}\}. \tag{4.18}$$

It was shown in [95] that

$$Y_n^q(\omega) \leq \max_{0\leq\theta\leq 2\pi} \Re\{(\mathbf{h}^{\mathrm{T}}\mathbf{e}(\omega) - P_d(\omega))e^{j\theta}\} \leq Y_n^q(\omega)\sec\left(\frac{\pi}{2q}\right). \tag{4.19}$$

When $q \to \infty$, the value of $\sec(\frac{\pi}{2q}) \to 1$, which indicates that $Y_n^q(\omega)$ gives a decent estimate of $P(e^{j\omega})$. In fact, for $q = 8$, $\sec(\frac{\pi}{2q}) = 1.020$. Hence, instead of using (4.16), the following strengthened inequality constraints over the discrete sets $\{\omega_l\}_{l=1}^{L}$ and $\{\theta_i\}_{i=1}^{2q}$ should be considered

$$\max_{1\leq i\leq 2q} \Re\{\mathbf{h}^{\mathrm{T}}\mathbf{e}(\omega_l)e^{j\theta_i}\} \leq \frac{\sigma_p}{\sec(\frac{\pi}{2q})} + \Re\{P_d(\omega_l)e^{j\theta_i}\}. \tag{4.20}$$

Replacing $\mathbf{e}(\omega_l)$ with $e^{-j\omega_l k}$, (4.20) becomes

$$\max_{1\leq i\leq 2q} \mathbf{h}^{\mathrm{T}}\cos(\omega_l k - \theta_i) \leq \frac{\sigma_p}{\sec\frac{\pi}{2q}} + P_d(\omega_l)\cos(\theta_i), \tag{4.21}$$

which can be simplified to the following set of inequality constraints

$$B_l \mathbf{h} \leq c_l, \tag{4.22}$$

where, for each l, B_l is a $2q$ by M matrix with $b^{\mathrm{T}}(\omega_l, \theta_i) = \cos(\omega_l k - \theta_i)$ as its ith row and c_l is a $2q$-dimensional vector with entries acquired with $c_l = \frac{\sigma_p}{\sec\frac{\pi}{2q}} + P_d(\omega_l)\cos(\theta_i)$.

Chapter 5

GFDM Receiver Performance with Designed Filter

It has been investigated in Chapter 4 that the designed pulse shaping filter can reduce the PAPR and the OOB radiation of the GFDM signal significantly. In this chapter, the BER performance of the GFDM system with the designed pulse shaping filter is analysed and compared with the one of the RC filter. The rest of this chapter chapter is organised as follows: Section 5.1 presents the GFDM receiver model. Section 5.2 describes the non orthogonality in the GFDM systems due to pulse shaping which causes self interference, and a potential method to mitigate the interference using an iterative approach. Numerical results are presented in Section 5.3 to illustrate the BER performance of the designed filter. Finally, concluding remarks are drawn in Section 5.4.

5.1 GFDM Receiver System Model

The received signal, $y[n]$, is represented in a vector as $\mathbf{y} = \{y_0, y_1, \ldots, y_{N-1}\}$, followed by conversion to the frequency domain with $\mathbf{Y} = \mathbf{W}_N\mathbf{y}$, where $\mathbf{W}_N$ is an N-point DFT matrix. It is assumed that the receiver has a perfect time

and frequency synchronization, and perfect CSI is available. To compensate for distortions from the channel and AWGN, the MMSE equaliser can be applied, and can be expressed as

$$\hat{\mathbf{Y}} = \mathbf{\Gamma}\mathbf{Y}, \tag{5.1}$$

where $\mathbf{\Gamma} = \text{diag}\{\gamma, \gamma_1, \ldots, \gamma_{N-1}\}$ is an $N \times N$ diagonal matrix with entries from the weighting parameters of the MMSE equaliser.

To recover the transmitted data symbols, the equalised signal is applied with a transpose of the permutation matrix, $\mathbf{\Psi}^{\text{T}}$, a matched filtering, $\mathbf{P}^{\text{H}}$, the downsampling parameter, $\mathbf{\Lambda}^{\text{T}}$, with a downsampling factor of $V = 2$, and the M-point inverse discrete Fourier transform (IDFT), $\mathbf{W}_M^{\text{H}}$. The recovered data symbols for the kth subcarrier can be written as [87]

$$\hat{\mathbf{x}}_k = \mathbf{W}_M^{\text{H}} \mathbf{\Lambda}^{\text{T}} \mathbf{P}^{\text{H}} \mathbf{\Psi}^{\text{T}} \hat{\mathbf{Y}}. \tag{5.2}$$

5.2 Self Interference due to Non-Orthogonality

As shown earlier in Chapter 4 Fig. 4.1, the filters of a subcarrier occupies twice the amount of the subcarrier bandwidth. Therefore, there will be overlap between adjacent subcarriers, i.e., subcarrier k will be interfered by the filters of subcarrier $k-1$ and subcarrier $k+1$. Although the matched filtering process is applied at the receiver, the interfering portions of the neighbouring subcarriers remain. as shown in Fig. 5.1. The solid line represents the filter for the subcarrier of interest, the dashed line represents the filter of adjacent subcarrier, and the dashed dot line represents interference due to the overlapping of the two adjacent subcarriers.

The interfering portion is obtained by $\mathbf{P}^{(\text{f})}\mathbf{P}^{(\text{r})}$, where $\mathbf{P}^{(\text{f})}$ and $\mathbf{P}^{(\text{r})}$ is the falling flank and rising flank, respectively, of the pulse shaping filter in the frequency domain.

To remove the interfering portion $\mathbf{P}^{(\text{f})}\mathbf{P}^{(\text{r})}$, the received signal of kth subcarrier

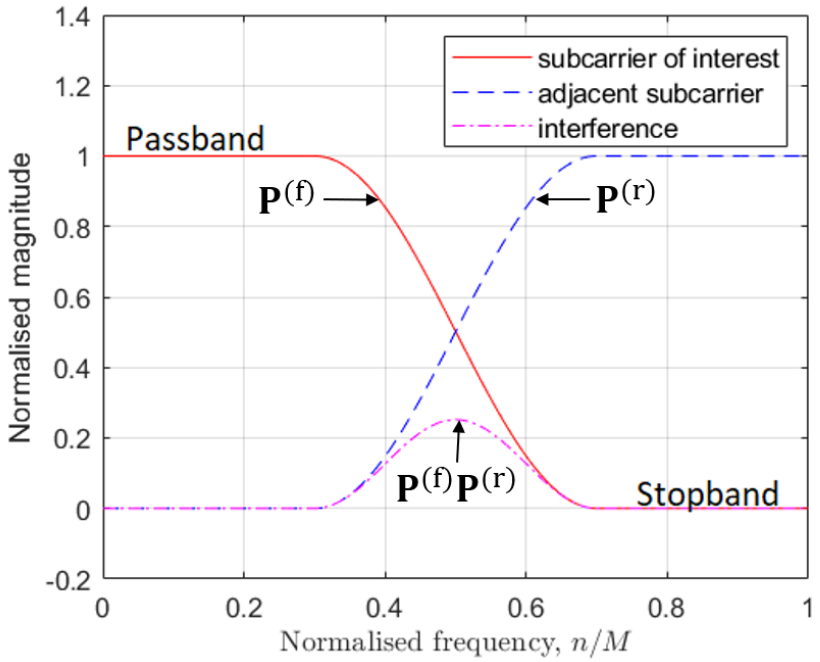

Figure 5.1: Illustration of the filter flanks in the frequency domain with filter roll-off factor $\beta = 0.4$.

can be split into the signal of interest and interfering signal. Let $\mathbf{y}_k$ be expressed in terms of the useful signal and interfering signal for the kth subcarrier, which can be written as

$$\begin{aligned}\mathbf{y}_k &= \mathbf{\Lambda}^{\mathrm{T}}\mathbf{P}^{\mathrm{H}}\mathbf{\Psi}^{\mathrm{T}}\hat{\mathbf{Y}} \\ &= \underbrace{\mathbf{P}^{(\mathrm{r})}\mathbf{P}^{(\mathrm{r})}\mathbf{X}_k + \mathbf{P}^{(\mathrm{f})}\mathbf{P}^{(\mathrm{f})}\mathbf{X}_k}_{\text{signal}} + \underbrace{\mathbf{P}^{(\mathrm{r})}\mathbf{P}^{(\mathrm{r})}\mathbf{X}_{k-1} + \mathbf{P}^{(\mathrm{f})}\mathbf{P}^{(\mathrm{f})}\mathbf{X}_{k+1}}_{\text{interference}} \\ &= \mathbf{X}_k + \mathbf{P}^{(\mathrm{f})}\mathbf{P}^{(\mathrm{r})}(\mathbf{X}_{k-1} + \mathbf{X}_{k+1}),\end{aligned} \tag{5.3}$$

where in an ideal case that the data symbol is able to be perfectly recovered, $\mathbf{x}_k = \mathbf{W}_M^{\mathrm{H}}\mathbf{X}_k$ will yield the transmitted data symbol for the kth subcarrier. When the transmitted signal is subjected to interference, a decision rule is used to map $\mathbf{W}_M^{\mathrm{H}}\mathbf{y}_k$ to the closest QAM points in the constellation grid of the transmitted signal to obtain $\hat{\mathbf{x}}_k$.

With (5.3), the interference due to adjacent the pulse shaping filter of adjacent

subcarriers can be minimized through an iterative approach as the one proposed in [87]. The number of iterations is represented by $j = 1, \ldots, \mathcal{J}$, and the vectors $\mathbf{y}_k$ and $\hat{\mathbf{x}}_k$ are extended by the iteration index to $\mathbf{y}_k^{(j)}$ and $\hat{\mathbf{x}}_k^{(j)}$, respectively. The pseudo-code of the interference cancellation (IC) algorithm is given in [87] and described in Alg. 1.

Algorithm 1 An Iterative Interference Cancellation Algorithm [87]

receive all subcarriers as $\mathbf{W}_M^H \mathbf{y}_k^{(0)}$
map each symbol to closest QAM point to obtain $\hat{\mathbf{x}}_k^{(0)}$
for $j = 1$ to $\mathcal{J}$ **do**
  for $k = 0$ to $K - 1$ **do**
    remove interference by computing
    $\mathbf{y}_k^{(j)} = \mathbf{y}_k^{(0)} - \mathbf{P}^{(\mathrm{r})}\mathbf{P}^{(f)}\mathbf{W}_M(\hat{\mathbf{x}}_{k-1 \bmod K}^{(j-1)} + \hat{\mathbf{x}}_{k+1 \bmod K}^{(j-1)})$
    update the received symbols with $\mathbf{W}_M^H \mathbf{y}_k^{(j)}$
    map each symbol to closest QAM point to obtain $\hat{\mathbf{x}}_k^{(j)}$
  end for
end for

5.3 Numerical Results

In this section, simulations are carried out to investigate the BER performance of the GFDM signal with the designed pulse shaping filter, QP-GFDM, as compared to the GFDM system with ideal RC filter, RC-GFDM, and the OFDM system. The following parameters are used for simulating the BER results: 16-QAM modulation, subcarrier number $K = 128$, subsymbols number $M = 15$, and filter roll-off $\beta = 0.2$. The BER is analysed with respect to different levels of energy per bit to noise power spectral density ratio, EbN0. The channels considered are the AWGN channel and the HIPERLAN/2 channel. For the HIPERLAN/2 channel, the channel model A is selected to investigate the BER performance in an indoor office environment.

Using a lower roll-off factor will yield a worse PAPR performance but will be able to suppress the OOB radiation better. Hence, the BER performance of

using different roll-off factors in the GFDM system is investigated. The filter roll-off is varied according to $\beta = \{0.2, 0.4, 0.5\}$. The BER performance over an AWGN channel and the HIPERLAN/2 channel is as illustrated in Fig. 5.2 and Fig. 5.3, respectively. It can be observed from both figures that the GFDM systems have a poorer BER performance as compared with the OFDM system, where the GFDM systems have error floors even as the EbN0 is increased. This is due to the signal being deteriorated by the self interference of the adjacent pulse shaping filters and cannot be properly removed using channel equalisers and matched filters, as described in (5.3) and shown in Fig. 5.1. When the filter roll-off, β, is increased, the BER is worse, as there will be more overlapping of the pulse shaping filters in the GFDM system. Hence, the impact of self interference is greater. Comparing the performance between QP-GFDM and RC-GFDM, the QP-GFDM has a significantly better BER when $\beta = 0.2$. At $\beta = 0.4$, the BER is similar for both systems, and at $\beta = 0.5$, the RC-GFDM is slightly better.

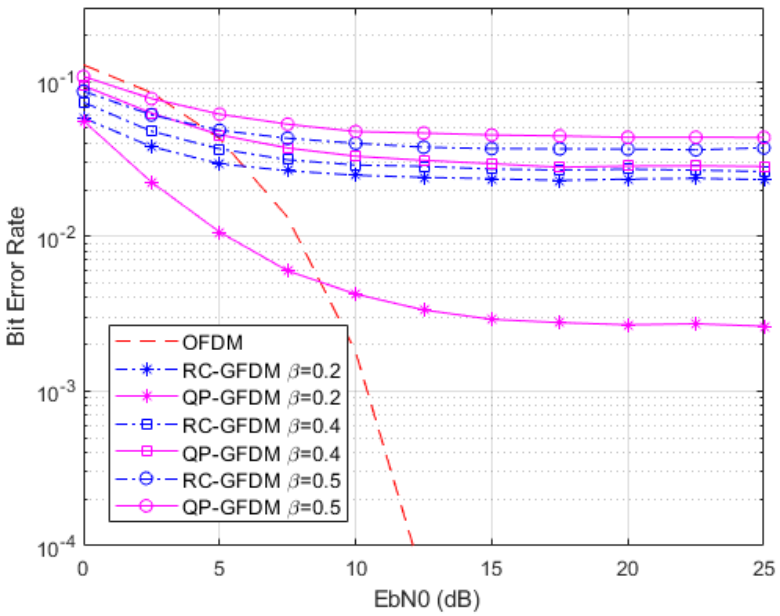

Figure 5.2: BER of the QP-GFDM system over an AWGN channel compared with RC-GFDM and OFDM, where $K = 128$, $M = 15$, $\beta = \{0.2, 0.4, 0.5\}$.

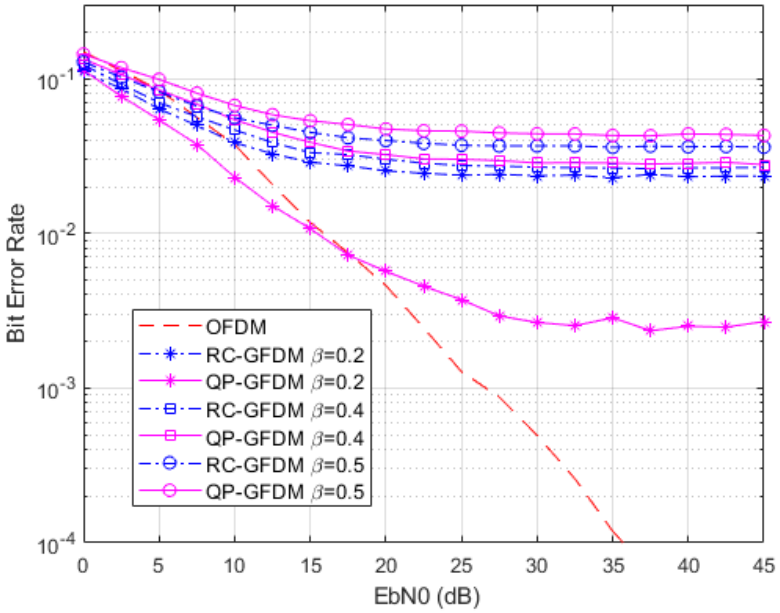

Figure 5.3: BER of the QP-GFDM system over the HIPERLAN/2 channel A compared with RC-GFDM and OFDM, where $K = 128$, $M = 15$, $\beta = \{0.2, 0.4, 0.5\}$.

Next, the effect of using different passband tolerance, σ_p, in the pulse shaping filter design is analysed. As illustrated in Fig. 4.3 on page 52, the baseband frequency response of the designed filter with lower tolerance has a better approximate of the ideal RC filter. The designed filter with more tolerance has larger ripples, and can severely degrade the BER performance in the GFDM system as shown in Fig. 5.4 and Fig. 5.5. It can also be deduced that using the passband tolerance of $\sigma_p = 0.001$ is sufficient as it has the best BER performance among the GFDM systems.

To mitigate the self interference, the IC algorithm in Alg. 1 is applied. The BER performance of the QP-GFDM system at different number of IC algorithm iterations is analysed over the AWGN and the HIPERLAN/2 channel. From Fig. 5.6 and Fig. 5.7, the optimal number of iterations can be identified as $\mathcal{J} = 4$ as increasing it further yields no further BER improvement, but increases the complexity at the GFDM receiver. Therefore, in the rest of the BER analysis in this chapter, the IC algorithm iterations is set at $\mathcal{J} = 4$.

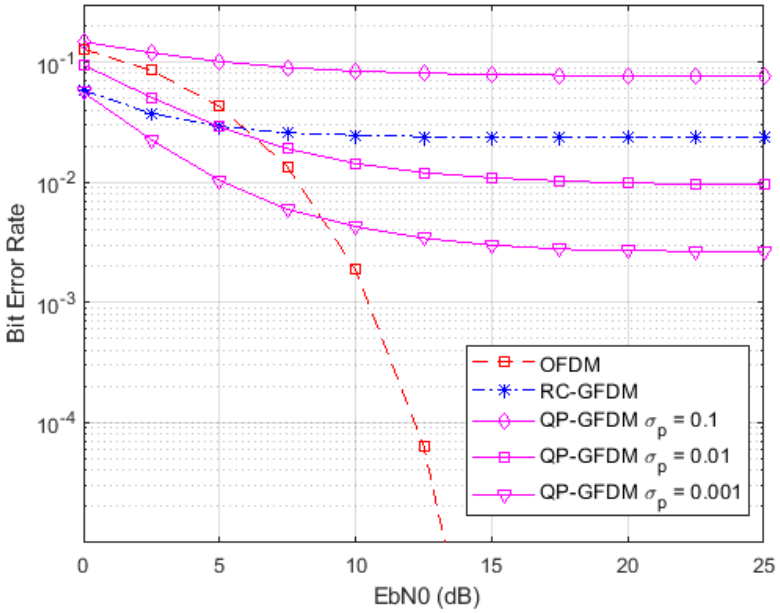

Figure 5.4: BER of the QP-GFDM system over an AWGN channel, with different passband tolerance, $\sigma_p = \{0.1, 0.01, 0.001\}$.

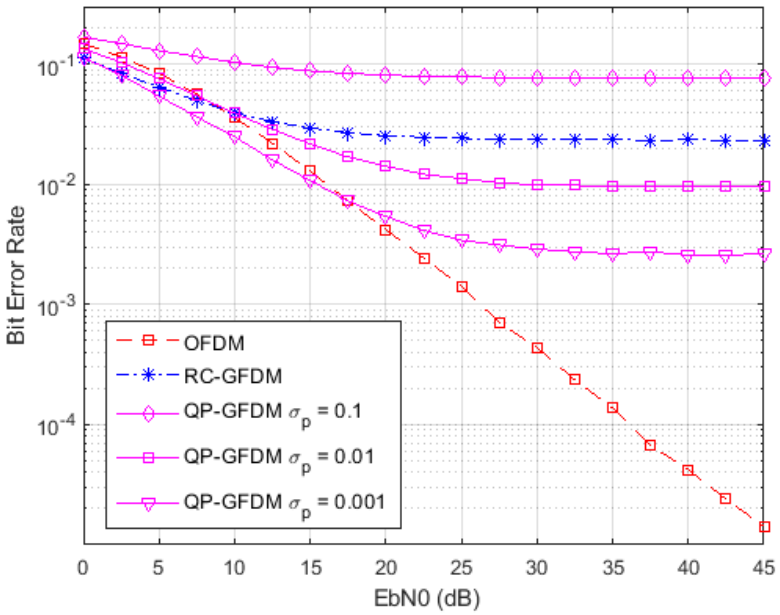

Figure 5.5: BER of the QP-GFDM system over the HIPERLAN/2 channel, with different passband tolerance, $\sigma_p = \{0.1, 0.01, 0.001\}$.

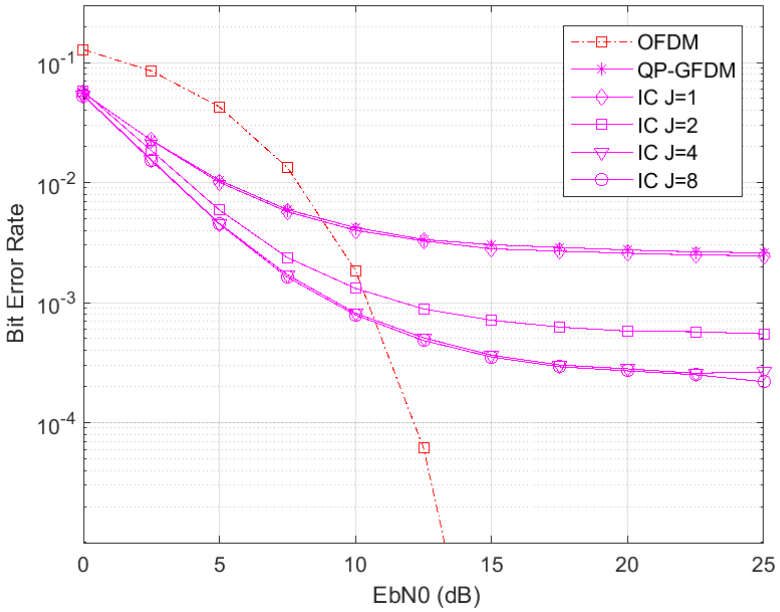

Figure 5.6: Effect of the interference cancellation algorithm iterations on QP-GFDM over an AWGN channel.

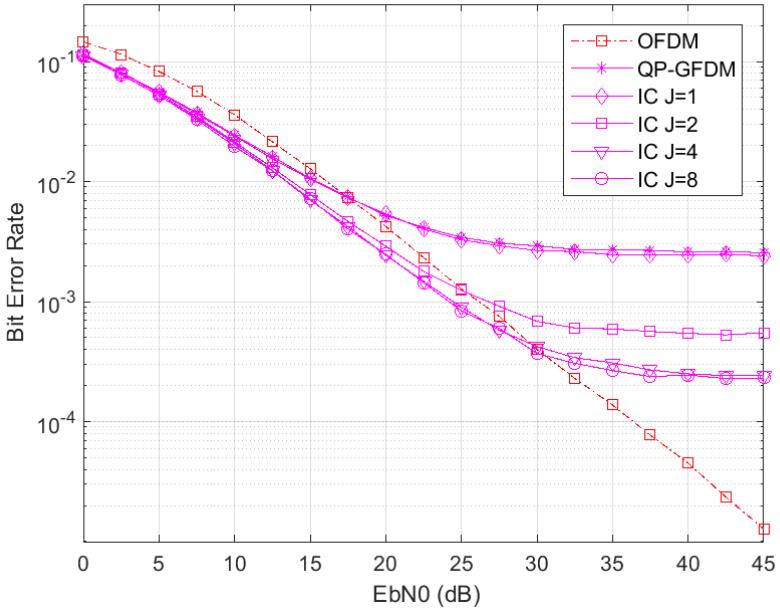

Figure 5.7: Effect of the interference cancellation algorithm iterations on QP-GFDM over the HIPERLAN/2 Channel A.

Fig. 5.8 and Fig. 5.9 shows the effect of using the IC algorithm on the GFDM system with designed filter of different passband tolerance. Although the designed pulse shaping filter has a better BER performance as shown earlier in Fig. 5.4 and Fig. 5.5, implementing the IC algorithm allows the GFDM system with the ideal RC filter to perform better. These results indicate that the IC algorithm originally proposed in [87] may not be optimal in removing self interference in GFDM systems with different types of pulse shaping filters.

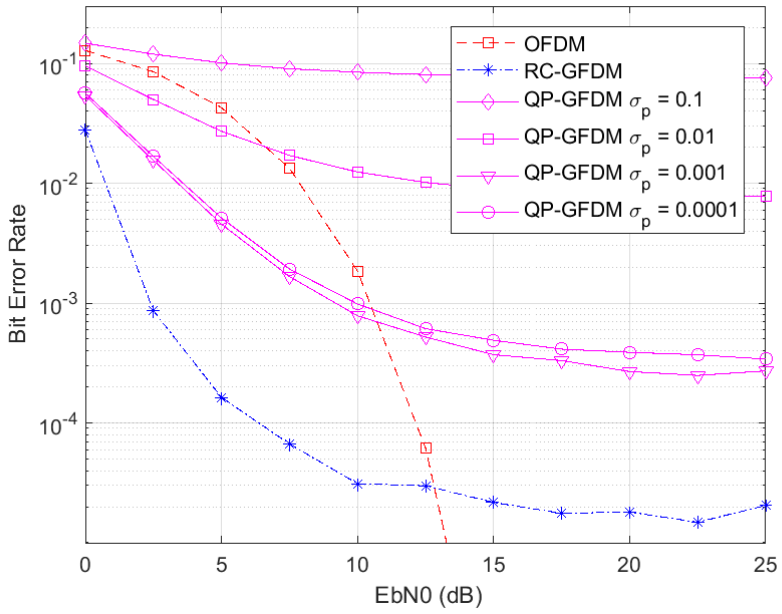

Figure 5.8: BER of the QP-GFDM system using different passband tolerance levels, σ_p, when transmitted over an AWGN channel.

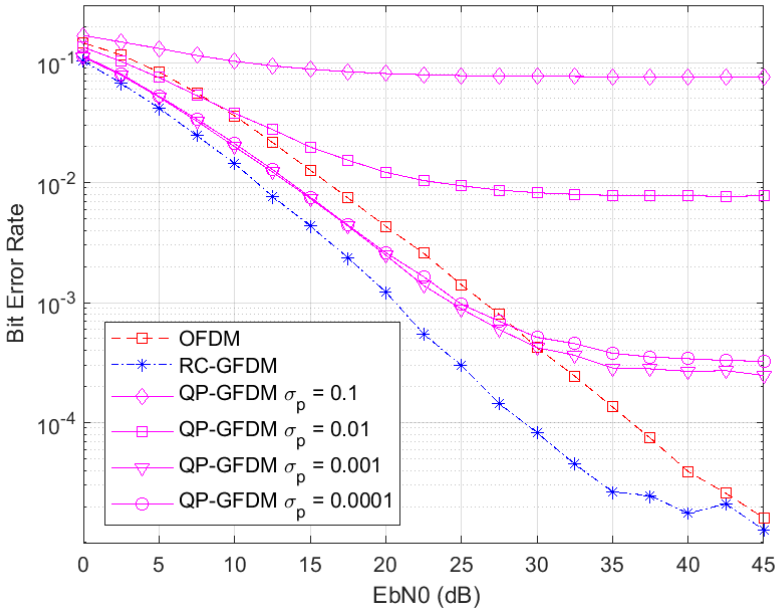

Figure 5.9: BER of the QP-GFDM system using different passband tolerance levels, σ_p, when transmitted over the HIPERLAN/2 Channel A.

5.4 Concluding Remarks

In this chapter, the BER performance of the GFDM system using the designed filter is analysed and compared with the one with ideal RC filter. At the receiver, it can be seen that the self interference degrades the BER of the GFDM system. Implementing an iterative interference cancellation algorithm at the receiver can improve the BER performance. The GFDM system with the designed filter suffer lower SNR than the OFDM system at a BER of 10^-3, but by using the interference cancellation algorithm with $\mathcal{J} = 4$ iterations, the SNR can be improved to 25 dB. Apart from analysing the BER of the GFDM system, it is good to understand the additional complexity and the energy efficiency of the GFDM system.

Chapter 6

Impact of the PAPR Towards HPA Nonlinearity

In Chapter 4, an optimal filter has been designed for the GFDM system using computationally efficient optimisation method. The designed filter has been shown to be effective in reducing the PAPR and minimising the OOB radiation. In Chapter 5, the performance of the GFDM system using the designed filter has been analysed at the receiver. However, analysis of the GFDM system performance from the previous chapters did not consider the effects of HPA nonlinearity.

In practice, the GFDM signal is passed to the HPA before being transmitted to the communication channel. As HPA is a nonlinear device, it may change the characteristics of the system performance, especially when the HPA operates in the nonlinear region due to high PAPR of the GFDM signals. In particular, nonlinear characteristic may lead to BER degradation and spectral regrowth which reduces the spectral efficiency [43], [96], [97]. The HPA can be operated with a large IBO in order to linearly amplify the GFDM transmitted signal, but doing so results in low HPA efficiency [98]. As the HPA contributes to more than half of the energy consumption in wireless communication systems [99], [100], ensuring high energy efficiency is essential especially for battery-powered mobile devices.

Hence, there is a tradeoff between spectral efficiency and energy efficiency when considering the HPA nonlinearity in the GFDM system.

In this chapter, a holistic approach is utilised to analyse the performance of the designed filter for GFDM presented in Chapter 4 when a nonlinear HPA is applied. The rest of the chapter is organised as follows: Firstly, an overview of the HPA and the different models of HPA is presented in Section 6.1. Next, several performance metrics in analysing the performance of systems that are subjected to HPA nonlinearity is presented in Section 6.2. This is followed by the numerical results of the performance of multicarrier systems with HPA nonlinearity in Section 6.3, where the designed pulse shaping filter in GFDM is compared with the ideal RC filter in GFDM and the conventional OFDM system. Finally, concluding remarks are drawn in Section 6.4.

6.1 The High Power Amplifier

Consider a GFDM system with HPA as shown in Fig. 6.1. After converting the discrete-time GFDM signal $s[n]$ into a continuous time signal $s(t)$ via a digital-to-analog converter (DAC), the signal is passed to a HPA before the actual transmission. Let $s(t) = r(t)e^{j\phi(t)}$ denote the baseband representation of the input signal to the HPA, where $r(t) = |s(t)|$ is a positive continuous random variable denoting the envelope of $s(t)$ and $\phi(t)$ denotes the phase at a given time instant t. The output of the HPA is given by [43]

$$\tilde{s}(t) = g(r(t))e^{j\Phi(r(t))}e^{j\phi(t)}, \tag{6.1}$$

where $g(r)$ and $\Phi(r)$ are the time-domain envelope and phase responses commonly referred to as AM-AM and AM-PM characteristics, respectively, for a given instantaneous envelope $r(t)$.

Various HPA models have been proposed in the literature, such as the Rapp's model [101], Saleh's model [102], and the Ghorbani's model [103]. The Rapp's

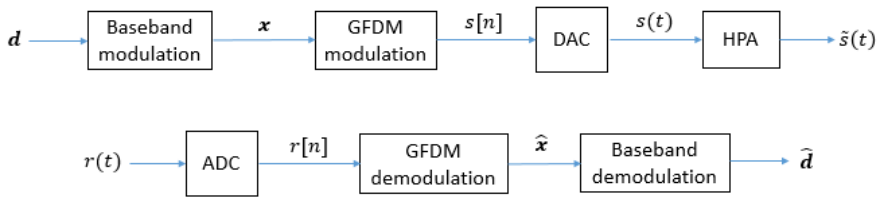

Figure 6.1: System model of GFDM transceiver.

model is commonly used to model the envelope characteristics of the solid-state power amplifier (SSPA), the Saleh's model is for modeling the traveling wave tube amplifier (TWTA), and the Ghorbani's model is for modeling field-effect transistor (FET) amplifiers. In this work, the Rapp's model is used to represent a practical memoryless SSPA model with nonlinearity. The Rapp's model has been widely applied in recent works to simulate the nonlinearity effects of the HPA [104]–[107], and is also used in evaluating the 5G-NR [108]. The AM-AM characteristic of the Rapp's model can be expressed as

$$g(r) = r_{out} = r_{out,max} \frac{\frac{r_{in}}{r_{in,max}}}{\left(1 + \left(\frac{r_{in}}{r_{in,max}}\right)^{2p}\right)^{\frac{1}{2p}}}, \tag{6.2}$$

and the AM-PM characteristic is assumed to be insignificant, which can be expressed as

$$\Phi(r) = 0. \tag{6.3}$$

Parameter p is a positive value that controls the smoothness of the curve, with $p \to \infty$ corresponding to an ideally linearised model. The normalized output of a Rapp's model with respect to different p is as shown in Fig. 6.2. Parameter r_{in} denotes the input envelope to the HPA, $r_{\text{in,max}}$ is the maximum saturation point of the HPA input , r_{out} is the output envelope from the HPA, and $r_{\text{out,max}}$ is the maximum saturation point of the HPA output.

A modified Rapp's model has been proposed in [109] which includes phase characteristics. However, the current work is more concerned on the impacts of

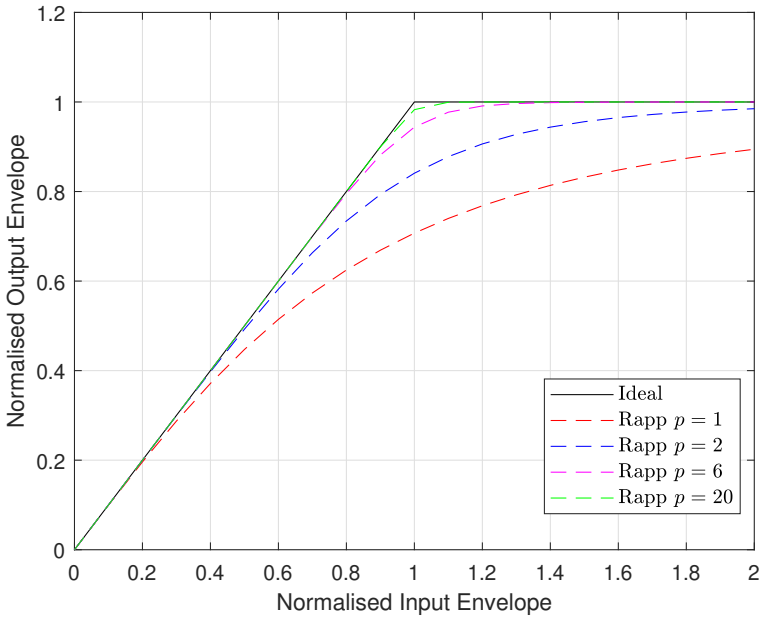

Figure 6.2: AM-AM characteristics of the Rapp's Model with several smoothness factors p.

the PAPR of transmit signals on the system performance due to HPA nonlinearity. It has been shown in [109] that the envelope transfer characteristics of the modified Rapp's model and the original Rapp's model in [101] are very close. Hence, the Rapp's model is sufficient to be used for the works in this thesis.

6.2 HPA Performance Measurement

6.2.1 HPA Efficiency

The efficiency of the HPA can be expressed as the ratio of the average output power from the HPA $\mathcal{P}_{out} = E\{r_{out}^2\}$, to the DC power supplied to the HPA $\mathcal{P}_{DC}$ [43]

$$\eta = \frac{\mathcal{P}_{out}}{\mathcal{P}_{DC}}. \tag{6.4}$$

In general, the efficiency η depends on the class of the HPA. In this work, the

Class-A and Class-B HPA are considered as they are commonly used for mobile terminals. The efficiency of the Class-A and Class-B HPA are respectively given by [110]

$$\eta_A = \frac{1}{2}\frac{E\{r_{out}^2\}}{r_{out,max}^2}, \tag{6.5}$$

and

$$\eta_B = \frac{\pi}{4}\frac{E\{r_{out}^2\}}{r_{out,max}E\{r_{out}\}}. \tag{6.6}$$

The efficiency of the HPA can be improved by scaling the signal input power such that the signal is within the linear region and not exceeding the saturation point. This can be done by applying an IBO to the input signal, which is given by [110]

$$\text{IBO} \triangleq \frac{r_{in,max}^2}{\mathcal{P}_{in}}, \tag{6.7}$$

where $\mathcal{P}_{in} = E\{r_{in}^2\}$ denotes the average input power. Similarly, the output backoff (OBO) can be defined as

$$\text{OBO} \triangleq \frac{r_{out,max}^2}{\mathcal{P}_{out}}. \tag{6.8}$$

When the linear amplification reaches up to the saturation point, the OBO (6.8) will be equivalent to the IBO (6.7) and the PAPR (3.29). Using the relationship of the HPA efficiency and OBO given in [111], (6.5) and (6.6) can be rewritten, respectively, as

$$\eta_A = 0.5\frac{1}{PAPR}, \tag{6.9}$$

and

$$\eta_B = 0.78\frac{1}{PAPR}. \tag{6.10}$$

From (6.9) and (6.10), it can be seen that the PAPR of the signal affects the efficiency of the HPA. Efficiency can be also be improved by reducing the IBO. However, signal that exceeds the saturation point will be clipped and will lead to undesired spectral growth.

6.2.2 Spectral Regrowth

For the sake of simplicity, it is useful to linearise the non-linearity of the HPA as follows [53]

$$\tilde{S}_n = \alpha S_n + D_n, \tag{6.11}$$

where S_n and $\tilde{S}_n$ are the Fourier transforms of the HPA input signal $s(t)$ and output signal $\tilde{s}(t)$, respectively. Parameter α represents the attenuation factor and D_n denotes the non-linear distortion component caused by the HPA. Assuming that D_n and S_n are statistically uncorrelated, the attenuation factor α can be obtained using

$$\alpha = \frac{E\{\tilde{S}_n S_n^{\dagger}\}}{E\{|S_n|^2\}} = \frac{E\{\tilde{S}_n S_n^{\dagger}\}}{\mathcal{P}_s}, \tag{6.12}$$

where $\{\cdot\}^{\dagger}$ denotes conjugate, and $\mathcal{P}_s = E\{|S_n|^2\}$ is the average power of S_n.

The average power of the non-linear distortion component D_n can expressed as [53]

$$\tilde{\mathcal{P}}_{d,n} = \tilde{\mathcal{P}}_s - \tilde{\mathcal{P}}_{s,n}, \tag{6.13}$$

where $\tilde{\mathcal{P}}_{s,n} = \alpha^2 \mathcal{P}_s$ is the power of the attenuated signal and $\tilde{\mathcal{P}}_s = E\{|\tilde{S}_n|^2\}$ is the power of the HPA output signal.

Using (6.13), the spectral regrowth can be measured using the adjacent channel leakage ratio (ACLR) [112] by the ratio of the out-of-band power emission and the in-band signal power, written as [110]

$$ACLR \triangleq \frac{\sum_{n=N}^{3N/2-1} \tilde{\mathcal{P}}_{d,n}}{\sum_{n=\frac{N}{2}}^{N-1} \tilde{\mathcal{P}}_{s}}. \tag{6.14}$$

where N is the total number of data symbols.

In this chapter, without loss of generality, the ACLR is used to measure the OOB radiation of the signal.

6.2.3 Effective SNR

The receiver performance can be analysed by measuring the SNR, which is defined as

$$SNR = \frac{\mathcal{P}_{out}}{\mathcal{P}_z}, \tag{6.15}$$

where $\mathcal{P}_z$ is the noise power and $\mathcal{P}_{out}$ is the HPA average output power. However, when the HPA power $\mathcal{P}_{DC}$ in (6.4) is fixed, a signal with a higher efficiency will achieve a higher average output power $\mathcal{P}_{out}$. Different systems will have different efficiency at a given IBO or ACLR. Therefore, the receiver performance should be evaluated in a unified manner using the effective SNR, defined as [110]

$$\begin{aligned} SNR_{eff} &= \frac{\mathcal{P}_{DC}}{\mathcal{P}_z} = \frac{\mathcal{P}_{out}}{\eta \mathcal{P}_z} \\ &= \frac{1}{\eta} SNR. \end{aligned} \tag{6.16}$$

6.2.4 Spectral efficiency

By comparing the transmitted data and recovered data, the spectral efficiency of the system can be evaluated using the average mutual information (AMI) [99]. The AMI, denoted by $I(\mathcal{X};\mathcal{Y})$, measures the dependence of two sets of random variables $\mathcal{X}$ and $\mathcal{Y}$, where an $I(\mathcal{X};\mathcal{Y}) = 0$ represents total independence of the random variables. The AMI can be used to measure the spectral efficiency

when the signal is transmitted over a wireless channel, such as the AWGN and multipath channels. The spectral efficiency (SE) of the system can be obtained from the AMI as [99],

$$\text{SE} = \text{AMI} = \frac{I(\mathcal{X};\mathcal{Y})}{N} \tag{6.17}$$

where

$$I(\mathcal{X};\mathcal{Y}) = \sum_{y\in\mathcal{Y}}\sum_{x\in\mathcal{X}} p(x,y)\log\frac{p(x,y)}{p(x)p(y)}, \tag{6.18}$$

is the mutual information, $p(x,y)$ is the joint distribution of $\mathcal{X}$ and $\mathcal{Y}$, and $p(x)$ and $p(y)$ are the marginal distributions of $\mathcal{X}$ and $\mathcal{Y}$ respectively. To compute the AMI of the GFDM system using (6.18), $\mathcal{X}$ is used to represent the input data symbols $\mathbf{x}$ while $\mathcal{Y}$ is the recovered data symbols $\hat{\mathbf{x}}$.

6.2.5 Energy Efficiency

Complex receivers are often implemented to suppress the self interference due to pulse shaping, as well as non-linearity distortion by the HPA. Hence, it is essential to analyse the processor power consumption based on the complexity and its spectral efficiency. The energy efficiency (EE) of a system can be measured using [113]

$$\text{EE} = \frac{\Omega(\text{SE})}{\mathcal{P}_c}, \tag{6.19}$$

where Ω is the total bandwidth occupied, SE is the spectral efficiency of the system, and $\mathcal{P}_c$ is the power consumed from the processing of the signal at both the transmitter and receiver.

6.3 Numerical Results

Throughout the simulations, unless specified, the following parameters are used for the GFDM systems: 16-QAM modulation, number of subcarriers $K = 128$, and number of subsymbols $M = 15$. The performance of an OFDM system and GFDM system using RC filter with similar roll-off factor to the designed QP filter will be evaluated and compared. In the OFDM system, the subcarriers and subsymbols is set at $K_{ofdm} = K \times M$ and $M_{ofdm} = 1$ respectively. For simplicity, the GFDM with RC filter will be referred to as RC-GFDM, while the GFDM system with the proposed designed pulse shaping filter via QP approach will be referred to as QP-GFDM.

6.3.1 PAPR and HPA efficiency

As illustrated in Fig. 6.3, when considering the PAPR at 10^{-3} probability, the PAPR of QP-GFDM is about 12.2 dB, 0.3 dB lower than RC-GFDM, while OFDM has a PAPR of 12 dB. In general, a lower PAPR will reflect a higher HPA efficiency, as a larger portion of the input power to the HPA, $\mathcal{P}_{DC}$, is used to amplify the input signal. A higher PAPR would mean that more power is wasted and dissipated as heat, hence lower HPA efficiency. Due to the wide dynamic range of multicarrier modulation techniques such as OFDM and GFDM, the PAPR is often high and thus have very low HPA efficiency.

As shown in Fig. 6.4, the OFDM system has a slightly higher HPA efficiency when compared with the GFDM systems. The efficiency difference between RC-GFDM and QP-GFDM is very minimal, with QP-GFDM having a better efficiency performance than RC-GFDM. This is due to the lower PAPR of the QP-GFDM signal when compared to RC-GFDM as shown in Fig. 4.4

It can be seen from Fig. 6.4 that the efficiency of the HPA can go as low as 1% for Class-A amplifier and 9% for Class-B amplifier, when the IBO is increased to allow for the HPA to operate in the linear region. It can also be deduced that

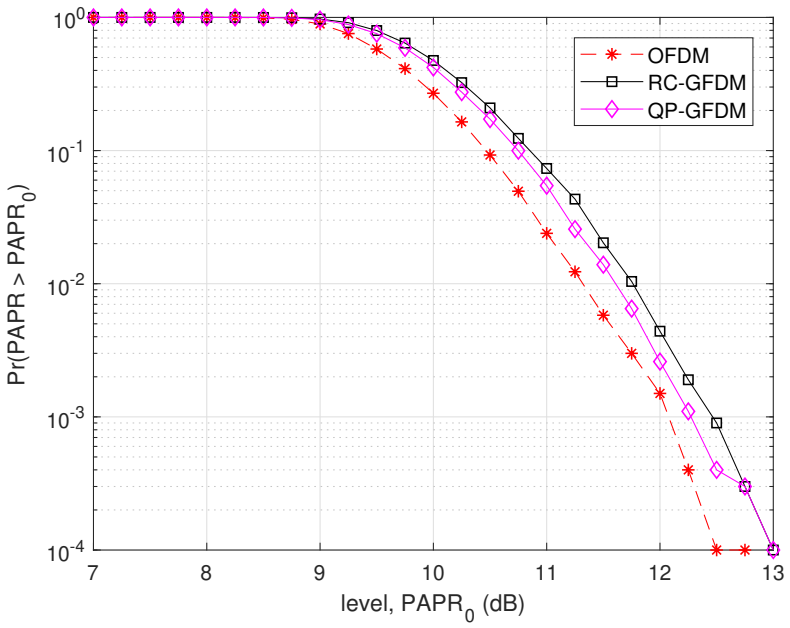

Figure 6.3: CCDF analysis of PAPR of different signals.

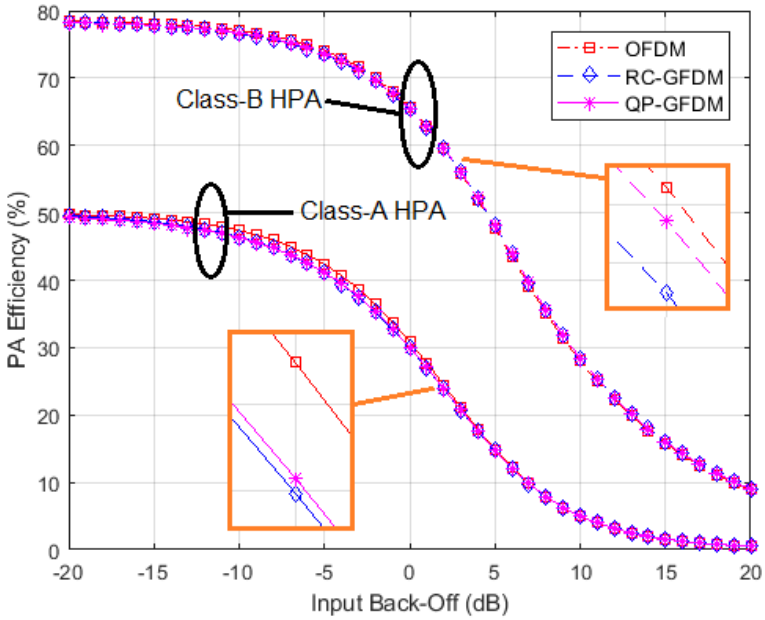

Figure 6.4: Relationship between the IBO level and the efficiency of the designed filter.

the maximum achievable efficiency is achieved when the PAPR approaches unity as a result of lower IBO, with around 50% for Class-A HPA and 78% for Class-B

HPA, aligning with (6.9) and (6.10) respectively. However, this also means that a greater portion of the signal exceeds the HPA saturation region and is clipped, resulting in spectral regrowth.

6.3.2 PSD and ACLR

Fig. 6.5 illustrates the ACLR of each signal to show the amount of spectral regrowth due to the HPA non-linearity, with respect to different levels of IBO. Ideally, the IBO needs to be as low as possible in order to obtain a higher HPA efficiency. On the other hand, the IBO level should be high enough to minimize the ACLR as a result from HPA non-linearity distortion. Due to the scarcity of available spectrum for data transmission, channels of different users need to be arranged closely. Hence, the need for a lower OOB emission outweighs the HPA efficiency, where 5G New Radio (NR) specifications has specified the ACLR limit to be -45 dB [114]. From Fig. 6.5, any IBO levels of lower than 8.4 dB, 8.7 dB, and 8.6 dB for OFDM, RC-GFDM, and QP-GFDM, respectively, will not be acceptable as the resultant ACLR is greater than -45 dB. In the following numerical simulations, the IBO is set to satisfy the ACLR limit of -45 dB, unless mentioned otherwise.

In Fig. 6.6, the trade-off between the HPA efficiency and ACLR can be observed, with the IBO as the controlled variable. At ACLR $= -45$ dB, the efficiency of OFDM, RC-GFDM, and QP-GFDM with Class-A amplifiers are obtained as 7.2%, 6.6%, and 6.7%, respectively, with Class-B amplifiers 33.5%, 32.7%, and 33.0%, respectively. The IBO levels and amplifier efficiencies obtained at ACLR $= -45$ dB can be observed to have a relationship with the PAPR of each respective systems shown in Fig. 4.4, where a higher PAPR requires a higher IBO, hence a lower HPA efficiency.

To view the effects of HPA non-linearity from another angle, the PSD before and after HPA is shown in Fig. 6.7. Although the GFDM signal experienced spectral regrowth, the OOB radiation of the GFDM signal is still lower than

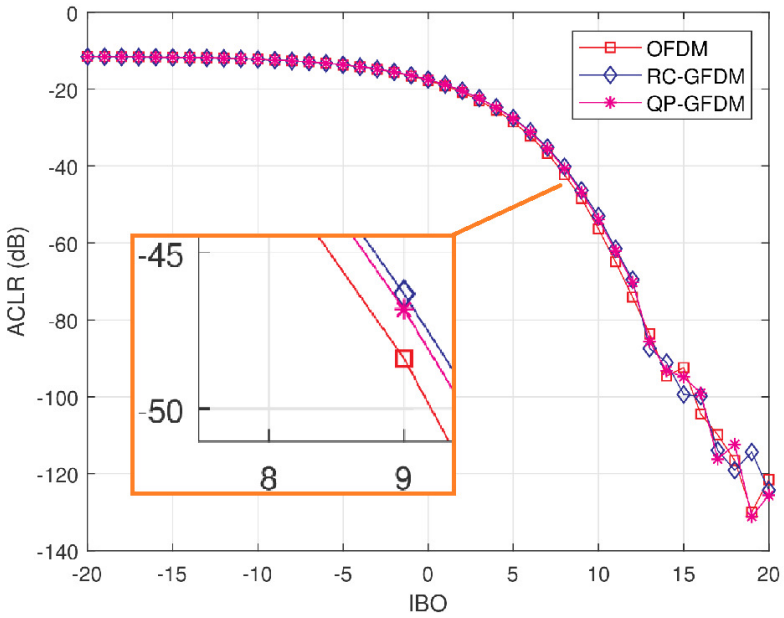

Figure 6.5: Relationship between the IBO level and the ACLR.

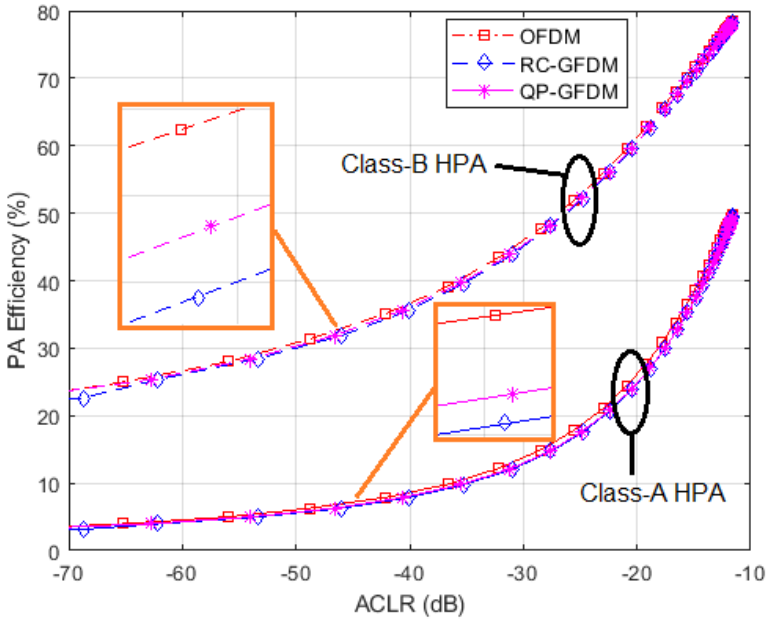

Figure 6.6: Relationship between the ACLR and the HPA efficiency.

OFDM, and is also within acceptable levels. The low OOB radiation is essential in wireless communications, and in particular for IoT networks, as this allows more devices to occupy the channel bandwidth with minimum interference to

each other.

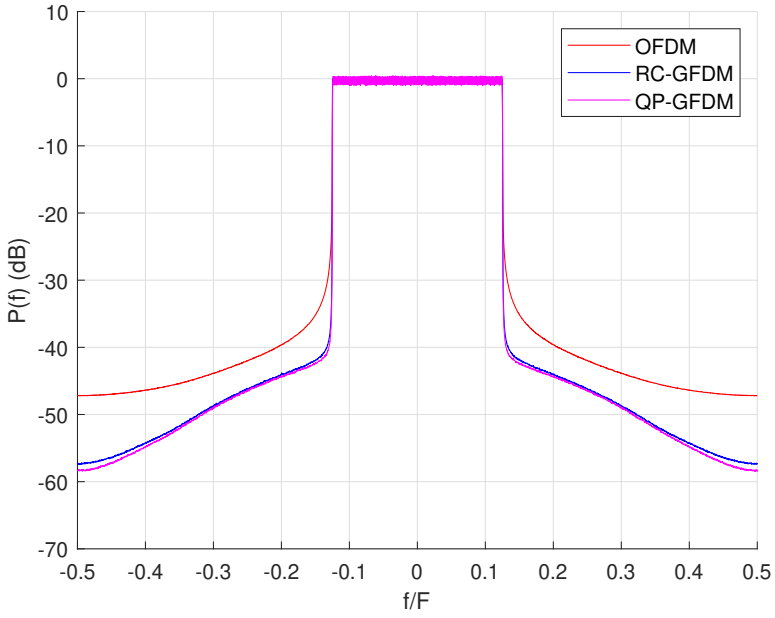

Figure 6.7: Power Spectral Density of the different signals after HPA non-linearity.

6.3.3 BER

To analyse the performance of the GFDM system at the receiver, the transmitted signal is passed through a Rayleigh fading channel, where the HIPERLAN/2 Class A channel model is used [81]. It is assumed that the system has a guard interval larger than the delay spread of the channel, and the receiver has perfect and instantaneous knowledge of the CSI.

As shown in Fig. 6.8, QP-GFDM has a better BER performance as compared with RC-GFDM when analysed using the conventional signal-to-noise power ratio (SNR). Due to the self interference from pulse shaping in GFDM systems, an error floor exists in the GFDM system. Thus, the BER of GFDM is often worse than OFDM. Although the MMSE equalizer is applied, it is often not enough to compensate for the distortion due to non-linearity.

To present a unified analysis of the BER, the BER performance is evaluated

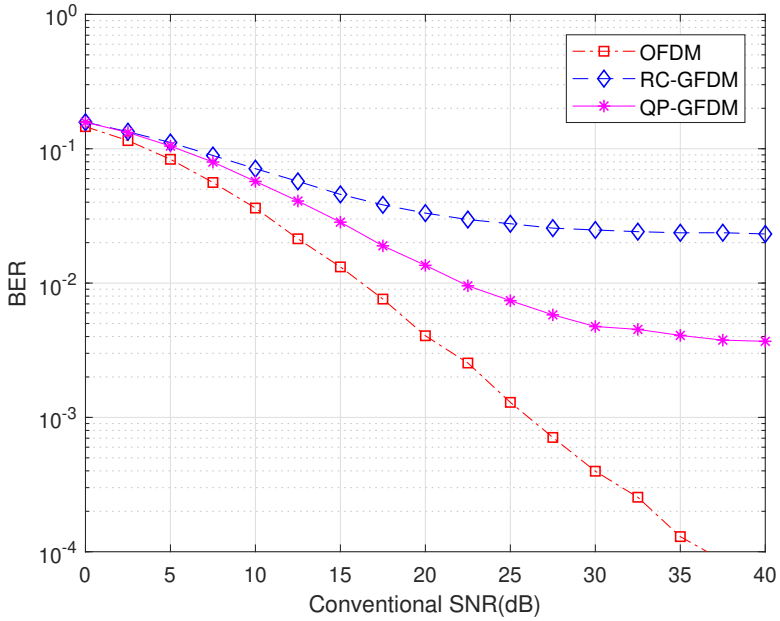

Figure 6.8: BER analysis of GFDM and OFDM signals that are subjected to HPA non-linearity using conventional SNR.

using the effective SNR with Class-A and Class-B amplifiers, shown in Fig. 6.9 and Fig. 6.10, respectively. Both analysis show that the BER is increased as compared with using conventional SNR, with systems using Class-A amplifiers having poorer performance.

6.3.4 Spectral Efficiency

The spectral efficiency analysis of the OFDM, RC-GFDM, and QP-GFDM for Class-A and Class-B HPA are analysed using AMI in (6.18), as shown in Fig. 6.11 and Fig. 6.12, respectively. To achieve AMI = 3 bits/sample for Class-A amplifiers, the OFDM system requires the lowest SNR_{eff} value of about 20 dB, followed by QP-GFDM and RC-GFDM at about 23 dB and 27 dB, respectively. As for systems using Class-B amplifiers, the OFDM system can achieve AMI = 3 bits/sample at SNR_{eff} = 13 dB, QP-GFDM at 17 dB, and RC-GFDM at 20 dB. This follows from the BER analysed previously, where a worse BER will have a lower spectral efficiency. It can also be seen from both Fig. 6.11 and Fig. 6.12

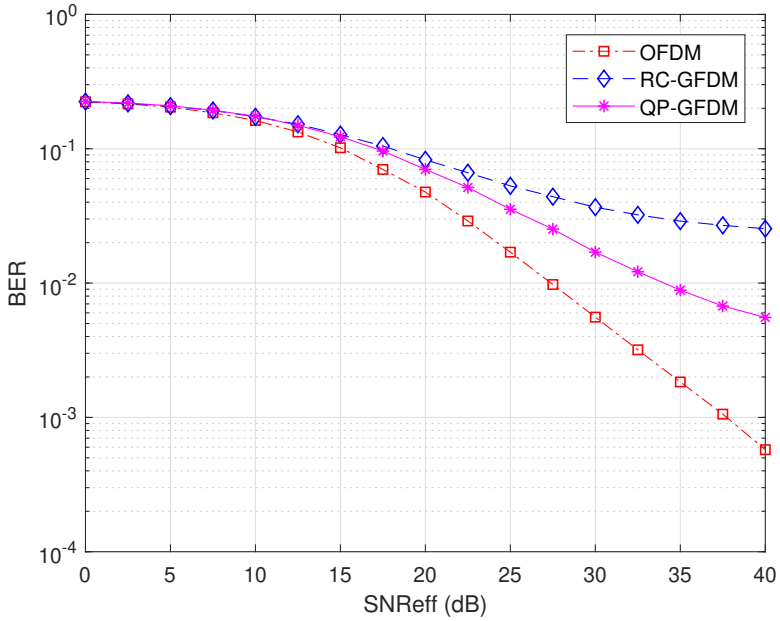

Figure 6.9: BER of GFDM systems with Class-A HPA using the effective SNR measure.

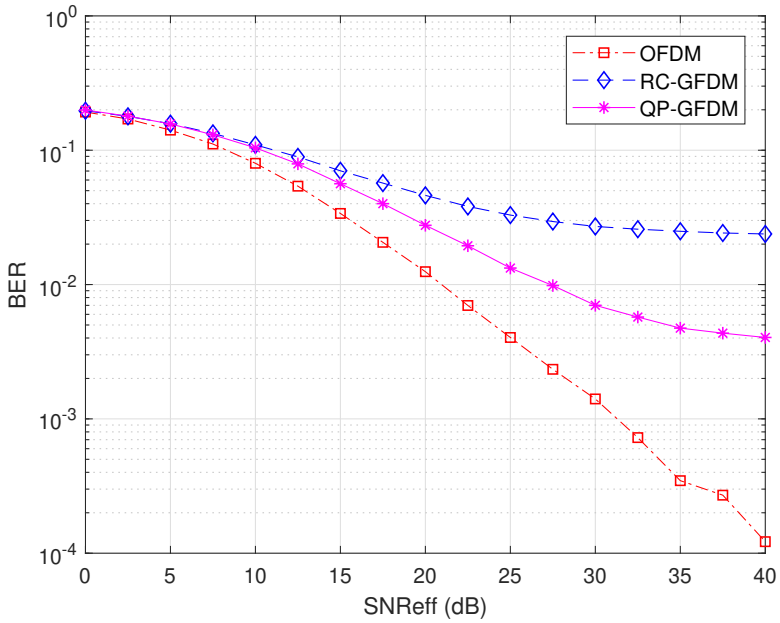

Figure 6.10: BER of GFDM systems using Class-B HPA using the effective SNR measure.

that the AMI obtained from QP-GFDM reaches 3.7 bits/sample, which is close to the OFDM system with AMI of 4 bits/sample.

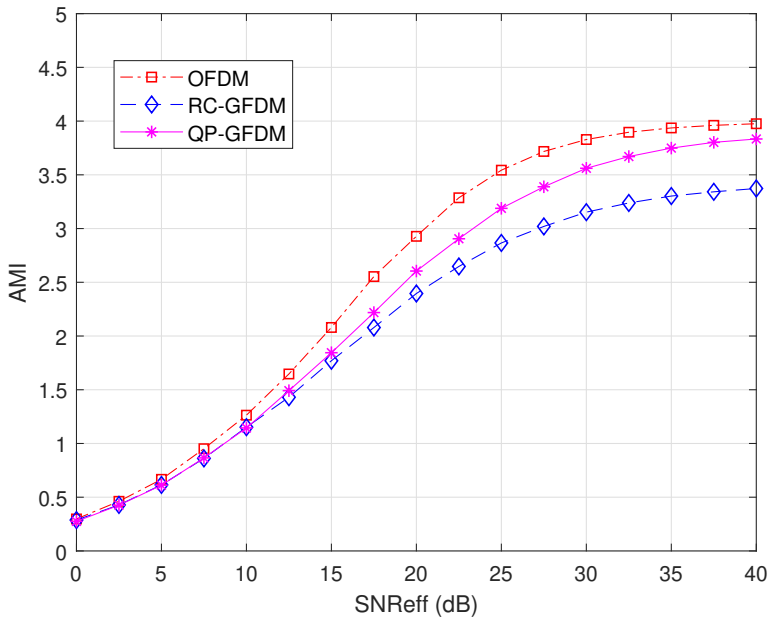

Figure 6.11: AMI of the GFDM systems with Class-A HPA.

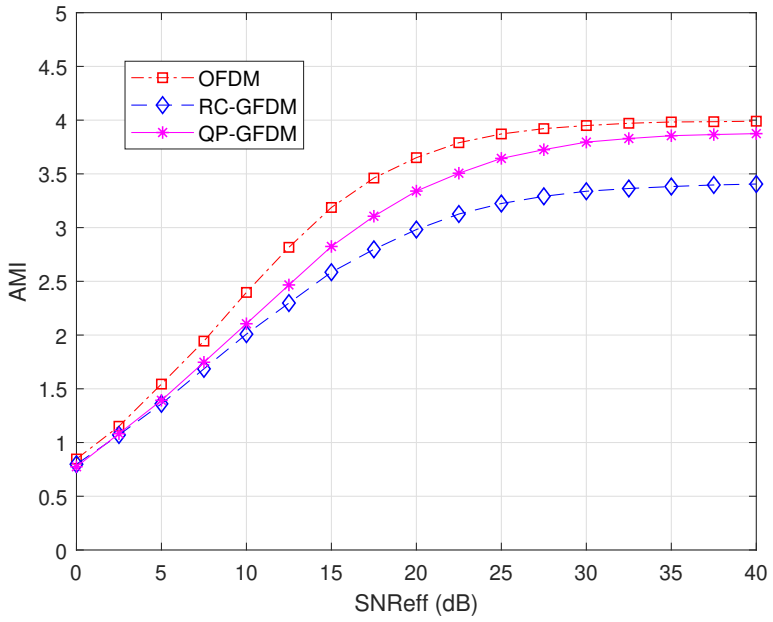

Figure 6.12: AMI of the GFDM systems with Class-B HPA.

6.3.5 Energy Efficiency

The implementation of pulse shape filtering in GFDM requires additional processing at both the transmitter and receiver, which will increase the power consumption. The power consumption is measured using data from a fixed-point DSP as described in [44]. The energy consumption of the DSP per cycle is $415.8\frac{\text{pWsec}}{\text{cycle}}$, where a complex multiplication requires 3 cycles. The energy consumption per GFDM symbol can then be written as

$$\begin{aligned}\mathcal{P}_c &= 415.8\frac{\text{pWsec}}{\text{cycle}}[3(C_{GFDM})]\text{cycle} \\ &= 1.2474[C_{GFDM}]\mu\text{J}.\end{aligned} \tag{6.20}$$

The complexity of the GFDM system C_{GFDM} only considers the FFT operations and the filter multiplication, where other operations are assumed to be omitted as they can be realized by means of register manipulation. The complexity at the transmitter, $C_{GFDM,Tx}$, and receiver, $C_{GFDM,Rx}$, can be calculated, respectively, using [87], [88]

$$C_{GFDM,Tx} = KM\log_2 M + KVM + N\log_2 N, \tag{6.21}$$

and

$$C_{GFDM,Rx} = N\log_2 N + KVM + KM\log_2 M, \tag{6.22}$$

where N is the total number of data symbols, K is the number of subcarriers, M is the number of subsymbols, and V is the upsampling factor of the filter. As illustrated in Fig. 6.13 and Fig. 6.14, QP-GFDM has a higher energy efficiency than RC-GFDM by about 7 bits/J for one GFDM sample in both cases with Class-A and Class-B amplifiers.

The performance of the QP-GFDM system compared to the one of RC-GFDM

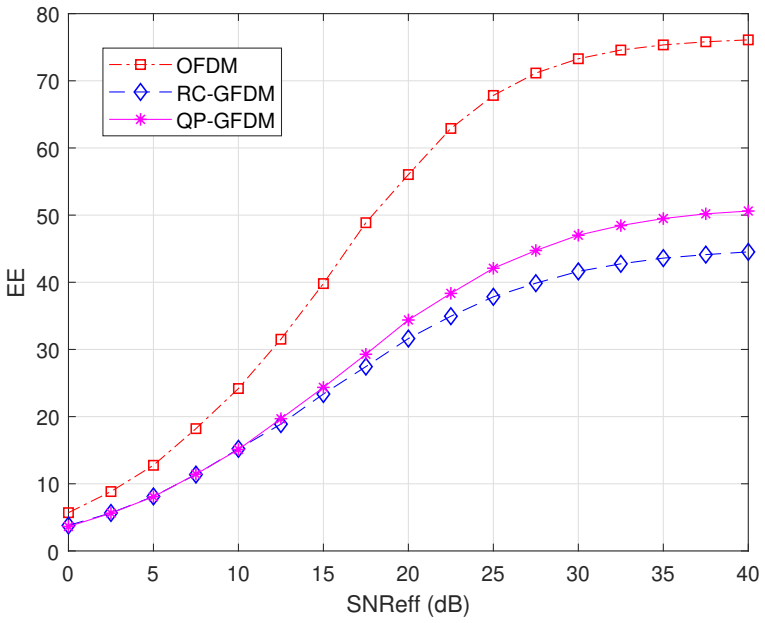

Figure 6.13: Energy Efficiency of RC-GFDM and QP-GFDM with Class-A HPA.

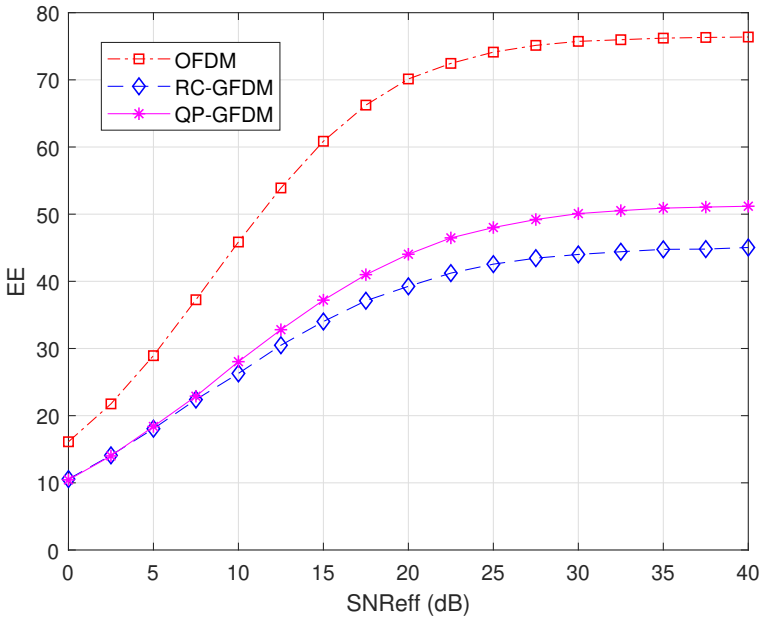

Figure 6.14: Energy Efficiency of RC-GFDM and QP-GFDM with Class-B HPA.

and OFDM is summarized in Fig. 6.15. The HPA non-linearity will introduce spectral regrowth, but the PSD of the GFDM signal shows that the OOB radiation of the distorted GFDM signal is still within acceptable levels, with QP-GFDM having an OOB radiation of about 1 dB lower than RC-GFDM. The OFDM system has a significantly better energy efficiency as compared to QP-GFDM and RC-GFDM, but it has a higher OOB radiation which may interfere with neighbouring channels. In summary, the GFDM system has a much lower OOB radiation than the OFDM system, which is desirable in wireless communication systems. The designed pulse shaping filter in GFDM, QP-GFDM, is superior to the ideal RC filter in GFDM, RC-GFDM, in all performance metrics analysed.

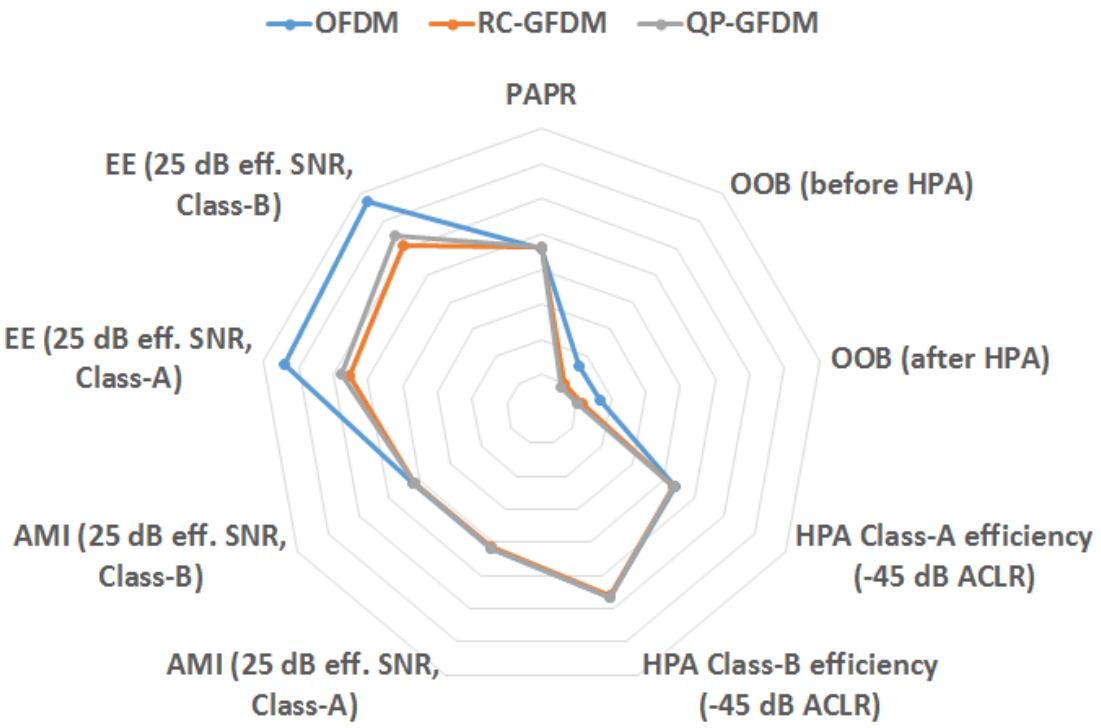

Figure 6.15: Performance comparison of QP-GFDM, RC-GFDM, and OFDM.

6.4 Concluding Remarks

In this chapter, a pulse shaping filter design using a computationally efficient optimisation approach has been presented. The performance of the designed pulse shaping filter in a GFDM system has been analysed by considering the effects of HPA non-linearity.

Numerical simulations have shown that the designed pulse shaping filter has a frequency response that is a close approximate of the ideal RC filter. The analysis on the OOB radiation has shown that the GFDM system using the designed pulse shaping filter, QP-GFDM, has an OOB radiation that is about 3 dB lower than the GFDM system with RC filter, RC-GFDM, and more than 10 dB lower than the conventional OFDM system. The CCDF analysis for PAPR shows that QP-GFDM has a PAPR between OFDM and RC-GFDM, with QP-GFDM having a PAPR of about 0.3 dB lower than RC-GFDM. By varying the IBO, a trade-off between achieving low OOB radiation and high HPA efficiency has been illustrated. Due to scarcity of spectrum resources, a low OOB radiation is preferred. Following 5G-NR specifications, the ACLR limit has been set at -45 dB and the IBO for each system that satisfies the limit has been obtained.

At ACLR $= -45$ dB, it has been shown that QP-GFDM has a better HPA efficiency with both Class-A and Class-B amplifiers, when compared with RC-GFDM. Although the HPA non-linearity will introduce spectral regrowth, the PSD of the GFDM signal shows that the OOB radiation of the distorted GFDM signal is still within acceptable levels, with QP-GFDM having an OOB radiation of about 1 dB lower than RC-GFDM. At the receiver, QP-GFDM is able to achieve a much lower BER, but is worse than OFDM due to ISI from pulse shaping. QP-GFDM has an AMI of around 0.5 bits/sample more than RC-GFDM in both Class-A and Class-B amplifiers, while also having an energy efficiency performance about 7 bits/J per sample greater than RC-GFDM at an effective SNR of 40 dB.

Chapter 7

Conclusions and Future Works

7.1 Conclusions

One of the major issues in multicarrier systems is the high PAPR of the transmitted signal. The pulse shaping technique is effective in reducing the PAPR of the multicarrier transmitted signal. Using ideal filters are well-known. However, ideal filters are non-causal and cannot be implemented practically without truncation and shifting process. This thesis has proposed to design the pulse shaping filters for multicarrier systems using computationally efficient optimisation method.

In Chapter 3, the performance of designing pulse shaping filters for MU-OFDM system is analysed. MU-OFDM systems increase the number of users utilizing the OFDM system at a given time. To apply pulse shaping into MU-OFDM systems, each pulse shape must differ from each other in order for the receiver to be able to detect the intended user data. A set of pulse shaping filter has been designed using min-max optimisation. The designed filter set has shown to be able to reduce the PAPR of the MU-OFDM transmitted signal by about 1.5 dB and has a lower BER when compared to an MU-OFDM system without pulse shaping. The designed set of pulse shaping filters is also implemented in MU-MIMO-OFDM systems, where the PAPR of the MU-MIMO-OFDM transmitted

signal is reduced by about 1.4 dB and also has a lower BER.

In Chapter 4, the research focuses on the GFDM system. The GFDM system was proposed as a promising waveform for implementation in 5G. The main advantage of the GFDM system is the flexibility of the system in accommodating different types of traffic, including burst-type transmissions. Pulse shaping is an integral part of the GFDM system, as a proper selection of prototype filter is capable of reducing the PAPR and OOB as compared with conventional OFDM systems. The quadratic programming filter design technique has been used to design a causal pulse shaping filter for implementation in GFDM systems as the prototype filter. Simulation results indicate that the designed causal pulse shaping filters are able to reduce the PAPR of the GFDM signal by about 0.3 dB as compared with using RC as the prototype filter. The OOB radiation is also reduced to -82.95 dB when using the designed filter, about 25 dB lower than the GFDM system with the RC filter.

In Chapter 5, the BER performance of the GFDM system is analysed. As the GFDM system suffers from self interference from non orthogonality of pulse shaping, the BER is severely degraded as compared with a conventional OFDM system. The designed filter has a better BER than the ideal filter when analysed over the AWGN channel and HIPERLAN/2 channel. To mitigate the self interference, an iterative interference cancellation algorithm is implemented. By using the interference cancellation algorithm, the SNR required for the GFDM system with designed filter is improved to 25 dB at a BER of 10^{-3}.

In Chapter 6, the holistic approach investigation is conducted on the GFDM system when the HPA is applied. In a practical system, the transmit signal will pass through a HPA before transmitted over the wireless channel. Nonlinear characteristics of the HPA will affect the performance characteristics of the communication system. Following 5G-NR specifications, an optimal IBO is obtained by limiting the ACLR at -45 dB. Numerical results show that the GFDM system with the designed filter has a better energy efficiency of about 7 bits/J per sample

better than the one with RC filter.

7.2 Future Research

In 5G-NR, the DFT-s-OFDM and CP-OFDM have been identified as the modulation technique for the uplink and downlink, respectively. The current pulse shaping filter design approaches can be used to design filters that improve the DFT-s-OFDM and CP-OFDM systems.

The OFDM system exhibits certain intrinsic drawbacks and may not be suitable for certain 5G use cases. The GFDM system is one of the potential candidates for future wireless communication systems. To justify the implementation of the GFDM system in replacing OFDM for 5G and beyond, it is essential to further improve the GFDM system.

The filter design problem can be formulated to minimize the PAPR, which is related to various HPA performance metrics. A theoretical derivation of the PAPR of the GFDM signal is also essential in understanding how the PAPR can be minimized. Additionally, it is also worth to further investigate the spectral efficiency and energy efficiency of GFDM systems by considering the efficient usage of CP as well as implementation of lower complexity GFDM transceivers.

The implementation of pulse shape filtering results in nonorthogonality, which induces self interference. The existing interference cancellation algorithm is not able to mitigate the self interference for different types of filters. Therefore, a more general interference cancellation algorithm that minimises the self interference due to filtering in GFDM can be designed.

References

[1] Cisco, "Cisco annual internet report (2018-2023)," February 2020. [Online]. Available: https://www.cisco.com/c/en/us/solutions/collateral/executive-perspectives/annual-internet-report/white-paper-c11-741490.html

[2] N. Saxena, A. Roy, B. J. R. Sahu, and H. Kim, "Efficient IoT gateway over 5G wireless: A new design with prototype and implementation results," *IEEE Commun. Mag.*, vol. 55, no. 2, pp. 97–105, February 2017.

[3] Y. Zhang, R. Yu, M. Nekovee, Y. Liu, S. Xie, and S. Gjessing, "Cognitive machine-to-machine communications: visions and potentials for the smart grid," *IEEE Network*, vol. 26, no. 3, pp. 6–13, May 2012.

[4] E. Dahlman, G. Mildh, S. Parkvall, J. Peisa, J. Sachs, Y. Selén, and J. Sköld, "5G wireless access: requirements and realization," *IEEE Commun. Mag.*, vol. 52, no. 12, pp. 42–47, December 2014.

[5] A. Osseiran, F. Boccardi, V. Braun, K. Kusume, P. Marsch, M. Maternia, O. Queseth, M. Schellmann, H. Schotten, H. Taoka, H. Tullberg, M. A. Uusitalo, B. Timus, and M. Fallgren, "Scenarios for 5G mobile and wireless communications: the vision of the METIS project," *IEEE Commun. Mag.*, vol. 52, no. 5, pp. 26–35, May 2014.

[6] D. Raychaudhuri and N. B. Mandayam, "Frontiers of wireless and mobile communications," *Proc. IEEE*, vol. 100, no. 4, pp. 824–840, April 2012.

[7] F. Boccardi, R. W. Heath, A. Lozano, T. L. Marzetta, and P. Popovski, "Five disruptive technology directions for 5G," *IEEE Commun. Mag.*, vol. 52, no. 2, pp. 74–80, February 2014.

[8] P. Demestichas, A. Georgakopoulos, D. Karvounas, K. Tsagkaris, V. Stavroulaki, J. Lu, C. Xiong, and J. Yao, "5G on the horizon: Key challenges for the radio-access network," *IEEE Veh. Technol. Mag.*, vol. 8, no. 3, pp. 47–53, Sep. 2013.

[9] G. Wunder, P. Jung, M. Kasparick, T. Wild, F. Schaich, Y. Chen, S. T. Brink, I. Gaspar, N. Michailow, A. Festag, L. Mendes, N. Cassiau, D. Ktenas, M. Dryjanski, S. Pietrzyk, B. Eged, P. Vago, and F. Wiedmann, "5GNOW: non-orthogonal, asynchronous waveforms for future mobile applications," *IEEE Commun. Mag.*, vol. 52, no. 2, pp. 97–105, Feb 2014.

[10] J. G. Andrews, S. Buzzi, W. Choi, S. V. Hanly, A. Lozano, A. C. K. Soong, and J. C. Zhang, "What will 5G be?" *IEEE J. Sel. Areas Commun.*, vol. 32, no. 6, pp. 1065–1082, June 2014.

[11] P. Guan, D. Wu, T. Tian, J. Zhou, X. Zhang, L. Gu, A. Benjebbour, M. Iwabuchi, and Y. Kishiyama, "5G field trials: OFDM-based waveforms and mixed numerologies," *IEEE J. Sel. Areas Commun.*, vol. 35, no. 6, pp. 1234–1243, June 2017.

[12] C. Wang, F. Haider, X. Gao, X. You, Y. Yang, D. Yuan, H. M. Aggoune, H. Haas, S. Fletcher, and E. Hepsaydir, "Cellular architecture and key technologies for 5G wireless communication networks," *IEEE Commun. Mag.*, vol. 52, no. 2, pp. 122–130, February 2014.

[13] E. Dahlman, S. Parkvall, J. Skold, and P. Beming, *3G Evolution: HSPA and LTE for Mobile Broadband*, ser. 3G Evolution. Elsevier Science, 2010.

[14] N. Islam and R. Want, "Smartphones: Past, present, and future," *IEEE Pervas. Comput.*, vol. 13, no. 4, pp. 89–92, Oct 2014.

[15] R. Caldwell and A. Anpalagan, "Meeting mobile's demands with multicarrier systems," *IEEE Potentials*, vol. 24, no. 5, pp. 27–31, Dec 2005.

[16] Ericsson, "Ericsson mobility report," November 2019.

[17] F. Ghavimi and H. Chen, "M2M communications in 3GPP LTE/LTE-A networks: Architectures, service requirements, challenges, and applications," *IEEE Commun. Surveys Tut.*, vol. 17, no. 2, pp. 525–549, Q2 2015.

[18] M. Agiwal, A. Roy, and N. Saxena, "Next generation 5G wireless networks: A comprehensive survey," *IEEE Commun. Surveys Tut.*, vol. 18, no. 3, pp. 1617–1655, Q3 2016.

[19] Q. Wu, G. Y. Li, W. Chen, D. W. K. Ng, and R. Schober, "An overview of sustainable green 5G networks," *IEEE Wireless Commun.*, vol. 24, no. 4, pp. 72–80, Aug 2017.

[20] P. Banelli, S. Buzzi, G. Colavolpe, A. Modenini, F. Rusek, and A. Ugolini, "Modulation formats and waveforms for 5G networks: Who will be the heir of OFDM?: An overview of alternative modulation schemes for improved spectral efficiency," *IEEE Signal Process. Mag.*, vol. 31, no. 6, pp. 80–93, Nov 2014.

[21] Zhendao Wang and G. B. Giannakis, "Wireless multicarrier communications," *IEEE Signal Process. Mag.*, vol. 17, no. 3, pp. 29–48, 2000.

[22] J. A. C. Bingham, "Multicarrier modulation for data transmission: an idea whose time has come," *IEEE Commun. Mag.*, vol. 28, no. 5, pp. 5–14, May 1990.

[23] H. Lin, "Flexible configured OFDM for 5G air interface," *IEEE Access*, vol. 3, pp. 1861–1870, 2015.

[24] B. Muquet, Zhengdao Wang, G. B. Giannakis, M. de Courville, and P. Duhamel, "Cyclic prefixing or zero padding for wireless multicarrier

transmissions?" *IEEE Trans. Commun*, vol. 50, no. 12, pp. 2136–2148, Dec 2002.

[25] J. Abdoli, M. Jia, and J. Ma, "Filtered OFDM: A new waveform for future wireless systems," in *2015 IEEE 16th International Workshop on Signal Processing Advances in Wireless Communications (SPAWC)*, June 2015, pp. 66–70.

[26] S. Venkatesan and R. A. Valenzuela, "OFDM for 5G: Cyclic prefix versus zero postfix, and filtering versus windowing," in *2016 IEEE International Conference on Communications (ICC)*, May 2016, pp. 1–5.

[27] B. Farhang-Boroujeny, "OFDM versus filter bank multicarrier," *IEEE Signal Process. Mag.*, vol. 28, no. 3, pp. 92–112, May 2011.

[28] V. Vakilian, T. Wild, F. Schaich, S. ten Brink, and J. F. Frigon, "Universal-filtered multi-carrier technique for wireless systems beyond LTE," in *2013 IEEE Globecom Workshops (GC Wkshps)*, Dec 2013, pp. 223–228.

[29] G. Fettweis, M. Krondorf, and S. Bittner, "GFDM -generalized frequency division multiplexing," in *VTC Spring 2009 - IEEE 69th Veh. Technol. Conf.*, April 2009, pp. 1–4.

[30] S. Weinstein and P. Ebert, "Data transmission by frequency-division multiplexing using the discrete fourier transform," *IEEE Trans. Commun.*, vol. 19, no. 5, pp. 628–634, October 1971.

[31] S. H. Han and J. H. Lee, "An overview of peak-to-average power ratio reduction techniques for multicarrier transmission," *IEEE Wireless Commun.*, vol. 12, no. 2, pp. 56–65, April 2005.

[32] A. Ghosh, D. R. Wolter, J. G. Andrews, and R. Chen, "Broadband wireless access with WiMax/802.16: current performance benchmarks and future potential," *IEEE Commun. Mag.*, vol. 43, no. 2, pp. 129–136, Feb 2005.

[33] C. Eklund, R. B. Marks, K. L. Stanwood, and S. Wang, "IEEE standard 802.16: a technical overview of the wirelessman/sup tm/ air interface for broadband wireless access," *IEEE Commun. Mag.*, vol. 40, no. 6, pp. 98–107, June 2002.

[34] R. V. Nee, "OFDM physical layer specification for the 5 GHz band," *IEEE P802.11-98/12*, January 1998.

[35] "Requirements for further advancements for evolved universal terrestrial radio access (EUTRA)," *3GPP TR 36.913 V8.0.1*, Mar 2009.

[36] M. Simsek, A. Aijaz, M. Dohler, J. Sachs, and G. Fettweis, "5G-enabled tactile internet," *IEEE J. Sel. Areas Commun.*, vol. 34, no. 3, pp. 460–473, March 2016.

[37] NGMN Alliance, "NGMN 5G white paper," February 2015.

[38] B. Farhang-Boroujeny and H. Moradi, "OFDM inspired waveforms for 5G," *IEEE Communications Surveys Tutorials*, vol. 18, no. 4, pp. 2474–2492, Q4 2016.

[39] P. H. Moose, "A technique for orthogonal frequency division multiplexing frequency offset correction," *IEEE Trans. Commun*, vol. 42, no. 10, pp. 2908–2914, Oct 1994.

[40] B. Yang, K. B. Letaief, R. S. Cheng, and Z. Cao, "Timing recovery for OFDM transmission," *IEEE J. Sel. Areas Commun.*, vol. 18, no. 11, pp. 2278–2291, Nov 2000.

[41] T. M. Schmidl and D. C. Cox, "Robust frequency and timing synchronization for OFDM," *IEEE Trans. Commun.*, vol. 45, no. 12, pp. 1613–1621, Dec 1997.

[42] J. J. van de Beek, M. Sandell, and P. O. Borjesson, "ML estimation of time and frequency offset in OFDM systems," *IEEE Trans. Signal Process.*, vol. 45, no. 7, pp. 1800–1805, July 1997.

[43] H. Ochiai, "An analysis of band-limited communication systems from amplifier efficiency and distortion perspective," *IEEE Trans. Commun.*, vol. 61, no. 4, pp. 1460–1472, April 2013.

[44] R. J. Baxley and G. T. Zhou, "Power savings analysis of peak-to-average power ratio in OFDM," *IEEE Trans. Consum. Electron.*, vol. 50, no. 3, pp. 792–798, Aug 2004.

[45] T. Jiang and Y. Wu, "An overview: Peak-to-average power ratio reduction techniques for OFDM signals," *IEEE Trans. Broadcast.*, vol. 54, no. 2, pp. 257–268, June 2008.

[46] Y. Rahmatallah and S. Mohan, "Peak-to-average power ratio reduction in OFDM systems: A survey and taxonomy," *IEEE Commun. Surveys Tuts.*, vol. 15, no. 4, pp. 1567–1592, April 2013.

[47] G. Wunder, R. F. H. Fischer, H. Boche, S. Litsyn, and J. No, "The PAPR problem in OFDM transmission: New directions for a long-lasting problem," *IEEE Signal Process. Mag.*, vol. 30, no. 6, pp. 130–144, Nov 2013.

[48] F. H. Juwono and D. Gunawan, "PAPR reduction using Huffman coding combined with clipping and filtering for OFDM transmitter," in *2009 Innovative Technologies in Intelligent Systems and Industrial Applications*, July 2009, pp. 344–347.

[49] X. Li and L. Cimini, "Effects of clipping and filtering on the performance of OFDM," *Commun. Lett., IEEE*, vol. 2, no. 5, pp. 131–133, May 1998.

[50] R. Dinis and A. Gusmao, "On the performance evaluation of OFDM transmission using clipping techniques," in *Gateway to 21st Century Commu-*

nications Village. VTC 1999-Fall. IEEE VTS 50th Veh. Technol. Conf., vol. 5, Sept 1999, pp. 2923–2928 vol.5.

[51] H.-G. Ryu, B.-I. Jin, and I.-B. Kim, "PAPR reduction using soft clipping and ACI rejection in OFDM system," *IEEE Trans. Consum. Electron.*, vol. 48, no. 1, pp. 17–22, Feb 2002.

[52] J. Armstrong, "Peak-to-average power reduction for OFDM by repeated clipping and frequency domain filtering," *Electron. Lett.*, vol. 38, no. 5, pp. 246–247, Feb 2002.

[53] H. Ochiai and H. Imai, "Performance analysis of deliberately clipped OFDM signals," *IEEE Trans. Commun.*, vol. 50, no. 1, pp. 89–101, Jan 2002.

[54] R. Bauml, R. Fischer, and J. Huber, "Reducing the peak-to-average power ratio of multicarrier modulation by selected mapping," *Electron. Lett.*, vol. 32, no. 22, pp. 2056–2057, Oct 1996.

[55] L. Yang, K. K. Soo, Y. M. Siu, and S. Q. Li, "A low complexity selected mapping scheme by use of time domain sequence superposition technique for PAPR reduction in OFDM system," *IEEE Trans. Broadcast.*, vol. 54, no. 4, pp. 821–824, Dec 2008.

[56] T. Jiang, W. Xiang, P. C. Richardson, J. Guo, and G. Zhu, "PAPR reduction of OFDM signals using partial transmit sequences with low computational complexity," *IEEE Trans. Broadcast.*, vol. 53, no. 3, pp. 719–724, Sep. 2007.

[57] Seung Hee Han and Jae Hong Lee, "PAPR reduction of OFDM signals using a reduced complexity PTS technique," *IEEE Signal Process. Lett.*, vol. 11, no. 11, pp. 887–890, Nov 2004.

[58] S. Slimane, "Peak-to-average power ratio reduction of OFDM signals using broadband pulse shaping," in *Veh. Technol. Conf., 2002. VTC 2002-Fall. 2002 IEEE 56th*, vol. 2, 2002, pp. 889–893 vol.2.

[59] S. Slimane, "Peak-to-average power ratio reduction of OFDM signals using pulse shaping," in *Global Telecommunications Conference, 2000. GLOBECOM '00. IEEE*, vol. 3, 2000, pp. 1412–1416 vol.3.

[60] R. Reine and Z. Zang, "Analysis and comparison of a set of ISI free waveforms for PAPR reduction in OFDM systems," in *TENCON 2011 - 2011 IEEE Region 10 Conference*, Nov 2011, pp. 246–250.

[61] N. Michailow and G. Fettweis, "Low peak-to-average power ratio for next generation cellular systems with generalized frequency division multiplexing," in *2013 Int. Symp. Intell. Signal Process. and Commun. Syst.*, Nov 2013, pp. 651–655.

[62] L. Sendrei and S. Marchevský, "On the performance of GFDM systems undergoing nonlinear amplification," *Acta Electrotechnica et Informatica*, vol. 15, no. 1, pp. 9–14, 2015.

[63] S. Slimane, "Reducing the peak-to-average power ratio of OFDM signals through precoding," *IEEE Trans. Veh. Technol.*, vol. 56, no. 2, pp. 686–695, March 2007.

[64] M.-J. Hao and C.-H. Lai, "Pulse shaping based PAPR reduction for OFDM signals with minimum error probability," in *Intelligent Signal Processing and Communications Systems, 2008. ISPACS 2008. International Symposium on*, Feb 2009, pp. 1–4.

[65] T. Sultana and S. Shawkat, "Employment of pulse shaping techniques for efficient PAPR reduction in OFDM system," in *Computer and Information Technology (ICCIT), 2014 17th International Conference on*, Dec 2014, pp. 482–487.

[66] R. Reine and Z. Zang, "A quadratic programming approach in pulse shaping filter design to reducing PAPR in OFDM systems," in *2013 19th Asia-Pacific Conf. Commun. (APCC)*, Aug 2013, pp. 572–576.

[67] M. S. John Proakis, *Digital Communications, 5th Edition*, 5th ed. McGraw-Hill Science Engineering Math, 2007.

[68] C. Tellambura, "Computation of the continuous-time PAR of an OFDM signal with BPSK subcarriers," *IEEE Commun. Lett.*, vol. 5, no. 5, pp. 185–187, May 2001.

[69] Y. S. Cho, J. Kim, W. Y. Yang, and C. G. Kang, *MIMO-OFDM Wireless Communications with MATLAB*, 1st ed. Wiley, 2010.

[70] S. Daumont, B. Rihawi, and Y. Lout, "Root-raised cosine filter influences on PAPR distribution of single carrier signals," in *3rd Int. Symp. on Commun., Contr. Signal Process. (ISCCSP) 2008.*, March 2008, pp. 841–845.

[71] P. Tan and N. Beaulieu, "Reduced ICI in OFDM systems using the "better than" raised-cosine pulse," *IEEE Commun. Lett.*, vol. 8, no. 3, pp. 135–137, March 2004.

[72] X.-G. Xia, "A family of pulse-shaping filters with ISI-free matched and unmatched filter properties," *IEEE Trans. Commun.*, vol. 45, no. 10, pp. 1157–1158, Oct 1997.

[73] A. Assalini and A. M. Tonello, "Improved nyquist pulses," *IEEE Commun. Lett.*, vol. 8, no. 2, pp. 87–89, Feb 2004.

[74] N. Michailow, M. Matthé, I. S. Gaspar, A. N. Caldevilla, L. L. Mendes, A. Festag, and G. Fettweis, "Generalized frequency division multiplexing for 5th generation cellular networks," *IEEE Trans. Commun.*, vol. 62, no. 9, pp. 3045–3061, Sept 2014.

[75] K. Liu, W. Deng, and Y. Liu, "Theoretical analysis of the peak-to-average power ratio and optimal pulse shaping filter design for GFDM systems," *IEEE Trans. on Signal Process.*, vol. 67, no. 13, pp. 3455–3470, July 2019.

[76] M. Ben Mabrouk, M. Chafii, Y. Louët, and F. Bader, "Low-PAPR condition for 5G-candidate waveforms," in *2017 XXXIInd General Assembly and Scientific Symposium of the International Union of Radio Science (URSI GASS)*, 2017, pp. 1–4.

[77] R. Reine and Z. Zang, "Semi-infinite quadratic programming approach to design FIR filter for PAPR reduction in OFDM system," in *2014 IEEE Workshop on Statistical Signal Processing (SSP)*, June 2014, pp. 408–411.

[78] Z. Zang and S. Nordholm, "Orthogonal digital waveform set for multi-dimensional signaling and multiuser communications with matched filter receivers," in *Communications, 2004 and the 5th International Symposium on Multi-Dimensional Mobile Communications Proceedings. The 2004 Joint Conference of the 10th Asia-Pacific Conference on*, vol. 2, Aug 2004, pp. 883–887 vol.2.

[79] J. Adeane, Z. Zang, and S. Nordholm, "Design of digital waveform set for multiuser CDMA communications with matched filter receivers," in *Information, Communications and Signal Processing, 2003 and Fourth Pacific Rim Conference on Multimedia. Proceedings of the 2003 Joint Conference of the Fourth International Conference on*, vol. 2, Dec 2003, pp. 844–848 vol.2.

[80] Z. Zang and S. Nordholm, "Design of ODMA digital waveforms using non-convex optimization methods," *Annals of Operations Research*, vol. 133, no. 1, pp. 319–330, 2005.

[81] J. Medbo, H. Andersson, P. Schramm, H. Asplund, and J.E.Berg, "Channel models for HIPERLAN/2 in different indoor scenarios," *ETSI BRAN 3ERI085B*, March 1998.

[82] S. Kaiser, "On the performance of different detection techniques for OFDM-CDMA in fading channels," in *Global Telecommunications Conference, 1995. GLOBECOM '95., IEEE*, vol. 3, Nov 1995, pp. 2059–2063 vol.3.

[83] G. L. Stuber, J. R. Barry, S. W. McLaughlin, Ye Li, M. A. Ingram, and T. G. Pratt, "Broadband MIMO-OFDM wireless communications," *Proceedings of the IEEE*, vol. 92, no. 2, pp. 271–294, 2004.

[84] Y. J. Zhang and K. B. Letaief, "An efficient resource-allocation scheme for spatial multiuser access in MIMO/OFDM systems," *IEEE Trans. Commun.*, vol. 53, no. 1, pp. 107–116, 2005.

[85] T. Jiang, C. Ni, and L. Guan, "A novel phase offset SLM scheme for PAPR reduction in Alamouti MIMO-OFDM systems without side information," *IEEE Signal Process. Lett.*, vol. 20, no. 4, pp. 383–386, April 2013.

[86] Y. Cai, Z. Qin, F. Cui, G. Y. Li, and J. A. McCann, "Modulation and multiple access for 5G networks," *IEEE Commun. Surveys Tuts.*, vol. 20, no. 1, pp. 629–646, Q1 2018.

[87] I. Gaspar, N. Michailow, A. Navarro, E. Ohlmer, S. Krone, and G. Fettweis, "Low complexity GFDM receiver based on sparse frequency domain processing," in *2013 IEEE 77th Veh. Technol. Conf. (VTC-Spring)*, June 2013, pp. 1–6.

[88] N. Michailow, I. Gaspar, S. Krone, M. Lentmaier, and G. Fettweis, "Generalized frequency division multiplexing: Analysis of an alternative multi-carrier technique for next generation cellular systems," in *2012 Int. Symp. Wireless Commun. Syst. (ISWCS)*, Aug 2012, pp. 171–175.

[89] W. A. Hassan, H. Jo, and A. R. Tharek, "The feasibility of coexistence between 5G and existing services in the IMT-2020 candidate bands in Malaysia," *IEEE Access*, vol. 5, pp. 14 867–14 888, 2017.

[90] Y. Medjahdi, S. Traverso, R. Gerzaguet, H. Shaïek, R. Zayani, D. Demmer, R. Zakaria, J. Doré, M. Ben Mabrouk, D. Le Ruyet, Y. Louët, and D. Roviras, "On the road to 5G: Comparative study of physical layer in MTC context," *IEEE Access*, vol. 5, pp. 26 556–26 581, 2017.

[91] T. van Waterschoot, V. Le Nir, J. Duplicy, and M. Moonen, "Analytical expressions for the power spectral density of CP-OFDM and ZP-OFDM signals," *IEEE Signal Process. Lett.*, vol. 17, no. 4, pp. 371–374, April 2010.

[92] M. Matthe, N. Michailow, I. Gaspar, and G. Fettweis, "Influence of pulse shaping on bit error rate performance and out of band radiation of generalized frequency division multiplexing," *2014 IEEE Int. Conf. Commun.*, pp. 43–48, 2014.

[93] C. H. G. Yuen and B. Farhang-Boroujeny, "Analysis of the optimum precoder in SC-FDMA," *IEEE Trans. Wireless Commun.*, vol. 11, no. 11, pp. 4096–4107, November 2012.

[94] E. A. L. John R. Barry and D. G. Messerschmitt, *Digital Communication*, 3rd ed. Springer US, 2004.

[95] R. L. Streit and A. H. Nuttall, "A note on the semi-infinite programming approach to complex approximation," *Mathematics of Comput.*, vol. 40, no. 162, pp. 599–605, 1983.

[96] A. Ortega, L. Fabbri, and V. Tralli, "Performance evaluation of GFDM over nonlinear channel," in *2016 Int. Conf. on Inf. and Commun. Technol. Convergence (ICTC)*, Oct 2016, pp. 12–17.

[97] A. Mohammadian, A. Mohammadi, A. Abdipour, and M. Baghani, "Spectral analysis of GFDM modulated signal under nonlinear behavior of power amplifier," *arXiv e-prints*, Mar 2018.

[98] H. Ochiai, "A novel trellis-shaping design with both peak and average power reduction for OFDM systems," *IEEE Trans. Commun.*, vol. 52, no. 11, pp. 1916–1926, 2004.

[99] J. Joung, C. K. Ho, and S. Sun, "Spectral efficiency and energy efficiency of OFDM systems: Impact of power amplifiers and countermeasures," *IEEE J. Sel. Areas Commun.*, vol. 32, no. 2, pp. 208–220, February 2014.

[100] C. Ning, H. Qian, and Q. Hua, "Power efficiency improvements through peak-to-average power ratio reduction and power amplifier linearization," *EURASIP Journal on Advances in Signal Processing*, vol. 2007, 01 2007.

[101] C. Rapp, "Effects of HPA-nonlinearity on 4-DPSK/OFDM-signal for a digital sound broadcasting system," *Proc. 2nd ECSC*, pp. 179–184, 10 1991.

[102] A. A. M. Saleh, "Frequency-independent and frequency-dependent nonlinear models of TWT amplifiers," *IEEE Trans. Commun.*, vol. 29, no. 11, pp. 1715–1720, November 1981.

[103] A. Ghorbani and M. Sheikhan, "The effect of solid state power amplifiers (SSPAs) nonlinearities on MPSK and M-QAM signal transmission," in *1991 Sixth International Conference on Digital Processing of Signals in Communications*, Sep. 1991, pp. 193–197.

[104] S. Teodoro, A. Silva, R. Dinis, F. M. Barradas, P. M. Cabral, and A. Gameiro, "Theoretical analysis of nonlinear amplification effects in massive MIMO systems," *IEEE Access*, vol. 7, pp. 172 277–172 289, 2019.

[105] J. Joung, C. K. Ho, K. Adachi, and S. Sun, "A survey on power-amplifier-centric techniques for spectrum- and energy-efficient wireless communications," *IEEE Commun. Surveys Tut.*, vol. 17, no. 1, pp. 315–333, Q1 2015.

[106] R. Zayani, H. Shaïek, and D. Roviras, "Efficient precoding for massive MIMO downlink under PA nonlinearities," *IEEE Commun. Lett.*, vol. 23, no. 9, pp. 1611–1615, Sep. 2019.

[107] G. U. Maheswari, A. Govindasamy, and S. J. Thiruvengadam, "Performance analysis of filter bank multicarrier system with non-linear high power amplifiers for 5G wireless networks," *IET Signal Process.*, vol. 11, no. 1, pp. 66–72, 2017.

[108] "Realistic power amplifier model for the new radio evaluation," *document R4-163314, 3GPP TSG-RAN WG4 Meeting 79, Nokia*, May 2016.

[109] M. Honkanen and S.-G. Haggman, "New aspects on nonlinear power amplifier modeling in radio communication system simulations," in *Proceedings of 8th International Symposium on Personal, Indoor and Mobile Radio Communications - PIMRC '97*, vol. 3, Sep. 1997, pp. 844–848 vol.3.

[110] R. Yoshizawa and H. Ochiai, "Energy efficiency improvement of coded OFDM systems based on PAPR reduction," *IEEE Syst. J.*, vol. 11, no. 2, pp. 717–728, June 2017.

[111] A. Cheaito, J.-F. Hérald, M. Crussière, and Y. Louët, "EVM derivation of multicarrier signals to determine the operating point of the power amplifier considering clipping and predistortion," *EURASIP J. Wireless Commun. Netw.*, 2016.

[112] T. J. Rouphael, in *RF and Digital Signal Processing for Software-Defined Radio.* Burlington: Newnes, 2009.

[113] Y. Chen, S. Zhang, S. Xu, and G. Y. Li, "Fundamental trade-offs on green wireless networks," *IEEE Commun. Mag.*, vol. 49, no. 6, pp. 30–37, June 2011.

[114] J. M. Meredith, "NR; base station (BS) radio transmission and reception," *3GPP TS 38.104 V15.2.0*, July 2018.